

AD-A136 844

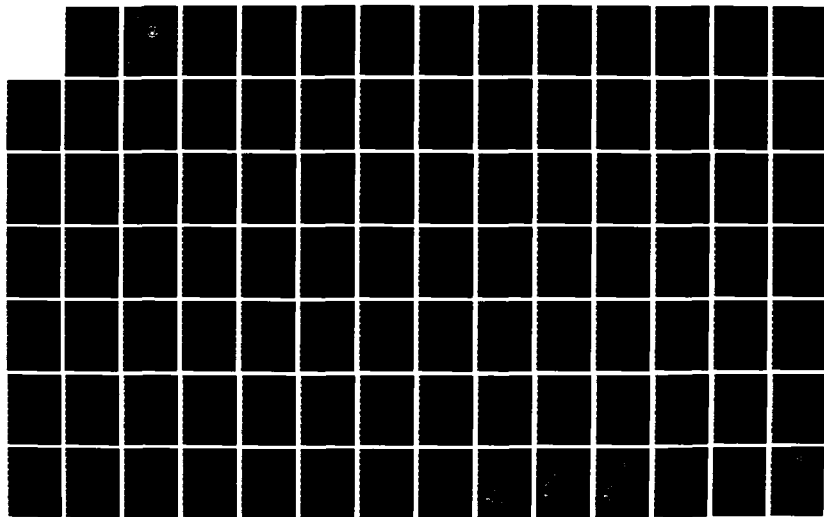
A QUASI-LAGRANGIAN DIAGNOSTICS INVESTIGATION OF RAPID
CYCLOGENESIS IN A POLAR AIR STREAM(U) NAVAL
POSTGRADUATE SCHOOL MONTEREY CA W A COOK SEP 83

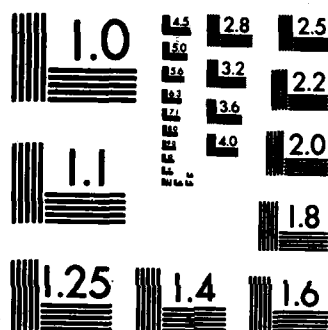
1/2

UNCLASSIFIED

F/G 4/2

NL





MICROCOPY RESOLUTION TEST CHART
NATIONAL BUREAU OF STANDARDS-1963-A

AD A136844

DTIC FILE COPY

NAVAL POSTGRADUATE SCHOOL
Monterey, California



DTIC
ELECTE
JAN 13 1984
S H D

THESIS

A QUASI-LAGRANGIAN DIAGNOSTICS INVESTIGATION
OF
RAPID CYCLOGENESIS IN A POLAR AIR STREAM

by

William A. Cook

September 1983

Thesis Advisor:

C. H. Wash

Approved for public release; distribution unlimited.

04 01 10 000

REPORT DOCUMENTATION PAGE		READ INSTRUCTIONS BEFORE COMPLETING FORM	
1. REPORT NUMBER	2. GOVT ACCESSION NO. AD-A136844	3. RECIPIENT'S CATALOG NUMBER	
4. TITLE (and Subtitle) A Quasi-Lagrangian Diagnostics Investigation of Rapid Cyclogenesis in a Polar Air Stream		5. TYPE OF REPORT & PERIOD COVERED Master's Thesis September 1983	
		6. PERFORMING ORG. REPORT NUMBER	
7. AUTHOR(s) William A. Cook		8. CONTRACT OR GRANT NUMBER(s)	
9. PERFORMING ORGANIZATION NAME AND ADDRESS Naval Postgraduate School Monterey, California 93943		10. PROGRAM ELEMENT, PROJECT, TASK AREA & WORK UNIT NUMBERS	
11. CONTROLLING OFFICE NAME AND ADDRESS Naval Postgraduate School Monterey, California 93943		12. REPORT DATE September 1983	
		13. NUMBER OF PAGES 147	
14. MONITORING AGENCY NAME & ADDRESS (if different from Controlling Office)		15. SECURITY CLASS. (of this report) Unclassified	
		15a. DECLASSIFICATION/DOWNGRADING SCHEDULE	
16. DISTRIBUTION STATEMENT (of this Report) Approved for public release; distribution unlimited		Accession For NTIS GRA&I <input checked="" type="checkbox"/> DTIC TAB <input type="checkbox"/> Unannounced <input type="checkbox"/> Justification	
17. DISTRIBUTION STATEMENT (of the abstract entered in Block 20, if different from Report)		By Distribution/ Availability Codes	
18. SUPPLEMENTARY NOTES		Avail and/or Dist Special A-1	
19. KEY WORDS (Continue on reverse side if necessary and identify by block number) North Atlantic, Quasi-Lagrangian Diagnostics, Mass Budget, Stability Analysis, Vorticity Budget, Explosive Maritime Cyclogenesis, Polar Low			
20. ABSTRACT (Continue on reverse side if necessary and identify by block number) A synoptic investigation employing quasi-Lagrangian diagnostic techniques was conducted for a North Atlantic Ocean polar low undergoing a period of rapid cyclogenesis. The polar low was of relatively small horizontal scale and developed in a region of low static stability and large low-level baroclinity, which is consistent with theoretical studies. Rapid surface pressure falls and vigorous			

circulation increases correlate well with the observed maxima in low-level inward mass transport and upper-level mass outflow, and are temporally coincident with the incursion of the forward divergence quadrant of a jet streak into the budget volume. The most rapid increases of absolute vorticity occurred in the 250 to 300 mb layer, and are related to combined contributions of positive vorticity advection and vertical redistribution processes. The dominant forcing of low-level absolute vorticity increases comes primarily from the divergence source term.

Approved for public release; distribution unlimited

A Quasi-Lagrangian Diagnostics Investigation
Of Rapid Cyclogenesis In A Polar Air Stream

by

William A. Cook
Lieutenant, United States Navy
B.S., Texas A & M University, 1976

Submitted in partial fulfillment of the
requirements for the degree of

MASTER OF SCIENCE IN METEOROLOGY AND OCEANOGRAPHY

from the

NAVAL POSTGRADUATE SCHOOL
September 1983

Author:

William A. Cook

Approved by:

Carl D. Wash THESIS ADVISOR

Russell L. Elsberry SECOND READER

Russell L. Elsberry (Acting)
CHAIRMAN, DEPARTMENT OF METEOROLOGY

AM DURN
DEAN OF SCIENCE AND ENGINEERING

ABSTRACT

A synoptic investigation employing quasi-Lagrangian diagnostic techniques was conducted for a North Atlantic Ocean polar low undergoing a period of rapid cyclogenesis. The polar low was of relatively small horizontal scale and developed in a region of low static stability and large low-level baroclinity, which is consistent with theoretical studies. Rapid surface pressure falls and vigorous circulation increases correlate well with the observed maxima in low-level inward mass transport and upper-level mass outflow, and are temporally coincident with the incursion of the forward divergence quadrant of a jet streak into the budget volume. The most rapid increases of absolute vorticity occurred in the 250 to 300 mb layer, and are related to combined contributions of positive vorticity advection and vertical redistribution processes. The dominant forcing of low-level absolute vorticity increases comes primarily from the divergence source term.

TABLE OF CONTENTS

I.	INTRODUCTION	12
II.	LITERATURE REVIEW	19
III.	DATA BASE	23
IV.	SYNOPTIC DISCUSSION AND NWP PERFORMANCE	27
	A. GENERAL	27
	B. SYNOPTIC DISCUSSION	28
	C. NUMERICAL WEATHER PREDICTION PERFORMANCE	36
V.	QUASI-LAGRANGIAN DIAGNOSTICS	38
VI.	MASS BUDGET AND STABILITY ANALYSES	43
	A. MASS BUDGET	43
	1. Horizontal Mass Transport	43
	2. Vertical Mass Transport	47
	B. STABILITY ANALYSIS	49
	1. Static Stability	50
	2. Potential Temperature	53
	C. SUMMARY	54
VII.	VORTICITY BUDGET ANALYSIS	56
	A. GENERAL	56
	B. TIME TENDENCY	57
	C. LATERAL TRANSPORT	59
	1. Mean Mode and Lateral Divergence	61
	2. Eddy Mode and Lateral Advection	63

D. VERTICAL REDISTRIBUTION	65
E. SOURCES AND SINKS	68
F. RESIDUALS	71
G. SUMMARY	72
VIII. CONCLUSIONS AND RECOMMENDATIONS	74
APPENDIX A. FGGE DATA RELIABILITY	76
APPENDIX B. JET STREAK INTERACTION	80
APPENDIX C. TABLES	83
APPENDIX D. FIGURES	90
LIST OF REFERENCES	142
INITIAL DISTRIBUTION LIST	145

LIST OF TABLES

TABLE I.	Fields Archived in the ECMWF Level III-b Data Set	83
TABLE II.	Previous QLD Studies	84
TABLE III.	Generalized Budget Equation	85
TABLE IV.	Mass Budget Equation	86
TABLE V.	Circulation Budget Equation	87
TABLE VI.	Mean and Eddy Modes	89

LIST OF FIGURES

Figure 1.	FGGE Data Coverage 00 GMT 26 January 1979 . . .	90
Figure 2.	Similar to Figure 1 except for 00 GMT 27 January 1979	91
Figure 3.	Similar to Figure 1 except for 00 GMT 28 January 1979	92
Figure 4.	FGGE Data Management Plan	93
Figure 5.	Storm Track.	94
Figure 6.	Synoptic Situation 12 GMT 26 January 1979 . . .	95
Figure 7.	DMSP IR Imagery 2207 GMT 26 January 1979. . .	96
Figure 8.	FNOC SST Analysis C 12 GMT 26 January 1979.	97
Figure 9.	DMSP IR Imagery 0124 GMT 27 January 1979. . .	98
Figure 10.	Similar to Figure 6 except for 00 GMT 27 January 1979	99
Figure 11.	DMSP IR Imagery 0544 GMT 27 January 1979. . .	100
Figure 12.	DMSP IR Imagery 1043 GMT 27 January 1979. . .	101
Figure 13.	Similar to Figure 6 except for 12 GMT 27 January 1979	102
Figure 14.	DMSP IR Imagery 2006 GMT 27 January 1979. . .	103
Figure 15.	Similar to Figure 6 except for 00 GMT 28 January 1979	104
Figure 16.	DMSP IR Imagery 1025 GMT 28 January 1979. . .	105
Figure 17.	Similar to Figure 6 except for 12 GMT 28 January 1979	106
Figure 18.	Similar to Figure 6 except for 00 GMT 29 January 1979	107
Figure 19.	DMSP IR Imagery 0048 GMT 29 January 1979 . . .	108

Figure 20.	Similar to Figure 6 except for 12 GMT 29 January 1979	109
Figure 21.	FNOC 36-h Model Forecast Comparison. . . .	110
Figure 22.	NMC, FGGE, FNOC Central Pressure Comparison.	111
Figure 23.	Horizontal Mass Flux	112
Figure 24.	Radial Cross-Sections	113
Figure 25.	Radial Cross-Sections	114
Figure 26.	QLD Vertical Velocities (Omegas)	115
Figure 27.	Similar to Figure 26 except for Kinematic Omegas	116
Figure 28.	Similar to Figure 26 except for FGGE Omegas	117
Figure 29.	Static Stability Index.	118
Figure 30.	Area-Averaged Potential Temperatures . . .	119
Figure 31.	Absolute Vorticity Vertical Profiles . . .	120
Figure 32.	Absolute Vorticity Time Sections	121
Figure 33.	Absolute Vorticity Vertical Time Tendency .	122
Figure 34.	Similar to Figure 33 except for Lateral Vorticity Transport	123
Figure 35.	Total, Mean and Eddy Mode Lateral Transports	124
Figure 36.	Similar to Figure 33 except for Mean Mode Transport	125
Figure 37.	Similar to Figure 33 except for Lateral Divergence	126
Figure 38.	Similar to Figure 33 except for Eddy Mode Transport	127

Figure 39.	Similar to Figure 33 except for Lateral Advection	128
Figure 40.	Similar to Figure 33 for Divergence of Vertical Transport	129
Figure 41.	Similar to Figure 33 except for Vertical Divergence	130
Figure 42.	Similar to Figure 33 except for Vertical Advection	131
Figure 43.	Similar to Figure 33 except for Tilting Term	132
Figure 44.	Similar to Figure 33 except for Frictional Dissipation	133
Figure 45.	Similar to Figure 33 except for Residuals .	134
Figure 46.	FGGE 6-h Area-Averaged Potential Temperatures	135
Figure 47.	6-h Static Stability Index	136
Figure 48.	FGGE 6-h Radius 4 Budget Fields	137
Figure 49.	300 mb Isotachs	138
Figure 50.	Similar to Figure 49	139
Figure 51.	Similar to Figure 49	140
Figure 52.	Similar to Figure 49	141

ACKNOWLEDGEMENT

I wish to extend sincere thanks to Mike McDermet and Jim Peak for their gracious assistance in data collection and computational areas. A special thanks goes to Professor R.L. Elsberry for his highly professional and in-depth critical review of this document. Additionally, my sincere appreciation and thanks to my thesis advisor, Professor C.H. Wash. Without his guidance and comprehensive knowledge of analysis techniques employed within this research, this document could not have been completed. Finally, my love and sincere appreciation are extended to my wife, JoAnne, and my children for their strong support and unyielding patience over the last year.

I. INTRODUCTION

The accurate prediction of the development of all severe maritime storms and their subsequent paths is of vital importance to military and civilian sea-going vessels, people living in coastal areas and their associated recreational activities, and to the expanding number of oil rigs situated over continental shelves. The Fastnet Yacht Race (Woodroffe, 1981) is remembered for the unexpected severe weather that caused havoc among the competitors to the south of Ireland. British fine-mesh model forecasts failed to give advance warning of a sudden deepening and the exceptional vigor of a maritime low which produced 15 m seas and gale force winds with gusts up to 34 m/s. Consequently, 24 yachts were missing or abandoned and 15 crew members were lost at sea. In September 1978, the Queen Elizabeth II (James, 1979) encountered unexpectedly heavy southwest seas and swell with winds gusting to 32 m/s, which resulted in structural damage and numerous injuries to passengers and crew. More recently, the oil rig Ranger (Lemoyne, 1982) was sunk due to the destructive weather associated with a maritime cyclone. Early warning is most essential to preclude this loss of life and to minimize damages due to the extreme weather conditions which accompany these powerful cyclones.

Perhaps the most frequently overlooked class of cyclone is the polar low. These primarily maritime systems form poleward of the polar front and generally are not considered to be a severe weather producing system, although appreciable precipitation from convective activity may accompany their passage. Occasionally, these small-scale polar lows undergo rapid intensification and become extremely powerful and dangerous cyclones on a scale comparable to middle latitude maritime cyclones.

The majority of observed cases of explosive cyclogenesis occurring off the east coast of continents at middle latitudes originate as a wave perturbation on a polar front separating polar air from tropical air, as in the classical Norwegian cyclone model. Occasionally, non-frontal cyclones, and specifically the polar low, undergo explosive cyclogenesis in the cold air poleward of the polar front. Based on a study (Sanders and Gyakum, 1980) of 267 explosive deepening cases in the North Pacific and North Atlantic Oceans during the winter months of 1976-1979, less than one percent of the cases occurred at latitudes north of 60°N .

The term "polar" low is widely used in literature to define a small-scale cyclone which forms poleward of the

polar front originating entirely within the polar air mass. However, there appears to be a categorization dilemma concerning the several types of polar lows and the very broad definition of the polar low. For example, all of the following cyclones have been referred to as polar lows:

- Small-scale cyclones poleward of the polar front associated with a comma cloud pattern and a strong positive vorticity maximum in the middle troposphere (Reed, 1979; Mullen, 1979);
- Small-scale cyclones poleward of the polar front not associated with a comma cloud pattern but often connected to spiral cloud patterns (Rasmussen, 1981);
- Small-scale cyclones associated with upper-level short waves commonly formed southeast of Greenland with strong west-northwest winds aloft (Harley, 1960); and
- Initially small-scale cyclones that form on the border of the polar air southeast of Greenland and can explosively deepen, acquiring dimensions comparable to middle latitude extratropical cyclones (Mansfield, 1974).

Some attempts have been made to resolve this categorization dilemma, based upon primary formation mechanisms and geographical considerations. Locatelli *et al.* (1982) suggests that there are two types of polar lows. The first type is mainly baroclinic in nature and possesses frontal characteristics, and the second type develops farther back in the polar air and appears to be more convective than the first type. Similarly, Sardie and Warner (1983) suggest that moist baroclinic processes alone may explain the origin of

North Pacific Ocean polar lows, while moist baroclinicity and CISK are essential in the genesis of North Atlantic Ocean polar lows.

Regardless of whether the nascent low is a middle latitude frontal cyclone or a polar low, explosive cyclogenesis is generally poorly predicted by existing numerical models. Sanders and Gyakum (1980) demonstrate that the National Meteorological Center primitive equation (PE) model predictions of rapidly deepening maritime cyclones typically forecast only one-fourth to one-third of the actual development.

Lack of conclusive evidence and conjecture as to what dominant physical processes are involved in the formation and development of polar lows strongly indicate that further research is necessary before full understanding and accurate prediction eventually can be achieved. Poor data coverage and the small scales over which explosive maritime cyclogenesis occurs have restricted detailed research, and have precluded accurate numerical predictions for many meteorological events over oceanic regions and at high latitudes. Improvements in satellite observations of numerous meteorological variables has moderated this

problem. However, before the potential of this newly acquired data source can be fully realized, a more comprehensive knowledge of the dynamics and thermodynamics involved in explosive cyclogenesis in polar air streams must be obtained.

This study constitutes a portion of a broadly based research effort to better understand and predict rapid maritime cyclogenesis by employing a combined observational and numerical modelling approach. Better understanding of the physical mechanisms and air-sea interactions involved will provide the basis for more credible and accurate numerical modelling schemes for oceanic regions. Specifically, this thesis consists of mass and circulation (absolute vorticity) budgets of a high latitude polar low. The polar low in this study originates as a trough of low pressure extending westward across Iceland on 26 January 1979 and undergoes periods of explosive cyclogenesis as it moves southeasterly toward the United Kingdom during the ensuing 72 h. This system is a prime example of rapid cyclogenesis in a polar air stream. Fortunately, the development occurred during one of the First GARP Global Experiment (FGGE) special observing periods and adequate data are available for research.

Translating storm budget diagnostic procedures (Wash, 1978) will be used in this study for budget analyses. This quasi-Lagrangian diagnostic (QLD) approach focuses expressly on the cyclonic scale to describe quantitatively the features of cyclone development, as well as the processes forcing changes in the cyclonic circulation. These techniques incorporate translational effects as the volume is centered on and moved with the surface pressure minimum of the cyclone. This affords a perspective on the interaction of the cyclone with its environment. Specifically, QLD budgets yield quantitative evaluations of the exchanges of mass, circulation and angular momentum between the budget volume and environment. Sources and sinks, lateral and vertical exchanges of meteorological variables can be calculated and identified with physical and dynamical processes within the volume.

The overall objective of this thesis is to gain insight into the significance and magnitude of several physical processes involved in rapid maritime cyclogenesis in a polar air stream. Specific thesis objectives are:

- Study of the horizontal and vertical mass circulation in relation to the explosive development;
- Investigation of the static stability changes during the development process;

- Study of the development process using vorticity to determine the key terms responsible for the development; and
- Study of the usefulness of the FGGE data for describing this rapidly developing cyclone.

Chapter II will summarize many of the significant research efforts on polar lows. A brief description and analysis of the the FGGE data set utilized as a data base in this study is presented in chapter III. A comprehensive synoptic discussion on the explosively deepening polar low is given in chapter IV. Chapter V provides a general description of the QLD technique and the budget equations utilized. Budget results are contained in Chapter VI and VII, and conclusions and recommendations for further research are in Chapter VIII.

II. LITERATURE REVIEW

Little is known about the polar low and it is seldom mentioned in meteorological textbooks and publications. The term "polar low" was first introduced by Harley (1960) to describe shallow, intense baroclinic disturbances with scales of about 1000 km which affect Great Britain. Numerous theories have been presented concerning polar low formation and development. To date there is little agreement, and no conclusive evidence, as to the dominant physical processes involved in its life cycle. Traditionally, polar low formation has been attributed to surface heating, or more specifically, to the sensible heat flux through the air-sea interface as cold polar air flows over relatively warm seas.

However, several papers (Harrold and Browning, 1969; Mansfield, 1974; Reed, 1979; Mullen, 1979), have claimed that the polar low is a shallow baroclinic phenomenon of relatively small horizontal scale. Rasmussen (1979), on the other hand, has revived the thermal instability theory, and has proposed that in many cases the polar low is a

manifestation of conditional instability of the second kind (CISK). Reed (1979) investigated cyclones in polar air streams over the North Pacific Ocean and suggested that the polar low is essentially a baroclinic phenomenon, and that CISK cannot be ruled out as a possible contributing factor in its formation and intensification. More recently, Mullen (1982) has documented polar air stream cyclogenesis over the wintertime North American continent. Since similar systems can develop over land in air masses with negligible water content, he concludes that the necessity of CISK for polar low formation and development may be ruled out.

A recognized problem in applying baroclinic instability theory to polar low formation is the short wavelength of these small-scale cyclones. In most theoretical studies of baroclinic theory (e.g., Simmons and Hoskins, 1976), wavelengths on the order of 3000-4000 km at the latitude of England are found to have maximum growth rates. Observed wavelengths of polar lows are typically only one-third of the expected 3000-4000 km.

Authors who claim baroclinic instability as the primary formation mechanism suggest that these phenomenon owe their small horizontal scales to low-level static stability (Reed,

1979; Duncan, 1977) or enhanced low-level baroclinity (Harrold and Browning, 1969). Mullen (1979) points out that theoretical support for baroclinic instability theory as the primary mechanism is offered by Gall (1976) and Staley and Gall (1977). They have shown that basic flows with Richardson numbers significantly lower near the surface than the Richardson number aloft can support greater linear growth rates for small synoptic-scale waves. Therefore, small Richardson numbers, which imply either small static stability or enhanced baroclinity, are theoretically consistent with baroclinic instability theory as a viable physical mechanism in polar low formation.

The role of barotropic instability in the development of polar lows has been given little attention. Polar lows often develop in the strong shear zone poleward of the jet axis, and fulfill the necessary requirement for barotropic instability. Nitta and Yanai (1969) found that the wavelength of maximum instability for a barotropic jet stream depends on the half-width of the jet, and that smaller wavelengths are associated with the narrower jets. Reed (1979) proposes that it is highly unlikely that a jet stream can ever be sharp enough to account for the very

small-scale systems that develop over the oceans in winter. Research by Simmons and Hoskins (1978) on the life cycle of baroclinic waves shows that baroclinic processes dominate during wave growth and that barotropic conversions do not become dominant until after wave growth ceases.

III. DATA BASE

The data base used for this study is comprised entirely of FGGE level III-b data which were assimilated and processed by the European Center for Medium-range Weather Forecasts (ECMWF). Specifically, analyses between 1200 GMT 26 January 1979 and 1200 GMT 29 January 1979 are used to define the development and movement of the polar low.

The international FGGE effort has resulted in the most extensive global atmospheric data set ever collected for use by the meteorological community. More than 7000 temperature sounding profiles from two polar orbiting satellites, and 6000 cloud-track winds from five geostationary satellites were available daily. The Global Weather Experiment met the objective of twice-a-day global measurements of the atmosphere with a 500 km resolution. The conventional observing system included the surface (land, ships, some drifting buoys), rawinsondes, dropsondes, pilot balloons and aircraft data. The satellite and non-satellite data are combined to provide the basis for the complete FGGE data set (Halen et al., 1982).

The northern regions of the North Atlantic Ocean are known to be a data-sparse region. During the FGGE special observing periods, additional data not normally received on a routine basis were gained through pilot reports, AIREPS, some dropsondes, but primarily through an increased number of ship reports in the region. This data coverage for 26 - 29 January 1979, the life span of the storm within this study, is adequate and provides a suitable data base for application of the QLD approach. The data coverage provided by the FGGE special observing period for the life span of this storm is presented in Figs. 1,2 and 3, which are obtained from the Documentation of station plot program, distributed by the Goddard Modeling and Simulation Facility in February 1982.

The data management plan that was put into operation during the FGGE period is described in Fig. 4. This chart shows the flow of data from the instrument signals, level I; the transformation into basic meteorological parameters, level II; and the final merging into a complete global set of basic meteorological parameters, level II-b data set. The 'b' denotes all the data collected within a three-month cut-off period, and contains as a subset the operational

data collected in real time. The real-time data are correspondingly indicated by label 'a'. The level II-b data constitute the basic meteorological product of the Global Weather Experiment.

The data assimilation system used to produce the level III-b data set is a three-dimensional, multivariate optimum interpolation, and an associated automatic system for data checking. The basic idea for optimum interpolation is to determine at each grid point those interpolation weights that gives the best fit of the analysis to the observations. This optimum weight not only depends on the distribution of the observations, but also on the error characteristics of the observations and the first-guess forecast. The quality of the observations is regarded as very good and only very few are considered incorrect and discarded. A 15-level model with a horizontal resolution of 1.875 degrees is used for the dynamical assimilation. The ECMWF level III-b production was completed in June 1981 and analyses at 00 GMT and 12 GMT are available for all standard levels to 10 mb. During the special observing periods, analyses have also been archived at 06 GMT and 18 GMT.

The analyses are available at 15 levels (1000 to 10 mb) and with a horizontal resolution of 1.875 degrees latitude/longitude. The data set contains the basic analysis fields: height, horizontal wind components and sea-level pressure. Fields of temperature, relative humidity and vertical velocity are also included. The temperature field has been calculated from the initialized heights and sea-level pressure, and the vertical velocity from the initialized winds. Finally, the relative humidity has been obtained from precipitable water analyses. Table I illustrates the pressure levels and the data fields available (Bengtsson, et al., 1982). Further information on the FGGE data and its reliability and usefulness within this research is included in Appendix A.

IV. SYNOPTIC DISCUSSION AND NWP PERFORMANCE

A. GENERAL

The polar low in this study evolved on 26 January 1979 from a trough of low pressure near Iceland that was well to the north of the polar front. The storm (Fig. 5) followed a southeasterly track from southwest of Iceland to Ireland over a 72-h period. This case is an excellent example of explosive maritime cyclogenesis in a polar air stream. The polar low involved in this case study is similar to those mentioned by Mansfield (1974), in that an initially small-scale cyclone evolved through explosive deepening into a cyclone with dimensions comparable to middle latitude cyclones.

This polar low development has striking similarities to those prescribed by Petterssen et al. (1962) to be common in maritime cyclogenesis. Specifically, this cyclone develops at low levels under a relatively straight upper current, without appreciable vorticity advection, and in a region of maximum baroclinity. Additionally, the upper cold trough develops simultaneously with the low-level cyclone throughout the period.

Probably the most remarkable feature during the life span of this cyclone is its rapid development, maturation and decay within three days. The following description of these stages in 12-h increments will utilize 250 mb winds and isotachs, 500 mb heights and absolute vorticity, and 1000-500 mb thickness and sea-level pressure analyses. Supplementary satellite imagery will be used to illustrate the more salient features and events.

B. SYNOPTIC DISCUSSION

The meteorological situation at 12 GMT 26 January for the eastern North Atlantic Ocean and the Norwegian Sea is dominated by a vertically stacked low pressure system situated over the central Norwegian Sea. Fig. 6a illustrates this strong cyclonic vortex at 250 mb and the large areal extent over which it influences the circulation pattern. A 45 m/s jet maximum extends across northern France and into central Europe and is directly associated with a polar front moving southeasterly into Europe. Another maximum of 30 m/s with a west-northwestly orientation across Greenland to the Five Fingers region of northwest Iceland, is indicated by broad bands of cirrus on the 2207 GMT 26 January imagery (Fig. 7).

In the lower troposphere, the first significant change in the sea-level pressure (SLP) contours in several days has developed in the form of a east-west oriented trough across Iceland. At 12 GMT 26 January there are no closed isobars and the pressure minimum of 1011 mb is located in the Denmark Strait. Although the National Meteorological Center (NMC) and Fleet Numerical Oceanographic Center (FNOC) analyses at 12 GMT 26 January 1979 indicate no frontal system to the west of Iceland, the gradient of the thickness values in Fig. 6c indicates a strong baroclinic zone. The question may be raised whether the trough of the polar low differs in fundamental respects from a front as mentioned by Reed (1979). Low-level streamlines suggest that this low-level baroclinic zone is the intersection of very cold Arctic air swept across the ice edge with the polar air mass behind the front entering Europe. Cloud patterns in Fig. 7 support this interpretation as cold dry air flows southward from the Greenland ice cap and Davis Strait and swirls cyclonically around Kap Farvel into the northern North Atlantic Ocean and Denmark Strait region.

The southern Greenland ice cap appears as the only distinguishable landmark in Fig. 7. Iceland lies under a

stratus overcast with convective activity occurring to its east. This convective activity east of Iceland is depicted by the broad band of the cold white tops of cumulonimbus.

Additionally, there exists a strong sea-surface temperature (SST) gradient off the southeastern coast of Greenland, as can be seen in Fig. 8. Petterssen et al. (1962) suggest these regions of strong SST gradient are preferred areas for maritime cyclogenesis, and this has been supported by the study of Sanders and Gyakum (1980).

In the mid-troposphere, a north-south oriented trough extends over the United Kingdom. Typical absolute vorticity patterns associated with this flow are depicted in Fig. 6b. Noteworthy is a small perturbation in the $12 \times 10^{-5} \text{ s}^{-1}$ iso-line immediately to the southwest of Iceland. Although little significance can be drawn from this perturbation at this time, its importance will become more apparent as the middle troposphere continues to adjust to changes in low-level temperature advection.

The deepening cyclone at 00 GMT 27 January 1979 has a SLP minimum of 1000 mb, which is a decrease of approximately 11 mb during the preceding 12 h. Satellite imagery at 0124 GMT 27 January (Fig. 9) illustrates a dramatic development

in the cyclone structure during the 3.5 h since the previous imagery. Cyclonic circulation is now most evident to the northwest of Ireland. Convective activity is widespread around the system, especially in the north through southeast sector. Cirrus streaks continue to indicate the presence of high speed winds over the Greenland ice cap, however, the wind direction has shifted to northwesterly.

At 00 GMT 27 January (Fig. 10a), a detached extension of the upper-level wind maximum lies directly over the surface position of the developing low, which has tracked southeasterly to the south of Iceland. The cold advection previously off the Greenland ice cap has translated eastward and has intensified. The tightly packed thickness lines and isobars are nearly perpendicular (Fig. 10c), and reflects this exceptional cold advection southward through the Denmark Strait. Warm advection to the east of the developing cyclone is comparatively weak.

In the middle troposphere (Fig. 10b), a significant change is noticeable in the 500 mb contour pattern. In response to the strong cold advection in the lower levels, troughing is now occurring in the 500 mb pattern near Iceland. This self-amplification has produced greater

curvature in the flow with corresponding vorticity advection changes. A small maximum of $18 \times 10^{-5} \text{ s}^{-1}$ now lies over the southwestern tip of Iceland with the $12 \times 10^{-5} \text{ s}^{-1}$ isoline extending well south of Kap Farvel.

Satellite imagery at 0544 GMT and 1043 GMT 27 January in Figs. 11 and 12, respectively, illustrate the continued rapid development of the surface system and its southeasterly track towards Ireland. The system at 12 GMT 27 January 1979 has a central pressure of 985 mb, which is a decrease of 15 mb during the previous 12 h, and a decrease of 26 mb during the previous 24 h. Convective activity has continued to increase in area and in vigor with very broad continuous bands of cumulonimbus throughout the eastern half of the system. The northerly flow across Iceland has dynamically induced a clearing along the south coast.

The upper-level wind maximum (Fig. 13a) now extends southward from Greenland well into the North Atlantic with its axis situated to the west of the strong polar low. This alignment between surface system and upper level wind maximum will provide significant divergence aloft and will contribute to further deepening of the cyclone. The strong upper level cyclone persists near 65°N and 20°W in the Norwegian Sea.

In the lower troposphere (Fig. 13c), very strong cold advection continues to the west of the polar low as thickness lines have been deformed well to the south of their initial latitudes at 12 GMT 26 January. Warm advection to the east of the cyclone remains relatively weak.

The interaction between the strong low-level advection processes and the consequent response of the middle troposphere is illustrated in Fig. 13b. The self-amplification process is most apparent now, and is markedly reflected by the continued amplification of the northeast-southwest oriented trough south of Iceland and by the consequent development of a significant absolute vorticity maximum within the trough. This newly generated vorticity maximum, located immediately to the northwest of the surface position of the already strong polar low, will provide further impetus toward deepening of the cyclone.

Satellite imagery at 2006 GMT 27 January 1979 (Fig. 14) indicates that the convective activity to the east of this powerful maritime cyclone now blankets most of Ireland and northwest Scotland. By 00 GMT 28 January 1979 (Fig. 15c), the polar low is very near maximum intensity with a central pressure of 976 mb, and is situated immediately to the

northwest of Ireland. Ocean weather ship Lima, stationed near 57.2°N and 20.4°W , or approximately 400 nautical miles south of Iceland, is reporting heavy snow showers accompanied by 21.5 m/s of wind and 7-m seas. The Mariner's Weather Log (July, 1979 issue) states that two ships, the Asia Freighter and the C.P. Discoverer, reported 10- to 11-m seas in the vicinity of 52°N and 16°W .

Although the storm is near peak intensity, the upper-tropospheric flow suggests that further deepening is unlikely and decay processes are imminent. The vorticity maximum at 500 mb (Fig. 15b) has almost overtaken the polar low, with the eastern portion of the absolute vorticity maximum now coincident with the surface system, and the system is quickly occluding up to the jet stream level (Fig. 15a).

Satellite imagery at 1025 GMT 28 January 1979 (Fig. 16) reveals that the center has now become somewhat disorganized and that the bands of convective activity to the east have become less pronounced. By 12 GMT 28 January 1979, the polar low's central pressure has been steady at 976 mb during the previous 12 h. Upper-level cyclogenesis at both the 500 mb and 250 mb levels has occurred and the system is now vertically stacked, as shown in Fig. 17. The absolute

vorticity maximum at 500 mb is now coincident with the surface position of the polar low. Numerous surface observations in the United Kingdom still report shower activity.

During the ensuing 12 h, the polar low drifts eastward and fills 3 mb to a central pressure of 979 mb by 00 GMT 29 January 1979 (Fig. 18). The system remains vertically stacked. Satellite imagery at 0048 GMT 29 January 1979 (Fig. 19) illustrates that the decay process has progressed at a rapid pace. The distinct, vigorous center of only 24 htop before is now extremely disorganized. The center has broken into three weak vortices along the western coast of the United Kingdom. Although numerous cumulonimbus tops are still evident around the low, the convective activity has subdued considerably.

The polar low continued to drift eastward across the United Kingdom by 12 GMT 29 January 1979 (Fig. 20). The central pressure has filled an additional 5 mb and is now 984 mb. The dissipating cyclone will continue to drift easterly. This short-lived, once powerful cyclone eventually dissipates entirely over the continent on the 30th.

C. NUMERICAL WEATHER PREDICTION PERFORMANCE

Numerical prediction models at NMC and FNOC performed poorly in the prediction of this storm's SLP evolution. The inability of the FNOC 36 h SLP forecasts to predict the minimum SLP of the rapidly deepening polar low is illustrated in Fig. 21. Although a deepening rate is apparent in the consecutive forecasts, the magnitude of the deepening was not predicted. Additionally, the model failed to forecast a closed circulation until 00 GMT 29 January, two days after closed SLP isobars were analyzed from FGGE data.

Although a complete set of NMC 36-h surface pressure forecasts is unavailable, those prognoses valid at 12 GMT 26 January, 12 GMT 27 January and 00 GMT 29 January reflect that the NMC products fared as poorly as the FNOC numerical predictions. For example, the NMC 36-h surface prognosis valid at 12 GMT 27 January forecast a trough of low pressure across England and Ireland with pressures varying from 1002-1006 mb. However, the observed central pressure had dropped to 985 mb and the storm had attained a strong cyclonic circulation.

One explanation for these differences may be that the different objective analysis and initialization schemes

employed by NMC and FNOC are significantly different from the initial fields obtained through optimum interpolation at ECMWF. Only subtle differences in the central pressures are found between FGGE, FNOC and NMC analyses of the polar low (Fig. 22). These slight differences disclaim the possibility that the lack of initial surface data is the cause for such gross errors in numerical prediction.

V. QUASI-LAGRANGIAN DIAGNOSTICS

The foremost objective of the quasi-Lagrangian technique (QLD) is the quantitative evaluation of important physical processes involved in extratropical cyclogenesis. Budgets of basic physical parameters such as mass, absolute vorticity (circulation), angular momentum and various energy forms can be computed within a specific atmospheric volume. This budget volume is translated with a distinguishable feature of the system, usually the SLP minimum. This accounts for translational effects in the lateral transport and advection of migratory extratropical cyclones. Additionally, vertical redistributions of the basic parameters within the budget volume as the result of vertical transport processes can be assessed. These inherent features establish the QLD technique as a viable approach to evaluate cyclone development. By contrast, Kung and Baker (1975) evaluated the effects of migratory synoptic-scale systems relative to a fixed volume only.

The basic framework and equations for the QLD approach were developed at the University of Wisconsin by Professor

Donald R. Johnson and his students. Johnson and Downey (1975a) provide an overview of the generalized budget approach; Johnson and Downey (1975b) show the definition and use of storm angular momentum; and Johnson and Downey (1976) give specific cyclone applications of mass and angular momentum budgets. These techniques have proven to be a useful tool in previous studies on extratropical cyclone development. Table II presents a chronological listing of studies employing the QLD approach.

The budget volume is defined by the ten mandatory pressure levels in the vertical and by a variable radius in the horizontal. As applied in this thesis the budget volume is centered over the SLP minimum of the polar low and is translated with the developing system. Two separate radii were selected to represent two budget volumes involved in this study. A radius of four degrees latitude was selected to represent the intense horizontal circulation near the center. A radius of eight degrees of latitude was selected for an outer radius to provide additional information on processes involved in the cyclogenesis.

The generalized budget equation, which is presented in Table III, relates the time rate of change of the property

to lateral transport, vertical transport or sources and sinks of the property within the volume. Budgets of the basic physical parameters such as mass and circulation (vorticity) follow from the generalized budget equation and are presented in Tables IV and V.

Following conservation of mass there are no sources or sinks of mass within the mass budget. The mass budget equation directly relates the mass tendency (dm/dt) to the sum of the lateral transport and vertical transport terms. The lateral transport term represents the mass convergence/divergence and may be considered the primary forcing term to be evaluated within the mass budget. The mass tendency can be directly computed since it is dependent only on the surface pressure tendency, since the pressure at the top of the budget volume remains fixed. Once these terms are computed, the vertical mass transport is determined from the imbalance between the mass tendency and the lateral transport terms.

A computational residual exists due to observational, truncation and interpolation errors. The primary source for this computational residual can be directly attributed to the inability to compute accurately the net lateral mass transport. Corrections to offset these errors must be

applied to individual layer residuals. The largest corrections are applied in the upper troposphere where wind observations are the least accurate. This procedure produces a corrected lateral mass transport field called the corrected mass flux.

The QLD vorticity budget equation, presented in Table V, section A, relates the time rate of change of vorticity directly to lateral and vertical transports, sources and sinks. The budget formulation begins with the calculation of absolute vorticity values at each grid point within the budget volume. Stokes theorem is then employed to relate the area-integrated vorticity to circulation. These calculations combined with vector identities are used to partition the transport terms into advective and divergence components, as presented in Table V, section B. To complete the vorticity budget equation, a source/sink term is incorporated to represent the net generation/dissipation of absolute vorticity within the budget volume due to divergence, tilting and friction terms.

The transport terms of the vorticity budget equation are also partitioned into mean and eddy modes (Table VI). The mean mode reflects the transport of absolute vorticity by

the irrotational component of the wind, and can be associated with changes in absolute vorticity due to synoptic scale mean circulations. Conversely, the eddy mode reflects the transport of absolute vorticity by primarily the rotational component of the wind, and is due to covariances between vorticity deviations and inflow and outflow on the storm boundary.

VI. MASS BUDGET AND STABILITY ANALYSES

A. MASS BUDGET

Quasi-Lagrangian diagnostic mass budget analyses were calculated in 12-h increments using FGGE data fields from 12 GMT 26 January and through 12 GMT 29 January. These time periods span the development, maturation and decay stages of the polar low, as described in chapter IV. Time sections of corrected mass flux and area-averaged omega, representing the horizontal and vertical mass transport, respectively, will be examined in detail in the following subsections. Additionally, the QLD produced vertical motion fields will be compared to those produced via the kinematic method and the ECMWF analysis procedure.

1. Horizontal Mass Transport

Time sections of the corrected mass flux representing the horizontal mass transport for radius four and eight are presented in Fig. 23. Ordinate labels indicate the central pressure level for which layer mass flux computations were performed. For example, the 925 mb level represents the surface to 850 mb layer. The labeled time periods are

viewed in the same manner. For example, the 2718 time period represents the 12 GMT 27 January through 00 GMT 28 January time frame.

A two-layer circulation pattern at radius four is illustrated in Fig. 23a, with a broad layer of outflow overlying a relatively shallow layer of inflow throughout the storm analysis period. The thickness of the convergent layer decreases in vertical extent during the early time periods through 2706 GMT. After this time period the depth of this layer increases as the polar low approaches maturity. By the 2818 GMT time interval, the level of non-divergence (LND) has increased to a maximum height at 450 mb. Beyond this time period the LND gradually lowers. A distinct inflow maximum is seen at 925 mb between the 2709 to 2806 time intervals. This strong low-level convergence correlates well to the period of rapid development as described in chapter IV. An associated upper-level maximum outflow at the 350 mb level occurs between 2718 to 2806 time intervals. The low-level convergence at radius four is quite shallow compared to the larger vertical extent of the upper level divergence. However, the magnitude of the mass flux in the convergence layer is much stronger than the divergence aloft, as required for conservation of mass.

The horizontal convergence and divergence patterns at radius eight are illustrated in Fig. 23b. The basic two-layer circulation pattern observed at radius four is not seen at this radial distance until later time periods. This is indicative of the initial small horizontal scale of the polar low, and the areal expansion of the system in time. The early time periods are influenced by the adjacent anticyclone circulations, but not by the polar low. After the 2718 interval, low-level convergence increases appreciably and acquires maximum strength just after the 2818 time interval. A distinct upper-level divergence pattern develops 24 h in advance of the distinguishable low-level convergence pattern.

Another perspective of the development and areal expansion of the polar low in time can be seen in the spatial variations of the horizontal mass flux within the volume. At 00 GMT 27 January (Fig. 24a) a shallow well-defined region of low-level convergence is centered at the 925 mb level and extends horizontally to radius nine. Above this convergence layer, and beyond radius nine in the horizontal, divergence dominates. A very strong divergence (outflow) maximum exists between radius 11 and 12 near 600 mb.

During the period from 00 GMT to 12 GMT 27 January, the central pressure of the polar low drops at a rate of greater than 1 mb/h. By 12 GMT 27 January, the inflow or convergence region (Fig. 24b) has become more compact. The radial extent of the convergence region has reduced from radius nine to eight and the vertical extent has shrunk from 625 mb to 750 mb. Strong divergence continues at the outer radii from the surface to 500 mb, and a distinct maximum has developed at radius five near the 350 mb level.

By 00 GMT 28 January, the system is near maturity. The inflow region has grown rapidly (Fig. 25a) in both the vertical and horizontal. A secondary maximum centered near the 800 mb level at radius five has formed. The LND has increased to 450 mb, which is some 300 mb higher than 12 h earlier. The divergence at the outer radii has diminished in area and magnitude, however, the divergence maximum centered near 350 mb has intensified. By 12 GMT 28 January, the polar low is fully mature, and a basic two-layer circulation pattern is seen in Fig. 25b.

2. Vertical Mass Transport

Area-averaged vertical motion (ω) fields for the 12 GMT 26 January to 12 GMT 29 January period are presented in Figs. 26-28. These vertical motion fields are a direct response to the strong lateral mass transports in the lower and upper troposphere as described in the previous section. The area-averaged ω fields in Fig. 26 are derived from conservation of mass with boundary conditions of zero vertical motion at the surface and at the top of the volume (100 mb). The kinematic method is used to produce the area-averaged ω fields illustrated in Fig. 27 and the ECMWF analysis area-averaged ω fields are presented in Fig. 28. Although produced by different methods, the basic patterns presented in these figures at both the inner and outer radii are remarkably similar. All figures depict a deep organized layer of upward vertical motion at the inner radii throughout the analysis period, and a much weaker and less organized pattern at outer radii.

The maximum upward vertical motion at the inner radius occurs in each method in the 12 GMT 27 January through 00 GMT 28 January time frame. There are, however, notable differences in the heights of these maxima and the

depth of the organized layer of upward vertical motion at this inner radius. The QLD produced area-averaged omega field (Fig. 26) indicates a vertical velocity maximum near 400 mb. The ECMWF omegas (Fig. 28) have the vertical velocity maximum centered at 500 mb, whereas the kinematic omega (Fig. 27) maximum is in the 700 to 500 mb layer. The top of upward motion region calculated by the mass budget method (Fig. 26) extends considerably higher than for the other methods, and reaches the top of the budget volume by the end of the analysis period.

A much weaker and less organized vertical motion pattern is observed within radius eight in Figs. 26b, 27b and 28b. The ECMWF vertical velocities are the weakest of the omega fields at this radius. The QLD and kinematic area-averaged omega fields reveal an appreciable downward vertical motion during the early time periods, as is especially evident in the kinematic fields. In the early time periods strong subsidence in the middle troposphere associated with the cold air advection to the west of the developing polar low is creating a complex pattern in the area-averaged omega field. This pattern represents the combined influences of the polar low and the following

anticyclone. This complex pattern changes significantly as the system undergoes horizontal expansion in time and the inner processes associated with cyclogenesis become dominant in the larger volume.

B. STABILITY ANALYSIS

As described in chapter IV, cold dry air flows south and southeast across the Greenland ice cap and over the relatively warm waters of the eastern North Atlantic Ocean and Denmark Strait during the early development of the polar low. Surface observations from Prince Christian Sound and Tingmiarmuit, located in extreme south and southeastern Greenland, respectively, quantitatively reflect the atmospheric properties of this air mass. At 12 GMT 26 January, Prince Christian Sound is reporting temperatures of -3°C , a dew point of -6°C and west-northwest winds at 9 m/s. Similar Tingmiarmuit reports are -4°C , -10°C and west-northwest winds at 5 m/s. Sea-surface temperatures (SST) provided in Fig. 8 indicate that the air mass is translating over SSTs of approximately 4 to 6°C . This corresponds to a difference between the air and ocean temperatures of 8 to 10°C (14 to 18°F).

This observed air-sea temperatures and the subsequent rapid intensification of the polar low are consistent with Pyke (1965), who suggests that very intense oceanic cyclogenesis occurs near ice-sea boundaries where the planetary boundary layer is far from equilibrium with ocean surface conditions. Although this imbalance occurs frequently during cold air outbreaks over the eastern North Atlantic Ocean, the rapid intensification of polar lows is quite infrequent. To gain further insight on the role of static stability in the formation of the polar low, the temporal variations in static stability are examined and compared to those obtained from other studies. Additionally, area-averaged potential temperatures fields and their temporal variations will be analyzed.

1. Static Stability

Variations in static stability are directly proportional to the change in potential temperature between pressure levels. Following Sandgathe (1981), the temporal variations in static stability are obtained by simply subtracting the 1000 mb potential temperature from that at 500 mb and dividing by the pressure difference. The computed values serve as a stability index, with higher values

reflecting higher stabilities. Values in Fig. 29 are produced utilizing QLD area-averaged potential temperatures at radii four and eight.

A destabilizing trend of the 1000-500 mb layer is immediately noticable in Fig. 29 from 12 GMT 26 January through 00 GMT 29 January. This trend spans the development and mature stages of the polar low. The initial stability decreases are approximately 0.8°K per 100 mb from 12 GMT 26 January to 00 GMT 27 January, during which a definite cyclonic circulation evolved. This decrease in stability prior to rapid deepening is consistent with numerical simulations by Sandgathe (1981), but is less than half of the initial decrease found by Roman (1981) in his investigation of the President's Day storm. In Calland's (1983) western Pacific Ocean cyclone, initial destabilization was also present prior to maximum deepening. The static stabilities of these three studies were considerably higher throughout the evolution of the storms compared to the stabilities in the polar low. For example, minimum stability indices of 5 and 4.4°K per 100 mb were computed for the President's Day storm and the western Pacific Ocean cyclone, respectively. The maximum observed stability index for the polar low was

4.8 °K per 100 mb occurring prior to the initial destabilization, and the minimum value was 2.1 °K per 100 mb.

The very low stability indices from 00 GMT 28 January through 00 GMT 29 January were explored further using a skew T, log P diagram. The area-averaged potential temperature at 1000 mb at radius four at 12 GMT 28 January is 277 K. Additionally, analysis of FGGE moisture fields indicates near saturation in the lower troposphere. Lifting this parcel moist adiabatically yields a temperature at 500 mb which is 10.7 °K higher than if the parcel is lifted dry adiabatically. This moist adiabatic process corresponds to a stability index of 2.1 °K per 100 mb, whereas the observed stability index was 2.4. At 00 GMT 29 January a stability index of 2.3 is obtained based on a moist adiabatic process compared to an observed value of 2.1 °K per 100mb. This suggests that lapse rates approach moist adiabatic at 12 GMT 28 January and actually become conditionally stable by 00 GMT 29 January.

At 00 GMT 29 January, the system has moved over Northern Ireland with a large portion of the budget volume over land. A sharp stability increase of 1.2 °K per 100 mb is shown in Fig. 29 from 00 GMT 29 to 12 GMT 29 January.

The storm's landfall and consequent sharp rise in stability is associated with a period of very rapid decay, as described in chapter IV.

2. Potential Temperature

To complete the stability analysis, QLD-produced area-averaged potential temperature fields were examined. Fig. 30 illustrates the temporal variations in potential temperatures at radius four and eight. Isentropes for both the inner and outer radius show cooling in the lower troposphere during the development stage of the cyclone. This cooling is also apparent in the middle troposphere, especially at the inner radius. This incursion of cold air into the budget volumes correlates well with the strong low-level temperature advection processes described in chapter IV. After 12 GMT 27 January, warming is observed in the lower troposphere. This warming of the lower troposphere is a destabilizing effect, and results from significant sensible heat transfer from the ocean to the atmosphere as the air flows southward over higher sea surface temperatures. Some warming occurs in the middle troposphere, and can be associated with the latent heat release due to convective activity. The warming in the middle troposphere is small

compared to the marked warming of the lower levels, which indicates that the destabilizing effect of the sensible heat transfer is larger than the stabilizing effect of latent heat release in the middle troposphere.

Fig. 30 also illustrates the hydrostatic response of the tropopause to the temporal variations of heating and cooling in the lower troposphere. The tropopause is indicated by the region of tight packing of the isentropes in the vertical. At 12 GMT 26 January the tropopause is at 275 mb at both the inner and outer radius with temperatures near 315°K at that level. At 12 GMT 28 January the polar low is mature and cold-core, and the tropopause lowers to 450 mb and at 295°K .

C. SUMMARY

To summarize the mass budget and stability analysis, the following results are presented:

- The area-averaged thickness of the convergence layer increases in depth during explosive development. The low-level convergence layer is centered near 925 mb, and is shallow compared to the larger vertical extent of the upper-level divergence;
- The incipient low is small in horizontal scale, and undergoes areal expansion concurrent with rapid development;
- Mass budget, kinematic and ECMWF omega fields reflect similarities in magnitude and pattern, however, each method produces velocity maxima at different levels.

- Area-averaged omega fields at radius eight during the early time periods are influenced by a combination of the polar low and adjacent anticyclones. The inner processes associated with cyclogenesis dominate the later time periods;
- A difference of 8 to 10 °C between air and ocean temperatures is observed during the early development;
- A destabilization trend is apparent throughout the development and mature stages. Destabilization of the lower troposphere prior to rapid development is consistent with numerical studies by Sanigatne (1981);
- Static stabilities are significantly lower throughout the life of the polar low as compared to those observed in similar studies on middle latitude rapid oceanic cyclogenesis. Lapse rates become conditionally stable during the mature stage;
- Isentropes in the lower and middle troposphere indicate cooling during the early development stage, and appreciable warming with the approach of the mature stage. The cooling period is due to strong thermal advective processes. The warming at the lower levels can be attributed to sensible heat gain from the ocean as the polar low has moved southeastward over higher SSTs, and the warming at the middle levels can be associated with the latent heat release due to convective activity.

VII. VORTICITY BUDGET ANALYSIS

A. GENERAL

Quasi-Lagrangian diagnostic absolute vorticity budget analyses were performed using FGGE ECMWF data fields from 12 GMT 26 January and continued in 12-h increments through 12 GMT 29 January. The results of this analysis are presented in this chapter and include comprehensive discussions on the principal contributing terms of the partitioned vorticity budget equation presented in Table V, section B.

Vorticity budget results are illustrated using vertical time sections supplemented by selected vertical profiles. Budget volume radii are identical to those used in the mass budget analysis, with radius four and radius eight representing the inner and outer radius respectively. Time periods denoted in the time sections refer to 12-h periods between synoptic times. Units and contour intervals for all time sections are identical for ease of inter-comparison and interpretation.

B. TIME TENDENCY

The increase in absolute vorticity in the inner budget volume during a period of explosive deepening is illustrated by vertical profiles in Fig. 31. At 12 GMT 26 January, absolute vorticity values are largest in the lower levels of the troposphere and decrease steadily with increasing height to 450 mb. This profile reflects the initial troughing at the surface and the weak ridging aloft, as seen in Fig. 6. During the following 48 h the polar low moves to the south and southeast which results in a loss of planetary vorticity. Despite this negative contribution, a significant increase in absolute vorticity is observed through the column during this time interval. At 12 GMT 27 January, the largest values are still in the lower levels. However, the largest gains during the preceding 24 h are found in the middle and upper levels (600-200 mb). Sharp increases in absolute vorticity at these levels continues during the next 24 h, and by 12 GMT 28 January, the maximum values within the inner budget volume are centered near 300 mb.

A vertical time section (Fig. 32) provides a similar perspective of the rapid increases of absolute vorticity within the inner and outer budget volume. Examination of

Figs. 32a and 32b indicates that the larger gains in absolute vorticity occur at the radius four. Additionally, gains at the radius eight are slower to evolve, and the maximum vorticities occur at later time periods. Steady increases in absolute vorticity in the inner budget volume are observed from 12 GMT 26 January to 00 GMT 28 January. The largest rate of increase appears to be centered on 12 GMT 27 January in the 450 to 900 mb layer, which correlates well temporally to the approach of the mature stage of the polar low. After 12 GMT 28 January slow decreases in absolute vorticity are noticeable as the system decays.

The time rate of change of the cyclone's absolute vorticity within the inner and outer budget volumes is presented in Figs. 33a and 33b. The same vorticity change features discussed above are found in the tendency time sections. At radius four, a distinct maximum is present at the 275 mb level in the 2706 GMT period. This maximum suggests strong upper-level forcing during the development stage, and is consistent with the sharp increases in absolute vorticity observed in Figs. 31 and 32. The time tendency reverses sign after the 2806 GMT time period, which reflects the decay of the storm in time. This negative tendency

appears first in the lower troposphere due to frictional effects, and occurs 12 h later throughout the remaining troposphere. A small decrease maximum is seen centered near the 925 mb level during the 2818 GMT period.

C. LATERAL TRANSPORT

The total lateral transport of absolute vorticity at the inner radius is presented in Fig. 34a. The maximum positive contribution is centered at the 925 mb level and increases in time through the mature stage at 00 GMT 28 January. Beyond the mature stage, an abatement of absolute vorticity transport occurs within this layer as the system decays. A secondary maxima occurs between 450 and 600 mb during the rapid development period. Both maxima correlate temporally with the mature stage of the polar low. At the outer radius (Fig. 34b), inward transport supports the cyclone's vorticity increase, however, this transport is weak and occurs at later time periods when the inner circulation has already begun to decay.

The total lateral transport, as described in Chapter V, can be partitioned into mean and eddy modes. Recall that the mean mode represents the transport of absolute vorticity by the irrotational part of the wind, and transport into the

budget volume is associated with the mean convergent flow. The eddy mode represents transport of absolute vorticity into the budget volume by the covariances of inflow/outflow and vorticity deviations, and arises from asymmetries in the flow about the cyclone.

The separate contributions of the mean and eddy modes to the total lateral transport during a period of rapid intensification are illustrated in Fig. 35. In the lower levels, the total lateral and mean mode transport curves are quite similar, both in trend and magnitude. Above 800 mb, the total lateral transport is the difference between the large negative mean mode and the even larger positive eddy mode. In a similar study of rapid intensification of a western Pacific Ocean cyclone, Calland (1983) also found that the mean mode dominates the lateral transport below 800 mb, and that significant positive eddy mode and negative mean mode contributions are observed in the upper levels. However, the total lateral transport in the upper levels in the western Pacific Ocean cyclone correlates well to mean mode transport, whereas the lateral transport for the polar low correlates more closely with the eddy mode transport.

Alternatively, the total lateral transport of absolute vorticity into/out of the budget volume can be separated into lateral divergence and advection components, which are similar to the mean and eddy modes, respectively. This procedure provides a more traditional vorticity equation viewpoint of the physical processes involved in the rapid development of the polar low. The following subsection will explore and contrast these separate contributions and relate them to synoptic scale features when appropriate.

1. Mean Mode and Lateral Divergence

The vertical-time section illustrating the temporal and spatial variations in the mean mode lateral transport of absolute vorticity is presented in Fig. 36. At radius four (Fig. 36a), a maximum contribution of absolute vorticity is seen at low levels, which is coincident temporally and spatially with the low-level maxima seen in the total lateral transport (Fig. 34a). Values of the low-level maxima for the mean mode are slightly higher than those observed for the total lateral transport. It follows that the eddy mode contribution must be slightly negative in the lower levels. This suggests that the primary, if not sole, contributor to the absolute vorticity build-up from lateral transport into

the lower troposphere arises from the mean cyclonic convergent flow. In the middle and upper troposphere, a loss of absolute vorticity is observed. A broad minimum is centered between 275 and 350 mb, and occurs at the same time periods as the positive maximum which it overlies. At radius eight (Fig. 36b), there are similar, but weaker contributions, and the maxima/minima are found at later times.

The lateral divergence component representing the inner radius is presented in Fig. 37a. This illustration depicts a basic two-layer regime with a broad region of divergence overlying a relatively strong convergence region. The upper-level outflow and the low-level inflow maxima are both temporally situated between the 2706 GMT and the 2806 GMT time periods, and are spatially located between the 275 to 350 mb levels and at the 925 mb level, respectively. These features reflect strong similarities to the horizontal mass fluxes within the inner budget volume described in chapter VI (Fig. 23a). The lateral divergence component at radius eight (Fig. 37b) reveals a similar structure to that seen at the inner radius, although the magnitudes of the divergence and convergence are much weaker. A weak divergence pattern overlies a convergence region throughout the

time periods. The convergence region strengthens during the later time periods but the values are much smaller than in the strong, well-organized convergence layer of the inner budget volume. The temporal and spatial gain in absolute vorticity through 2806 GMT in the lower troposphere is consistent with the positive mass fluxes at the outer radius (Fig. 23b) during the same time periods. This evolution is another indication of the initially small areal scale of the polar low and its areal expansion concurrent with the explosive development.

Comparison of the lateral divergence (Fig. 37) and the mean mode (Fig. 36) reveals strong similarities temporally, spatially and in magnitudes. These periods of distinct inflow of absolute vorticity in the lower levels and corresponding outflow aloft coincide with rapid pressure falls and increased circulation, as described in chapter IV.

2. Eddy Mode and Lateral Advection

The eddy mode contribution to the total lateral transport is presented in Fig. 38. As in previous budget analysis illustrations, it is clear that the inner radius (Fig. 38a) budget reflects the dynamics and physical processes involved in the rapid cyclogenesis, and that these

processes at the outer radius (Fig. 38b) are distorted due to the incorporation of adjacent synoptic scale features into the outer budget volume. This occurs because of the small horizontal scale of the polar low.

At radius four (Fig. 38a) there is a slightly negative contribution from the eddy mode in the lower troposphere. However, in the upper troposphere there is a strong positive maximum centered near 350 mb, especially between the 2706 and 2718 periods. This corresponds to the time periods of a jet streak incursion into the budget volume, as described in Chapter IV and amplified in Appendix B. Additionally, the largest SLP falls and circulation increases are observed during this time interval. Beyond this time the eddy mode contribution aloft diminished with time, and the polar low began to decay.

The presence of an eddy mode maximum in the upper layers, and its temporal relationship to periods of rapid SLP falls and vigorous increases in surface cyclonic circulation, closely agree with similar findings by Calland (1983) in his study of a rapid cyclogenesis in the western Pacific Ocean. Wash (1978) emphasizes the significant role of eddy mode transports in cyclogenesis, and suggested that

poor Limited Fine Mesh (LFM) forecasts of several midwest cyclones resulted from an inability to resolve accurately the eddy mode transports in the model.

The lateral advection of absolute vorticity for both the inner and outer budget volumes (Fig. 39) show striking similarities to the eddy mode transport (Fig. 38). At the inner radius (Fig. 39a), a maximum in positive vorticity advection (PVA) is temporally and spatially coincident with the maximum seen in the eddy mode transport (Fig. 38a) in the upper troposphere. Additionally, concentric values seen around these maxima are almost identical in magnitude. This shows that the upper-level PVA results from advection of the cyclonic shear poleward of the jet streak, and that the jet streak incursion into the inner budget volume is the dominant contributor to upper-level absolute vorticity increases. In the lower troposphere, both the lateral advection and eddy mode transports reflect negative vorticity advection (NVA).

D. VERTICAL REDISTRIBUTION

As presented in the previous section, significant absolute vorticity increases observed in the lower troposphere can be attributed to the mean cyclonic convergent flow.

Similarly, strong increases in absolute vorticity at the upper levels can be attributed to the incursion of a jet streak into the budget volume. This section will explore the role of vertical redistribution of absolute vorticity from the lower and upper levels of the troposphere into the middle levels, where the larger gains are observed during rapid intensification (Fig. 31).

The vertical redistribution of absolute vorticity is represented in the partitioned form of the vorticity equation (Table V, section B) by the divergence of the vertical transport. The divergence of the vertical transport is a vertical derivative of the transport between pressure levels, which was computed using the kinematic vertical velocities. The vertical-time section of the divergence of the vertical transport is presented in Fig. 40. At the inner radius (Fig. 40a), a two-layer circulation is depicted with strong transport of absolute vorticity from the lower levels into the middle and upper troposphere. A maximum region of divergence of the vertical transport occurs between the 2718 and 2806 GMT time interval, and is spatially centered at the 925 mb level. This maxima naturally correlates well with the period of maximum vertical velocities illustrated in

Fig. 27. Convergence of absolute vorticity is noticed in the middle and upper levels throughout the time section with a maximum located at the 350 mb level during the 2806 GMT period.

At the outer radius (Fig. 40b), a more complex pattern is seen. It is apparent that adjacent synoptic features dominate the larger volume until the 2718 GMT period. After this time period, an upward transport of absolute vorticity from the lower levels to the middle troposphere is observed. The values at this outer radius are significantly smaller than those observed at the inner radius, and occur at later time periods.

As was the case with the lateral transport terms, the divergence of the vertical transport can be partitioned into the more traditional vertical advection and divergence components. The vertical divergence component is the negative of the divergence component of the lateral transport so they cancel. The spatial and temporal variations in the vertical divergence component are presented in Fig. 41. A cursory inspection of Figs. 40 and 41 indicates that the vertical divergence component is the principal contributor to the divergence of the vertical transport, and this shows that

vertical advection of absolute vorticity plays a relatively unimportant role. Examination of the vertical advection component (Fig. 42) at the inner radius markedly reflects this insignificant contribution to cyclone development. Values in the outer volume were too small for graphical depiction. This dominance of the vertical divergence component in the vertical redistribution of absolute vorticity, and the relatively insignificant role of vertical advection, agree with findings by Calland (1983) in his study of a western Pacific Ocean cyclone.

E. SOURCES AND SINKS

In the partitioned form of the vorticity budget equation (Table V, section B), the source/sink term is comprised of the horizontal divergence, tilting and friction terms. The horizontal divergence and tilting terms can be sources or sinks of vorticity, and the friction term is only a sink. Holton (1979) states that the generation of absolute vorticity by horizontal divergence is the fluid analog of the change in angular velocity, which results from a change in the moment of inertia when angular momentum is conserved. If positive horizontal divergence exists and circulation is conserved, the area enclosed by the parcel will increase and

the absolute vorticity must decrease. Similarly, a region of horizontal convergence will generate absolute vorticity when circulation is conserved. Additionally, Holton attributes the vertical vorticity generation to the tilting of horizontally oriented components of vorticity by a non-uniform vertical motion field.

The horizontal divergence referred to within this section is identical to the divergence component of the lateral transport of absolute vorticity previously discussed (Fig. 37). A region of strong convergence is seen in the lower levels at radius four (Fig. 37a), and reflects significant cyclonic vorticity generation within the lower troposphere. Similarly, the broad divergence region centered at the 350 mb level contributes to significant negative vorticity tendencies aloft. The maxima in low-level vorticity generation is temporally centered near the 2718 GMT time period, however, the maximum contribution to upper-level vorticity decreases occurs later during the 2806 GMT period. Similar, but weaker patterns exist at the outer radius (Fig. 37b), and occur at later time periods.

Vertical vorticity generation due to the tilting term (Fig. 43) plays an unimportant role in the cyclone

development. Only small losses of absolute vorticity at radius four are noticed in the middle troposphere (600 mb) between the 2706 and 2718 GMT periods. Values for the tilting term observed at the outer radius are negligible, and an illustration is not included.

The negative contribution, or sink of absolute vorticity within the budget volume, due to friction is calculated using a stability independent parameterization (Johnson and Downey, 1976). This dissipation of absolute vorticity within the lower layer of the troposphere is illustrated in Fig. 44. The influence of friction is confined to the layer below 775 mb, and is a more dominant feature at the inner volume (Fig. 44a) than at the outer volume (Fig. 44b). A maximum in frictional dissipation is observed at the 925 mb level, and occurs between the 2806 and 2818 GMT periods. Temporally, this corresponds to the beginning of the decay cycle of the polar low and subsequent rises in central pressures.

The frictional dissipation of absolute vorticity has a severe retarding effect on the lateral transport processes in the lower troposphere. For example, the total lateral transport (Fig. 34a) between 2718 and 2806 GMT has a maximum

value of $12 \times 10^{-10} \text{ s}^{-2}$ centered at 925 mb. The frictional dissipation (Fig. 44a) calculated for the same time period and level is approximately $10 \times 10^{-10} \text{ s}^{-2}$. Subtraction of these opposing tendencies yields a net effective lateral transport of only $2 \times 10^{-10} \text{ s}^{-2}$. Therefore frictional effects in the lower levels clearly negate to a considerable degree the otherwise quite significant contribution of the lateral transport of absolute vorticity. The frictional effects in the middle and upper troposphere, however, are insufficient to offset the vorticity generating mechanisms, and allows more rapid increases in absolute vorticity at these levels.

F. RESIDUALS

Vorticity budget residuals arise from interpolation and truncation errors, as well as from unresolved physical processes not incorporated into the vorticity budget equation. The residuals serve to measure the integrity of the vorticity budget calculations. Positive residuals indicate a vorticity excess, or vorticity that is not accounted for by the calculations with the present data set and this formulation of the physical processes (e.g. the parameterization of the frictional processes). Similarly, negative

values indicate smaller values of absolute vorticity than computed.

At radius four (Fig. 45a), a complex pattern of residuals is illustrated. In the upper levels, a dual-center maxima is located near the 250 mb level. A similar pattern in the upper troposphere was calculated by Calland (1983) during a period of rapid intensification of a western Pacific Ocean cyclone. Calland suggested that these excesses are the result of improper representation of intense mesoscale convective activity, and a subsequent underestimation of vertical redistribution processes. It must be noted that it is extremely difficult to isolate specific causes for the residuals within the budget volume. However, misrepresentation of mesoscale convective activity remains a plausible explanation for the vorticity excesses observed in the upper troposphere and the deficits observed at middle levels. No appreciable residuals are observed at the outer radius (Fig. 45b).

G. SUMMARY

The purpose of this section is to interrelate many of the processes discussed in the previous sections. The summarize the vorticity budget, the following results are noted:

Lower troposphere

- The mean convergent flow (mean mode) dominates the total lateral transport below 800 mb. However, this low-level lateral transport of absolute vorticity is nearly offset by frictional dissipation of vorticity;
- Significant lower tropospheric absolute vorticity increases were shown to occur primarily from the source divergence term; and
- The vertical divergence component of the vertical transport is the primary mechanism in the transport of absolute vorticity from the lower levels to the middle and upper levels.

Upper troposphere

- The most rapid increases in absolute vorticity occur at 2706 GMT in the 250 to 300 mb layer, which correlates well to a period of rapid surface pressure falls and vigorous circulation increases;
- Eddy mode transport and PVA transport components are the dominant contributors of absolute vorticity in the upper levels, and are associated with the incursion of a jet streak into the budget volume;
- Upper tropospheric increases in absolute vorticity due to jet streak propagation into the budget volume and vertical redistribution processes offset the strongly negative contributions of upper level divergence;
- The largest surface pressure falls and circulation increases are temporally coincident with the occurrence of the eddy mode and PVA maximum; and
- The eddy mode and PVA contribution aloft diminishes with occlusion and the polar low begins to fill and decay.

VIII. CONCLUSIONS AND RECOMMENDATIONS

Dynamical and physical processes involved in a rapid intensification of a polar low were investigated using quasi-Lagrangian diagnostic techniques. Specifically, mass and absolute vorticity budgets were calculated for a North Atlantic polar low utilizing ECMWF FGGE level III-b data fields. Significant budget features were examined and correlated to observed synoptic patterns.

The following key results are presented:

- The incipient cyclone develops within a low level baroclinic zone overlying a sea-surface temperature gradient. No appreciable mid-level positive vorticity advection was observed;
- Initial destabilization of the lower troposphere preceding rapid intensification is attributed to strong low level advection of cold air over relatively high sea surface temperatures. The resulting low static stabilities and enhanced low-level baroclinity support a shift of maximum growth rate to shorter wavelengths, as prescribed in theory.
- The polar low is initially small in horizontal scale, and undergoes areal expansion concurrent with rapid development;
- Rapid surface pressure falls and vigorous circulation increases correlate well with the observed maxima in low level inward mass transport and upper level mass outflow;
- Mean convergent flow dominates the total lateral transport of absolute vorticity below 800 mb, however, frictional forces seriously retard this contribution. The more significant gains in low level absolute vorticity occur primarily from the divergence source term;
- The most rapid observed surface pressure falls and circulation increases are coincident temporally with

the incursion of the forward divergence quadrant of a jet streak into the budget volume. This fundamental contribution of shear vorticity, combined with vertical redistribution of absolute vorticity from lower levels, offsets the strong upper level losses due to divergence; and

- An oscillatory temperature pattern with spurious warming and cooling regions below 350 mb in the 06 and 18 GMT ECMWF analysis was discovered.

Recommendations for further research:

- Further efforts should be made to isolate the diabatic heating contributions such as sensible heat fluxes through the air-sea interface and latent heat release due to convection;
- A broad climatological study should be conducted to gain more conclusive correlations between jet streak superpositioning and rapid maritime cyclogenesis; and
- An in-depth investigation should be conducted into the oscillatory nature of the ECMWF FGGE temperature analysis.

APPENDIX A

FGGE DATA RELIABILITY

Major inconsistencies discovered in the 06 and 18 GMT ECMWF FGGE temperature fields precluded efforts to study the evolving cyclone in 6 h time increments. Therefore, QLD mass and vorticity budget analyses (Chapters VI and VII), as well as synoptic illustrations referenced in Chapter IV, were prepared utilizing only the 00 and 12 GMT FGGE data fields. These data were found to be suitable for this research effort, and no major discrepancies were noted.

The 06 and 18 GMT data problem was first discovered during analysis of the 6-h area-averaged potential temperatures (Fig. 46). Notice the oscillatory patterns of warming and cooling below 350 mb, especially at the inner radius (Fig. 46a). Following the inner volume 275 and 280 °K isentropes would suggest spurious warming at 2706, 2718 and 2818 GMT interspersed with periods of rapid cooling at 2806 and 2906 GMT. Other inconsistencies are seen throughout the inner volume time section, but perhaps the most glaring evidence of erroneous temperature data is suggested by the sudden warming near the 450 mb level at 2906 GMT. Similar

wavelike patterns of warming and cooling are seen in the outer volume (Fig. 46b), and are particularly evident in the temporal variations of the 275 and 295 °K isentropes. There are no plausible physical explanations for these undulating thermal tendencies from the synoptic patterns.

It follows that the 06 and 18 GMT data problem will also lead to a misrepresentation of stability tendencies. This misrepresentation is clear when comparing the 6-h stability trace (Fig. 47) to the 12-h trace (Fig. 29). The 6-h trace suggests a marked stabilization from 00 GMT to 06 GMT 28 January, followed by an equally strong destabilization period over the next 6 h. Similarly, an anomalous pattern of rapid stabilization and destabilization is suggested during the 00 to 12 GMT 29 January period.

These problems encountered with the 06 and 18 GMT data prompted the decision to employ a 12-h time increment for budget analyses, thereby eliminating the 06 and 18 GMT data fields from the budget calculations. However, a 6-h vorticity budget was run to document the impact of the erroneous data on budget formulations. Comparison of the 6-h absolute vorticity time tendency (Fig. 48a) to the 12-h time tendency (Fig. 33) reveals some similarities, but the trends

that are evident in the 12-h plots are obscured by the oscillatory components in the 6-h plots. The incorporation of the 06 and 18 GMT data into budget calculations has created a checkerboard pattern of absolute vorticity gains (maxima) and losses (minima) in the 6-h time tendency. This pattern by no means accurately describes the volumetric gains/losses of absolute vorticity expected in this study of a rapid cyclogenesis. Similarly, an oscillatory pattern is observed in the 6-h budget residuals (Fig. 48b), where alternating periods of vorticity excesses and deficits are seen throughout the time section. A residual pattern such as this in the budget calculations and analyses has little credibility.

A brief investigation was conducted to determine a possible cause of the temperature bias at 06 and 18 GMT. There are few temperature observations in the lower and middle levels of the troposphere due to the following:

- No rawinsonde soundings, which are only released at 00 and 12 GMT;
- Lack of aircraft reports, since aircraft normally transit the North Atlantic at much higher altitudes; and
- Temperature soundings from polar orbiting satellites are sparse and intermittent.

Therefore, only a few temperature observations are available in the lower and middle troposphere as input to adjust the first guess from the model. Calland (1983) and Paegle (1983) have also documented a FGGE temperature bias, and add support to the 06 and 18 GMT temperature inconsistencies encountered in this study.

APPENDIX B

JET STREAK INTERACTION

As described in Chapter VII, an inner volume maximum in eddy mode transport (Fig. 38a) occurs in the 250 to 300 mb layer, and correlates well to rapid surface pressure falls and vigorous circulation increases. Additionally, the eddy mode transport and the vertical redistribution processes offset the strongly negative contributions from upper level divergence, and thereby enhance the development of the polar low. To further investigate the fundamental role of upper-level forcing, a more detailed analysis of the 300 mb winds and isotachs was performed. Special attention is given to the superpositioning of the jet streak features in relation to the evolving polar low.

At 12 GMT 26 January, the polar low is a shallow depression located immediately to the southwest of Iceland (Fig. 6c). Analysis of 300 mb winds and isotachs (Fig. 49a) indicates straight, northwesterly flow over the incipient cyclone, and a 40 m/s jet streak upstream across western Greenland. By 18 GMT 26 January (Fig. 49b) the leading edge of this jet streak extends to the southeast coast of

Greenland, and a decrease in horizontal distance between the surface low and the jet streak is noticed. This approach of the upper level jet streak is also reflected in significant increases in eddy mode transport (Fig. 38a). During the next 6 h, the jet streak continues to propagate downstream, and by 00 GMT 27 January (Fig. 50a) the maximum is over the east coast of Greenland.

During the period from 12 GMT 26 January to 00 GMT 27 January, the surface low has evolved a closed circulation, and has experienced a 11 mb decrease in central pressure (Fig. 10c). The ensuing 12-h time period marks the most dramatic central pressure falls (15 mb) and circulation increases. Additionally, a maximum in positive vorticity tendency occurs in the 250 to 300 mb layer (Fig. 33a) during this time interval. This can be explained by the rapid approach of the jet streak and, consequently, a strong eddy mode transport of absolute vorticity in the upper levels. By 06 GMT 27 January (Fig. 50b) the jet streak has continued to propagate rapidly to the south-southeast with the polar low located below the left front quadrant of the jet streak at this time. The strong cyclonic shear and divergence associated with this quadrant enhances mass compensation

(increased vertical velocities) from lower levels, which is consistent with the surface pressure falls. By 12 GMT 27 January (Fig. 51a) the strong polar low has moved in a more easterly direction away from the jet streak, however, substantial upper level cyclonic shear aloft is still observed.

By 18 GMT 27 January (Fig. 51b), the polar low has continued to move to the east. The polar low is occluding at upper levels and the corresponding abatement in eddy mode transport of absolute vorticity into the upper troposphere (Fig. 38a) is observed beyond this time. The polar low matures and becomes vertically stacked (Figs. 15 and 52a) by 00 GMT 28 January. Beyond this time period (Fig. 52b), the polar low drifts to the east and begins to decay.

APPENDIX C

TABLES

TABLE I

Fields Archived in the ECMWF Level III-b Data Set

(From Bengtsson, 1982)

	Z	U	V	T	W	RH
10mb	x	x	x	x	x	
20mb	x	x	x	x	x	
30mb	x	x	x	x	x	
50mb	x	x	x	x	x	
70mb	x	x	x	x	x	
100mb	x	x	x	x	x	
150mb	x	x	x	x	x	
200mb	x	x	x	x	x	
250mb	x	x	x	x	x	
300mb	x	x	x	x	x	x
400mb	x	x	x	x	x	x
500mb	x	x	x	x	x	x
700mb	x	x	x	x	x	x
850mb	x	x	x	x	x	x
1000mb	x	x	x	x	x	x

TABLE II
Previous QLD Studies

(Extracted in part from Wash, 1978)

<u>PROPERTY</u>	<u>RESEARCHER(S)</u>
Available potential Energy	Spaete 1974
Circulation	Wash 1975
Mass	Johnson and Downey 1976
Absolute Angular Momentum	Johnson and Downey 1976
Kinetic Energy	Chen and Bosart 1977
Absolute Angular Momentum	Wash 1978
Mass	Roman 1981
Mass	Tallman 1982
Circulation and Angular Momentum	Conant 1982
Mass and Circulation	Calland 1983

TABLE III
Generalized Budget Equation
(After Wash, 1978)

$$F = \int_{1000 \text{ mb}}^{100 \text{ mb}} \int_0^\beta \int_0^{2\pi} \frac{1}{g} f r^2 \sin\beta \, d\alpha d\beta \, (-dp)$$

where F is the volume integral of the desired budget property f .

The budget equation is

$$\frac{\delta F}{\delta t} = LT(F) + VT(F) + S(F)$$

where the lateral transport is

$$LT(F) = \int_{1000 \text{ mb}}^{100 \text{ mb}} \int_0^{2\pi} \frac{1}{g} (U-W)_\beta f r \sin\beta \, d\alpha (-dp) \Big|_\beta$$

and the vertical redistribution is

$$VT(F) = \int_{1000 \text{ mb}}^{100 \text{ mb}} \int_0^\beta \int_0^{2\pi} \frac{1}{g} \frac{\partial}{\partial p} (\omega f) r^2 \sin\beta \, d\alpha d\beta \, (-dp) .$$

The source/sink term is

$$S(F) = \int_{1000 \text{ mb}}^{100 \text{ mb}} \int_0^\beta \int_0^{2\pi} \frac{1}{g} \frac{df}{dt} r^2 \sin\beta \, d\alpha d\beta \, (-dp) .$$

TABLE IV
Mass Budget Equation
(After Wash, 1978)

The Definition

$$M = \int_{V_p} \frac{1}{g} r^2 \sin\beta \, d\alpha d\beta dp$$

where $f = 1$.

The Budget Equation

$$\frac{dM}{dt} = LT + VT,$$

where

Lateral Transport

$$LT = - \int_{\eta_B}^{\eta_T} \int_0^{2\pi} \frac{1}{g} (U-W)_\beta \, r \sin\beta_B \, d\alpha dp \Big|_{\beta_B}$$

Vertical Transport

$$VT = \int_0^{\beta_B} \int_0^{2\pi} \frac{1}{g} (\omega - \omega_B) \, r^2 \sin\beta \, d\alpha d\beta \Big|_p$$

where

$$\omega = \frac{dp}{dt}, \quad \omega_B = \frac{dp_B}{dt}.$$

TABLE V
Circulation Budget Equation

(After Wash, 1978)

Section A

$$C_a = \int_{1000 \text{ mb}}^{100 \text{ mb}} \int_0^\beta \int_0^{2\pi} \frac{1}{g} \zeta_a r^2 \sin\beta \, d\alpha d\beta \, (-dp)$$

where C_a is the absolute circulation and ζ_a is absolute vorticity.

The budget equation is

$$\frac{\delta C_a}{\delta t} = LT(\zeta_a) + DVT(\zeta_a) + S(\zeta_a)$$

where the lateral transport is

$$LT(\zeta_a) = \int_{1000 \text{ mb}}^{100 \text{ mb}} \int_0^\beta \int_0^{2\pi} \frac{1}{g} (\underline{U}-\underline{W})_\beta \zeta_a r \sin\beta \, d\alpha (-dp) \Big|_\beta$$

and the divergence of the vertical transport is

$$DVT(\zeta_a) = \int_0^\beta \int_0^{2\pi} \frac{1}{g} \frac{\partial}{\partial p} (\omega \zeta_a) r^2 \sin\beta \, d\alpha d\beta .$$

The source/sink term is

$$S(\zeta_a) = \int_{1000 \text{ mb}}^{100 \text{ mb}} \int_0^\beta \int_0^{2\pi} \frac{1}{g} \frac{d\zeta_a}{dt} r^2 \sin\beta \, d\alpha d\beta (-dp) .$$

TABLE V. (Cont.)

Section B

The partitioned form of the vorticity budget equation is

$$\frac{\delta(\zeta_a)}{\delta t} = + \text{LT}(\zeta_a) + \text{DVT}(\zeta_a) + S(\zeta_a)$$

$\begin{array}{c} \text{mean mode} \quad \text{eddy mode} \end{array}$
 $\begin{array}{c} \text{vertical divergence} \quad \text{vertical advection} \end{array}$
 $\begin{array}{c} \text{divergence term} \quad \text{tilting term} \quad \text{frictional dissipation} \end{array}$
 $\begin{array}{c} \text{horizontal divergence} \quad \text{horizontal advection} \end{array}$

The above partitions make use of Stokes' theorem

$$\oint \zeta_a \underline{U} \cdot \underline{m} \, d\ell = \iint_A \nabla \cdot \zeta_a \underline{U} \, dA,$$

and the division of total flux ($\underline{U} \zeta_a$) into divergent and advective components,

$$\nabla \cdot \zeta_a \underline{U} = \zeta_a (\nabla \cdot \underline{U}) + \underline{U} \cdot \nabla \zeta_a.$$

TABLE VI
Mean and Eddy Modes
(After Conant, 1982)

$$EM(C_a) = \int_{1000 \text{ mb}}^{100 \text{ mb}} \int_0^{2\pi} \frac{1}{g} \zeta_a^* (\bar{U}-\bar{W})_\beta r \sin\beta \, d\alpha (-dp) \Big|_\beta$$

$$MM(C_a) = \int_{1000 \text{ mb}}^{100 \text{ mb}} \int_0^{2\pi} \frac{1}{g} \bar{\zeta}_a^a (\bar{U}-\bar{W})_\beta^\alpha r \sin\beta \, d\alpha (-dp) \Big|_\beta$$

$$EM(G_a) = \int_{1000 \text{ mb}}^{100 \text{ mb}} \int_0^{2\pi} \frac{1}{g} \overline{g_a^* (\bar{U}-\bar{W})_\beta^\alpha} r \sin\beta \, d\alpha (-dp) \Big|_\beta$$

$$MM(G_a) = \int_{1000 \text{ mb}}^{100 \text{ mb}} \int_0^{2\pi} \frac{1}{g} \bar{g}_a^a (\bar{U}-\bar{W})_\beta^\alpha r \sin\beta \, d\alpha (-dp) \Big|_\beta$$

EM is the eddy mode and MM is the mean mode.

Note that $(\bar{\quad})^\alpha = \frac{1}{2\pi} \int_0^{2\pi} (\quad) d\alpha$

and $(\quad)^* = (\quad) - (\bar{\quad})^\alpha$ is the deviation of the property from its mean around a lateral boundary.

APPENDIX D

FIGURES

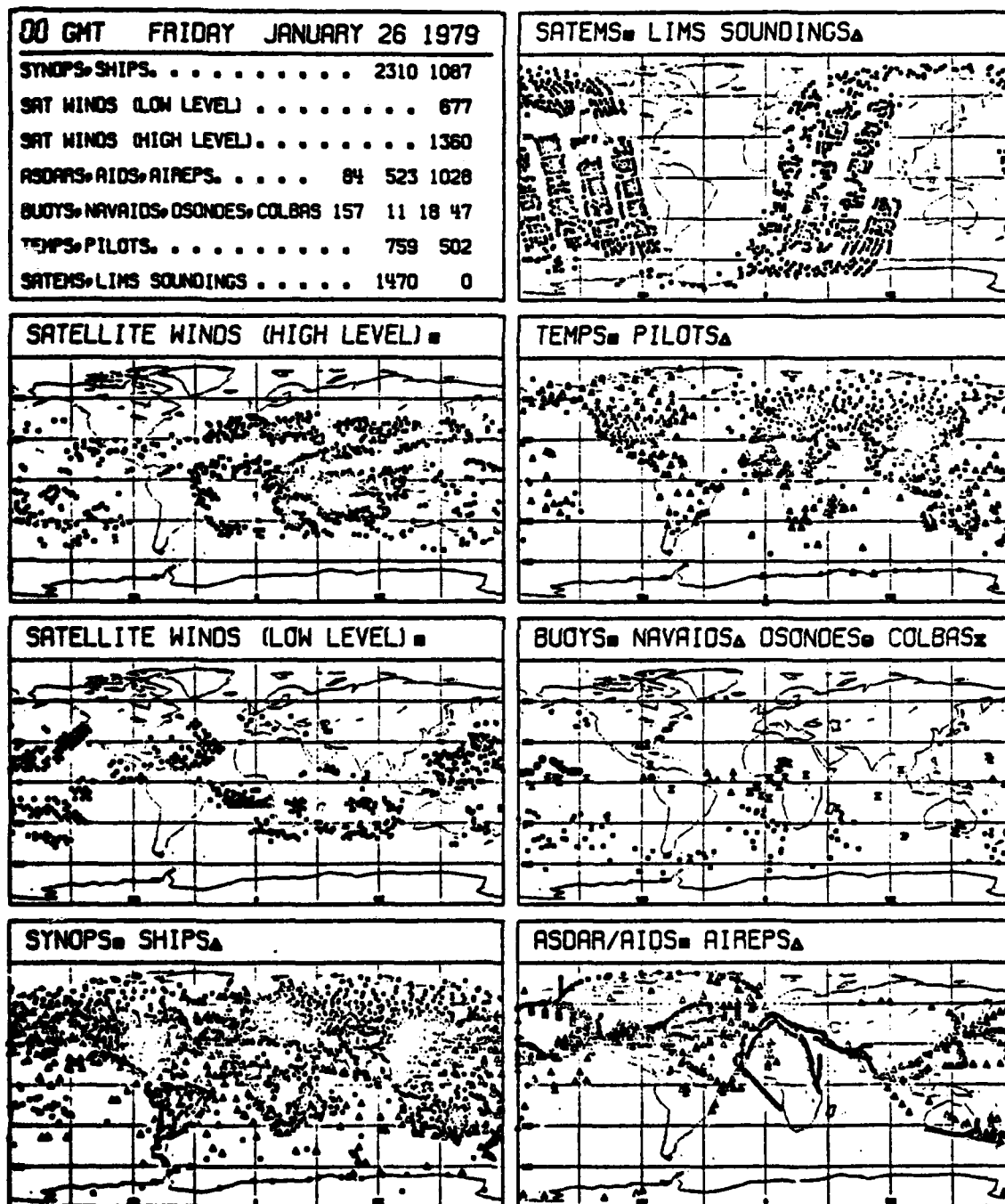


Figure 1. PGGE Data Coverage 00 GMT 26 January 1979 (From Documentation of Station Plot Program)

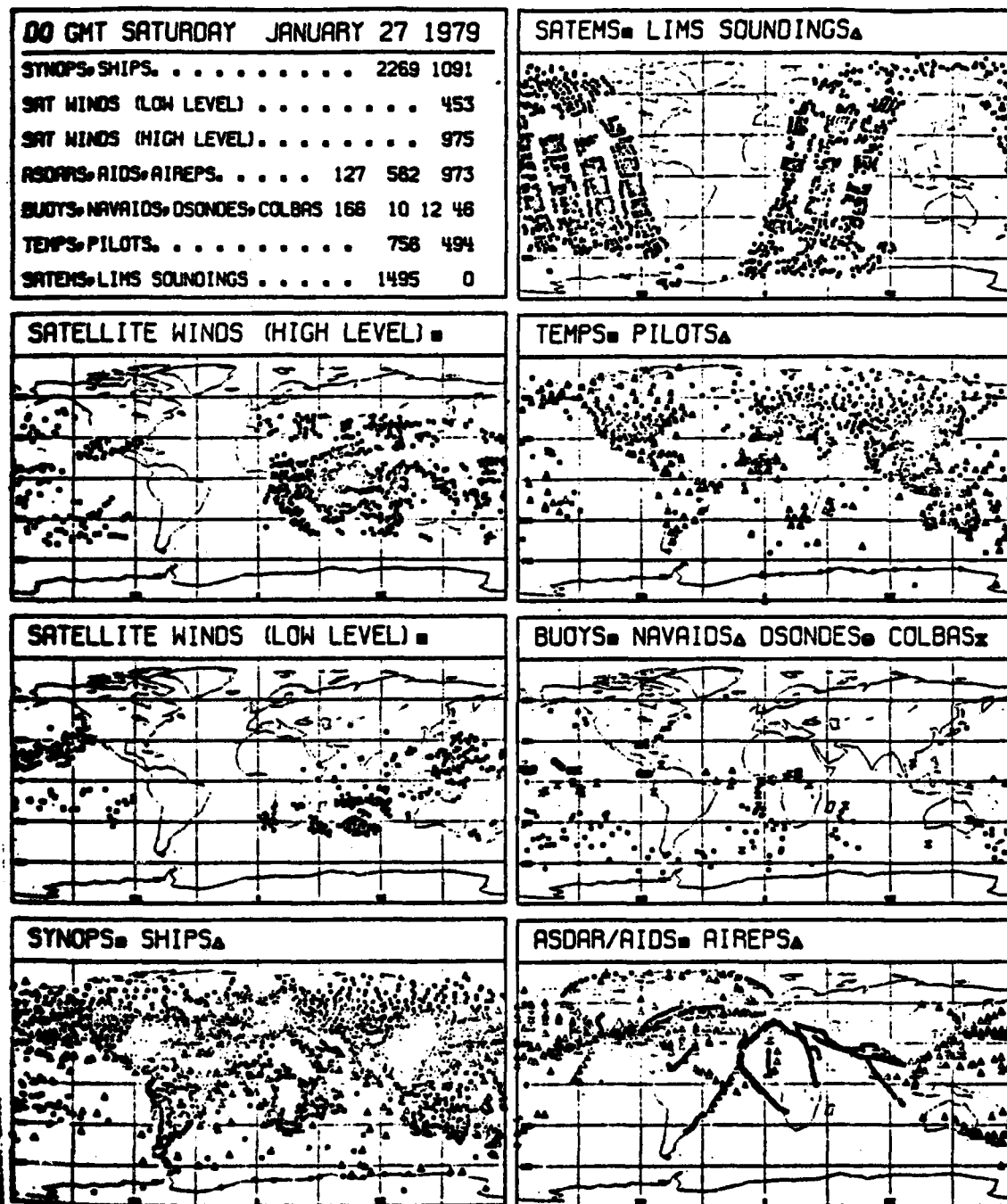


Figure 2. Similar to Figure 1 except for 00 GMT 27 January 1979

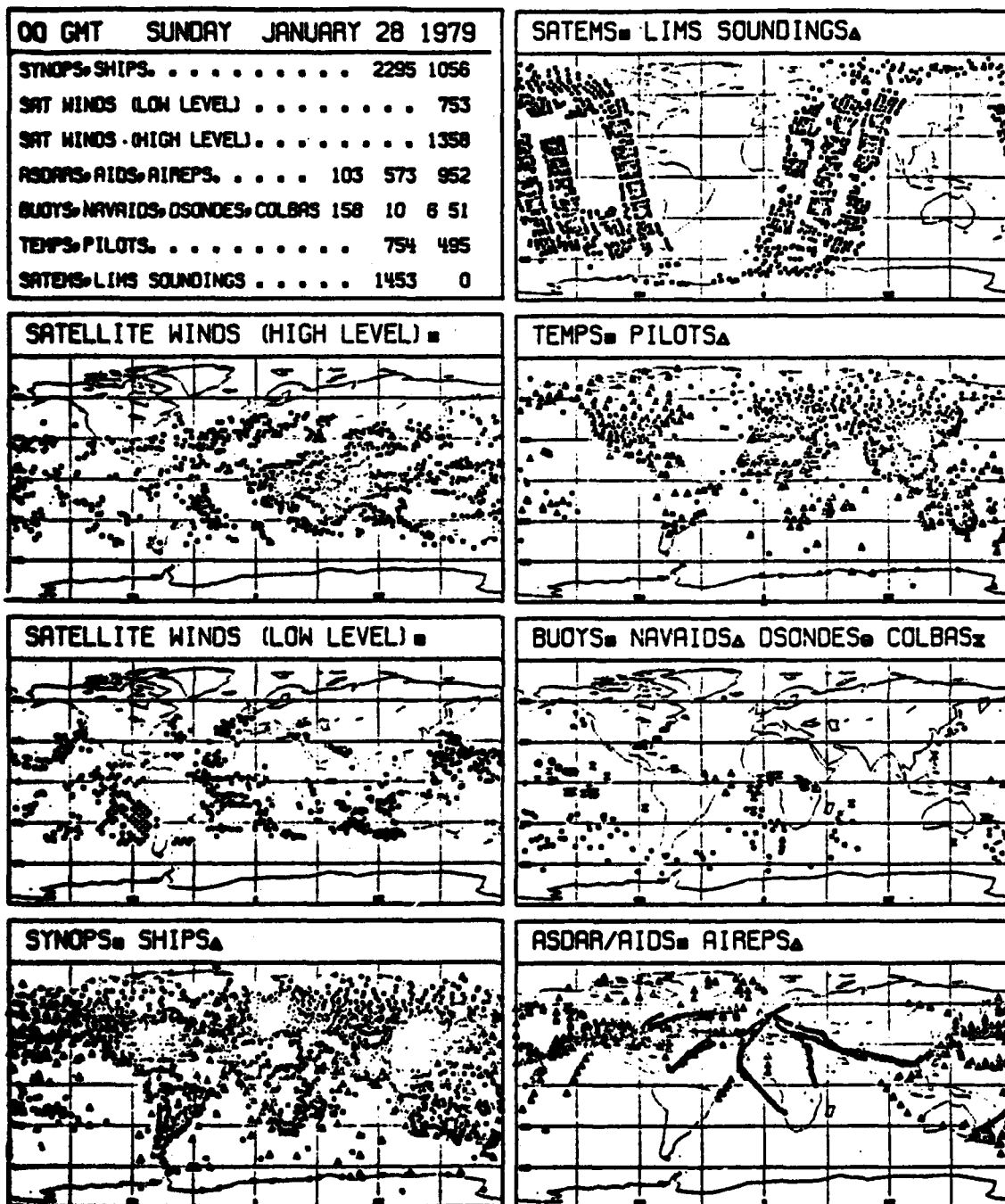


Figure 3. Similar to Figure 1 except for 00 GMT 28 January 1979

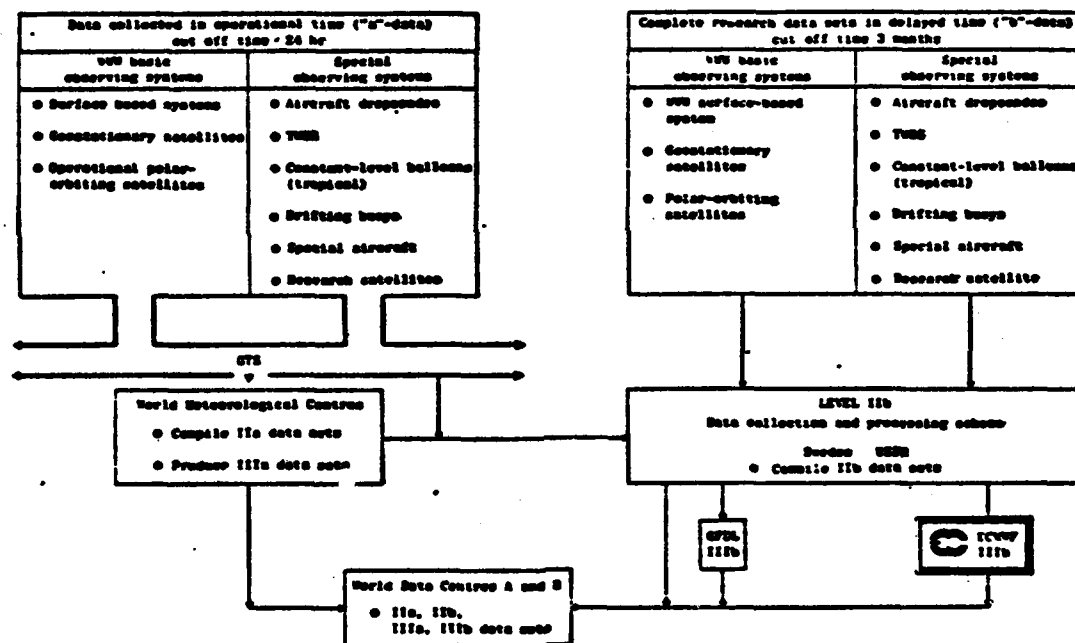


Figure 4. FGGE Data Management Plan (From Bengtsson, 1982)

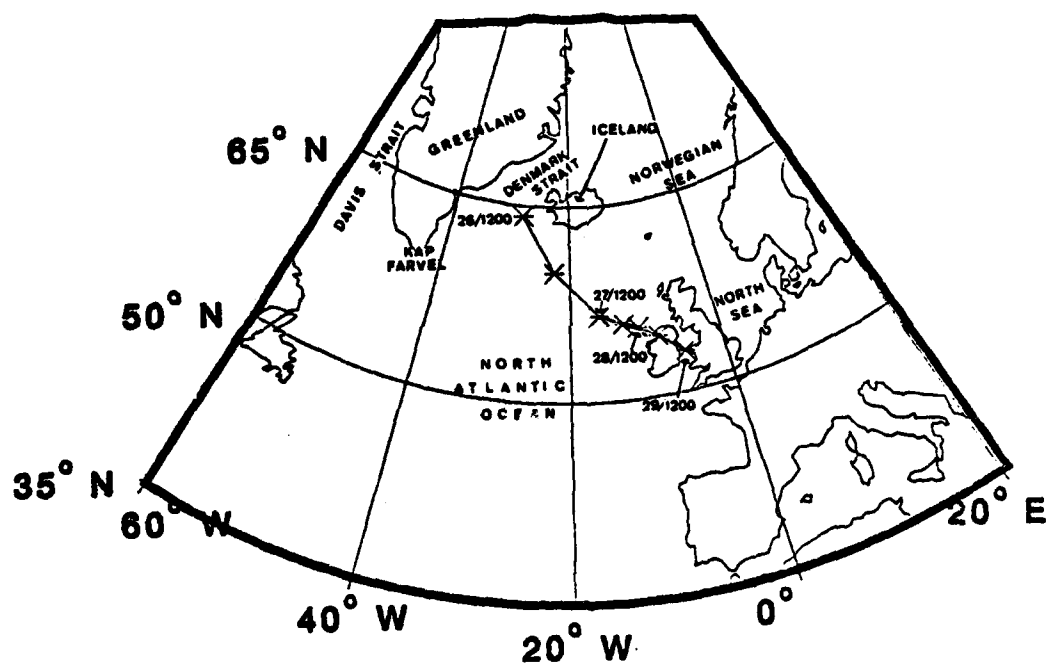


Figure 5. Storm Track. Positions in 12-h Increments.

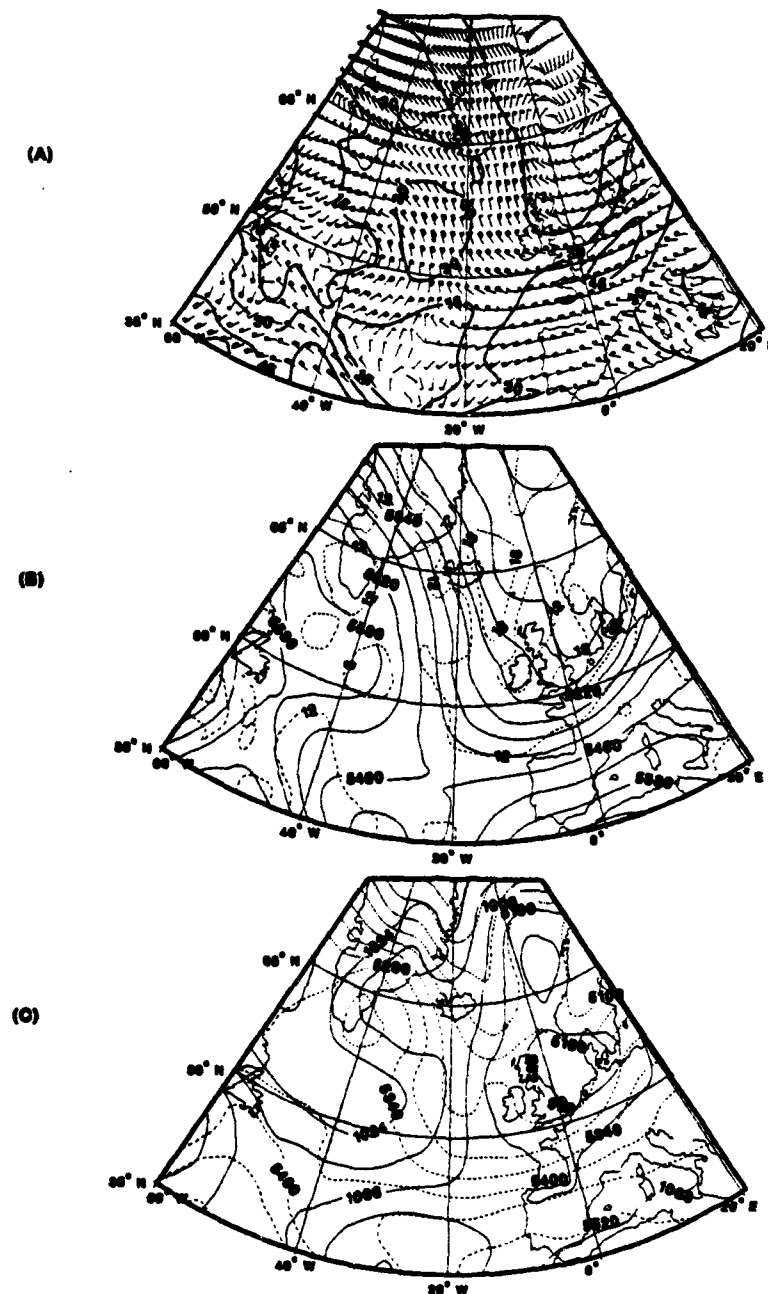


Figure 6. Synoptic Situation 12 GMT 26 January 1979 (A) 250 mb Winds (m/s). (B) 500 mb Heights (Solid) in gpm and Absolute Vorticity (Dashed) $\times 10^{-5}$ s. (C) SLP (Solid) and 1000-500 mb Thickness (Dashed).

AD-A136 844

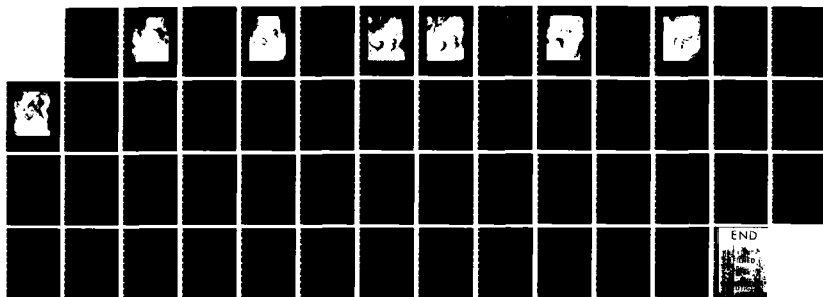
A QUASI-LAGRANGIAN DIAGNOSTICS INVESTIGATION OF RAPID
CYCLOGENESIS IN A POLAR AIR STREAM(U) NAVAL
POSTGRADUATE SCHOOL MONTEREY CA W A COOK SEP 83

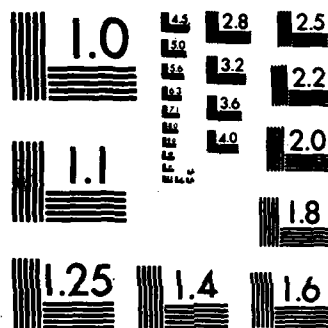
2/2

UNCLASSIFIED

F/G 4/2

NL





MICROCOPY RESOLUTION TEST CHART
NATIONAL BUREAU OF STANDARDS-1963-A



Figure 7. DMSP IR Imagery 2207 GMT 26 January 1979. (L)
Denotes Surface Position of Polar Low.

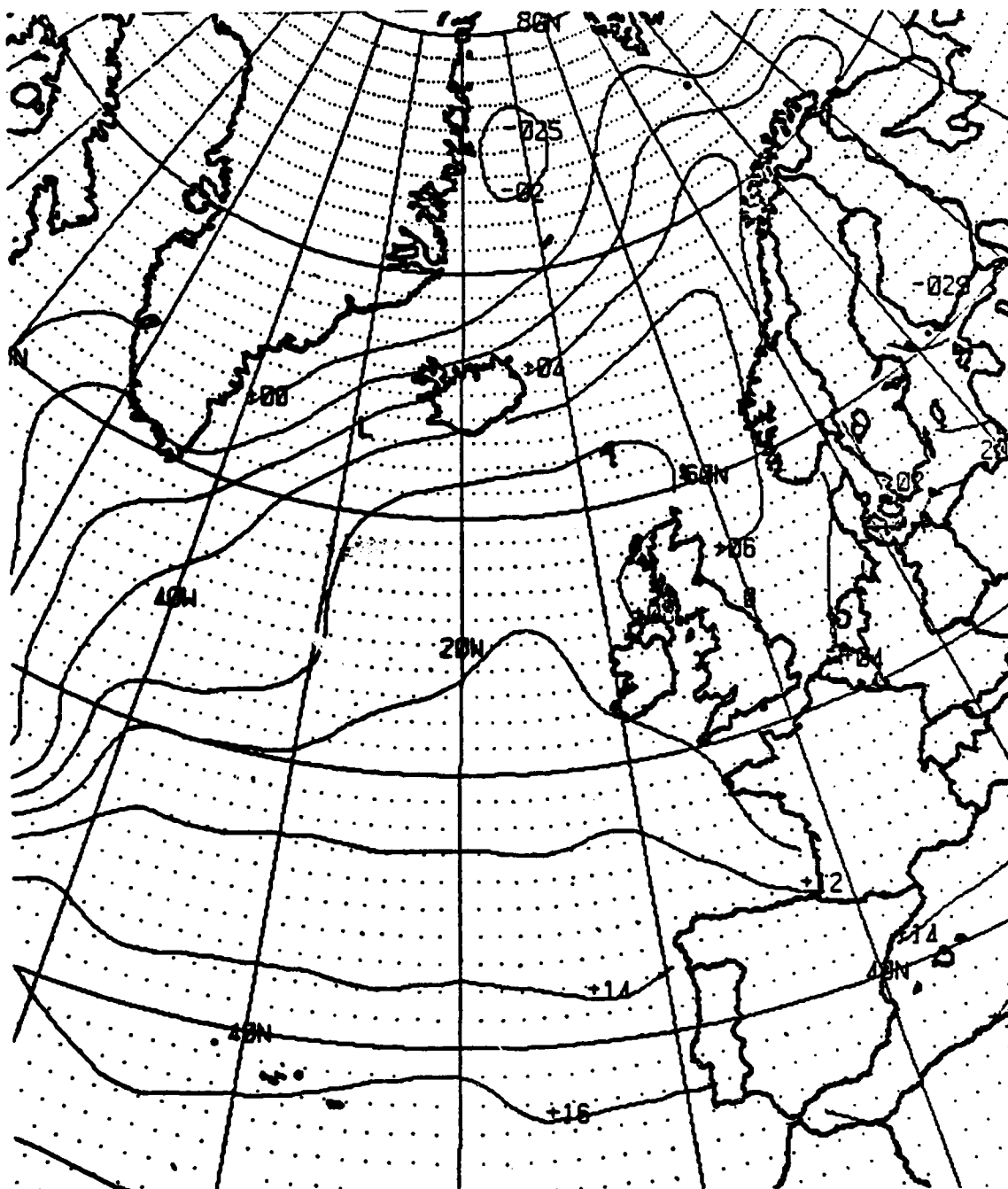


Figure 8. FNOC SST Analysis C 12 GMT 26 January 1979.
 (L) Denotes Surface Position of Polar Low at 12
 GMT 26 January 1979.



Figure 9. DMSP IR Imagery 0124 GMT 27 January 1979. (L)
Denotes Surface Position of Polar Low.

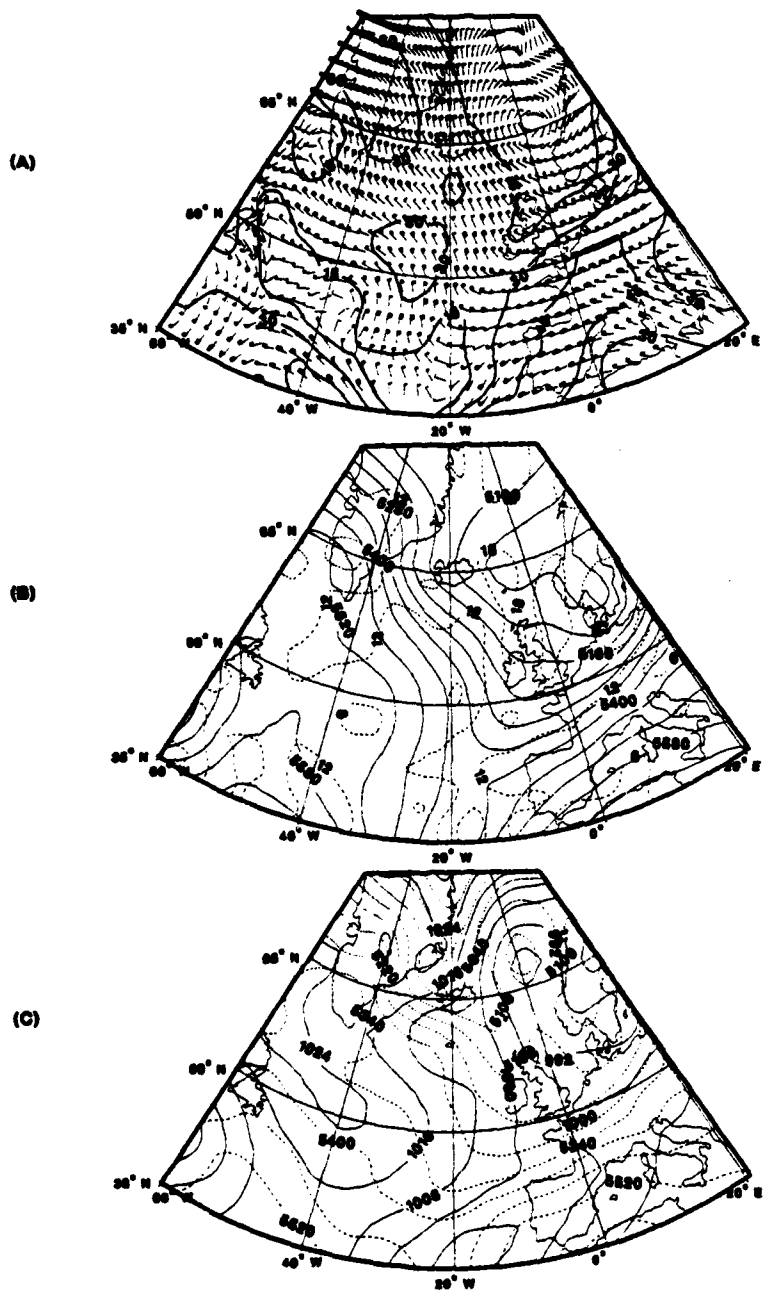


Figure 10. Similar to Figure 6 except for 00 GMT 27 January 1979



Figure 11. DMSP IR Imagery 0544 GMT 27 January 1979. (L)
Denotes Surface Position of Polar Low.



Figure 12. DMSP IR Imagery 1043 GMT 27 January 1979. (L)
Denotes Surface Position of Polar Low.

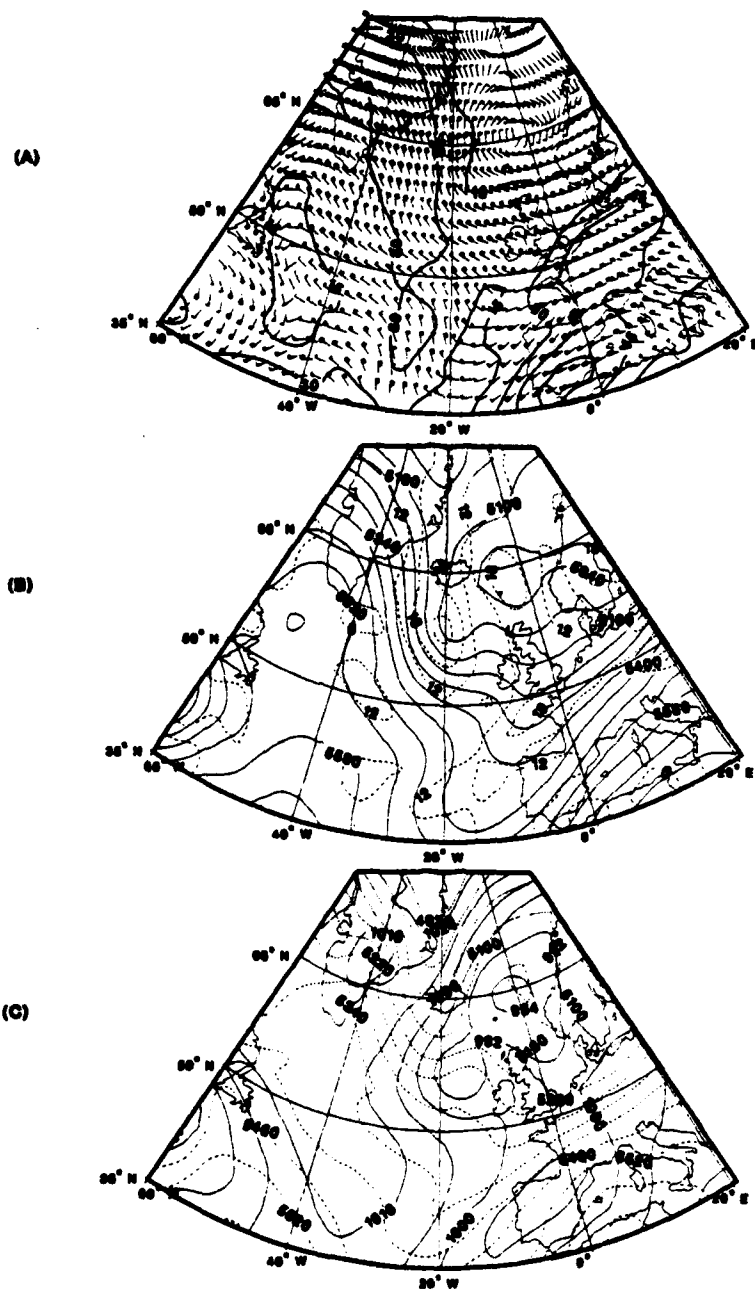


Figure 13. Similar to Figure 6 except for 12 GMT 27 January 1979



Figure 14. DMSP IR Imagery 2006 GMT 27 January 1979. (L)
Denotes Surface Position of Polar Low.

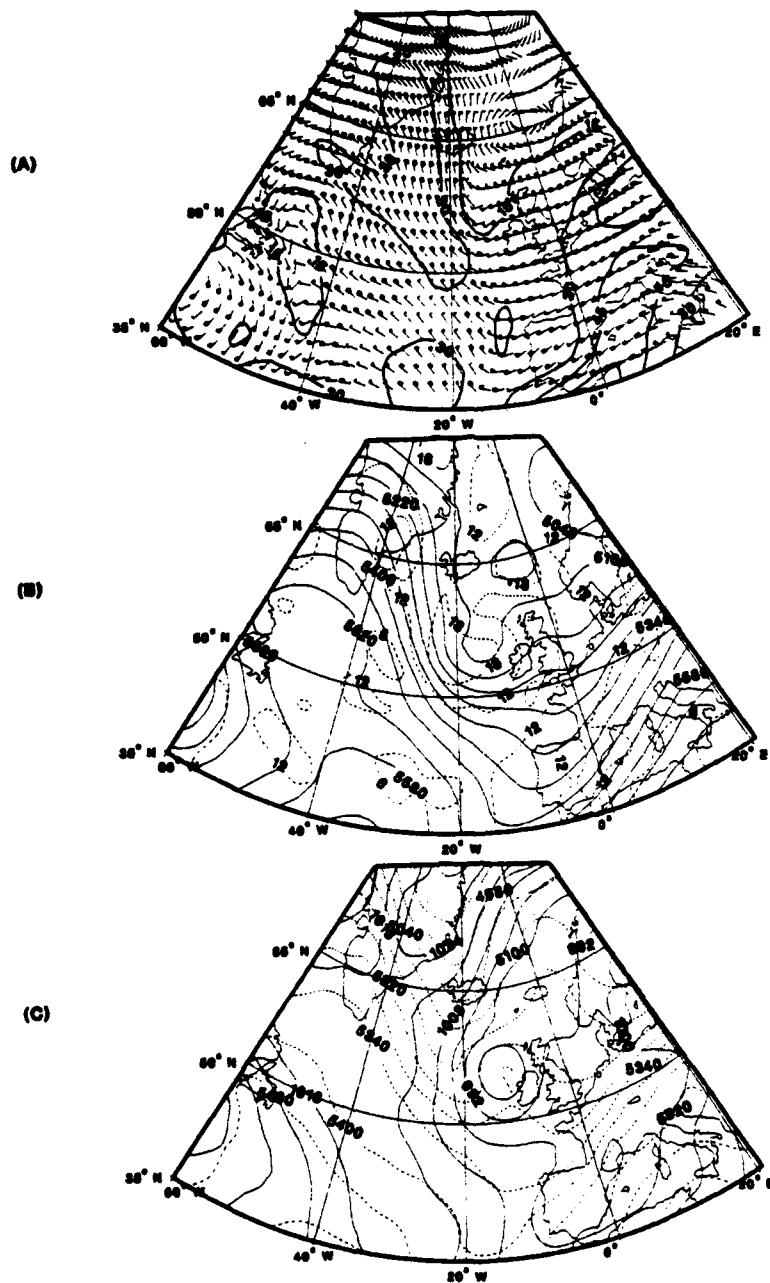


Figure 15. Similar to Figure 6 except for 00 GMT 28 January 1979



Figure 16. DMSP IR Imagery 1025 GMT 28 January 1979. (L)
Denotes Surface Position of Polar Low.

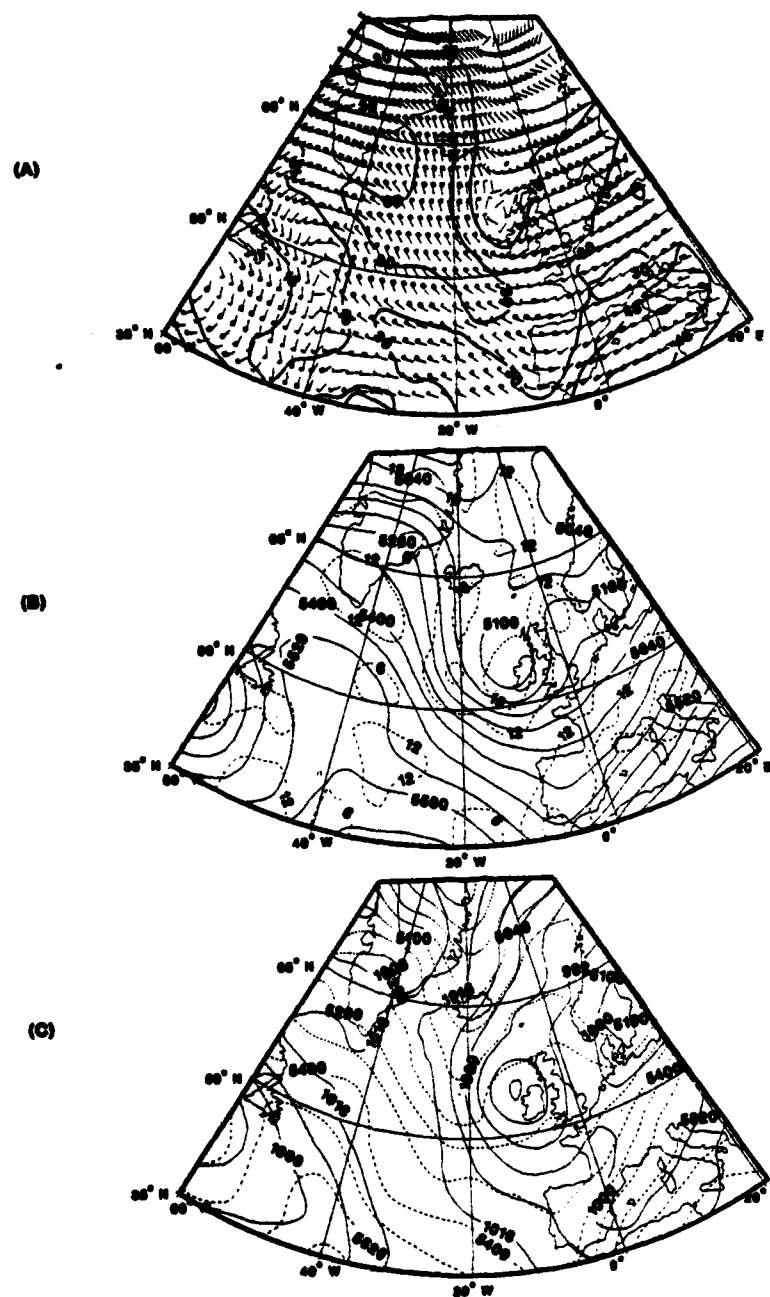


Figure 17. Similar to Figure 6 except for 12 GMT 28 January 1979

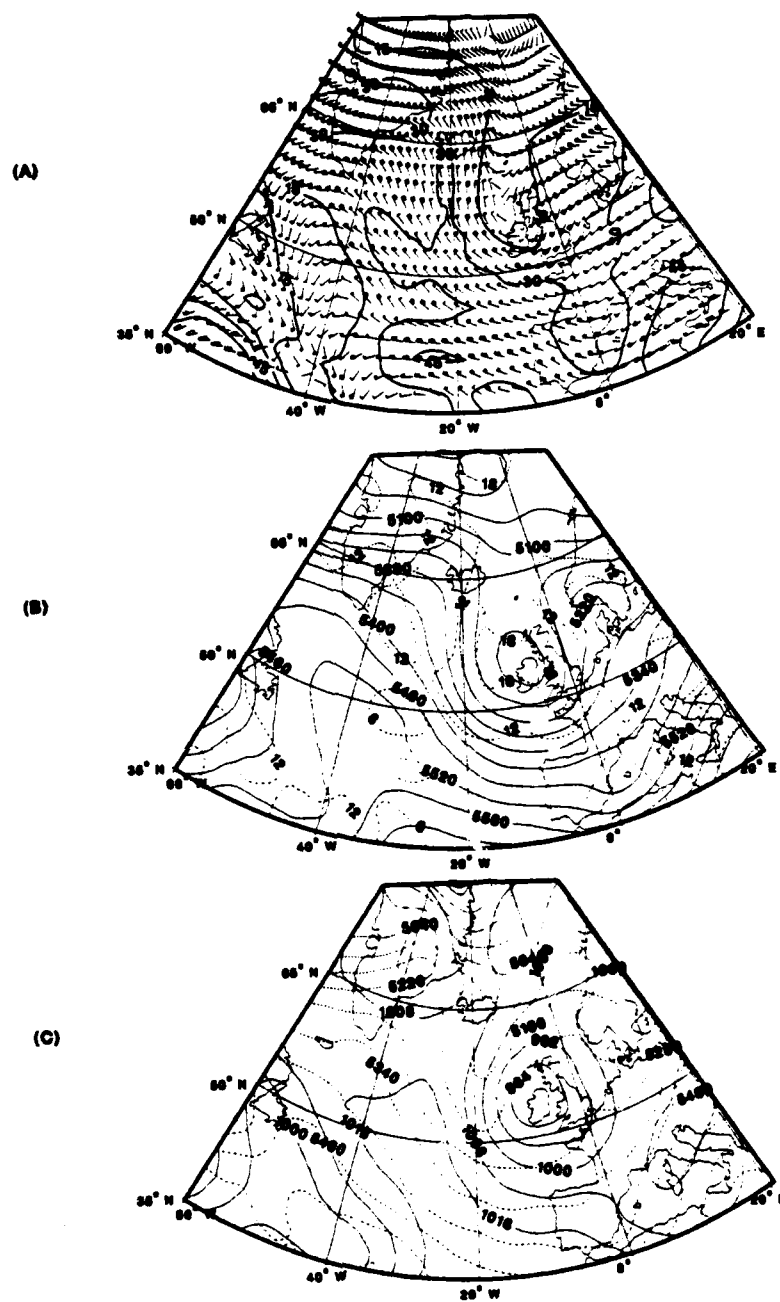


Figure 18. Similar to Figure 6 except for 00 GMT 29 January 1979



Figure 19. DMSP IR Imagery 0048 GMT 29 January 1979

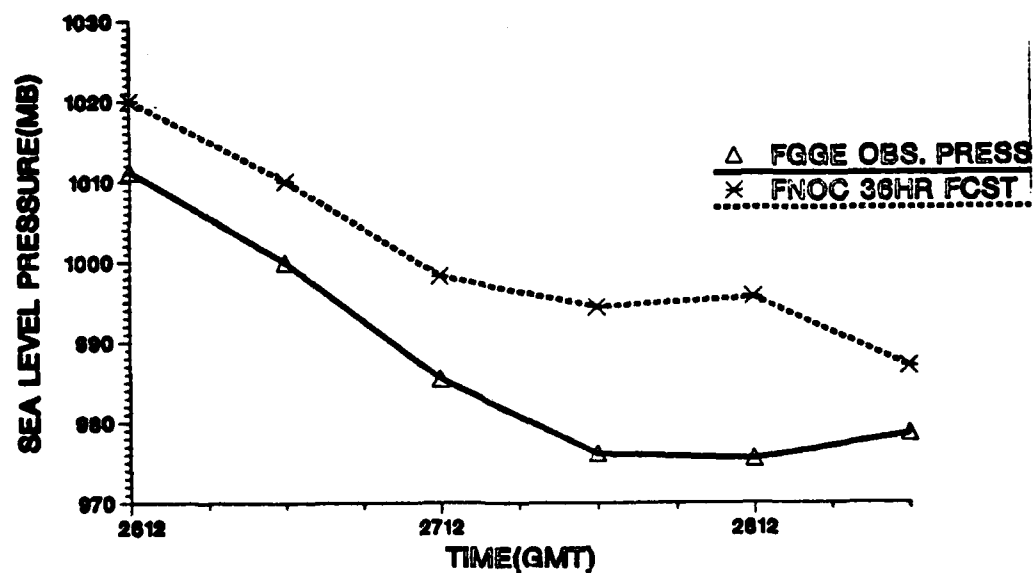


Figure 21. FNOC 36-h Model Forecast Comparison. SLP Forecasts in 12-h Increments. 2612 Refers to 12 GMT 26 January.

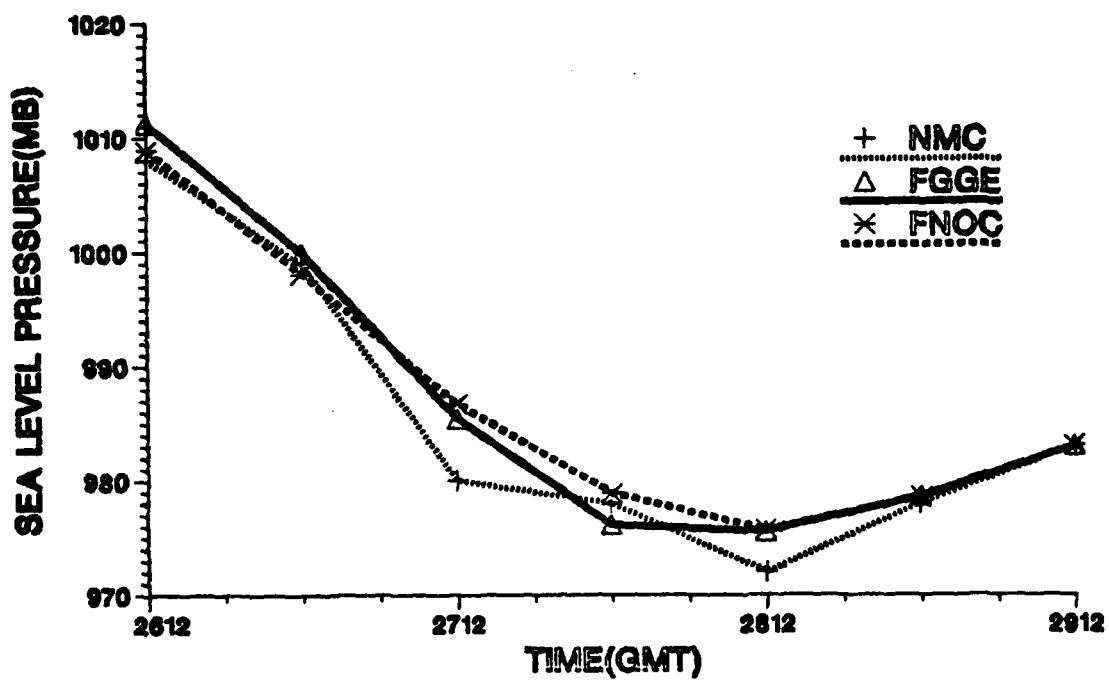


Figure 22. NMC, FGGE, FNOC Central Pressure Comparison. SLP Analyses in 12-h Increments.

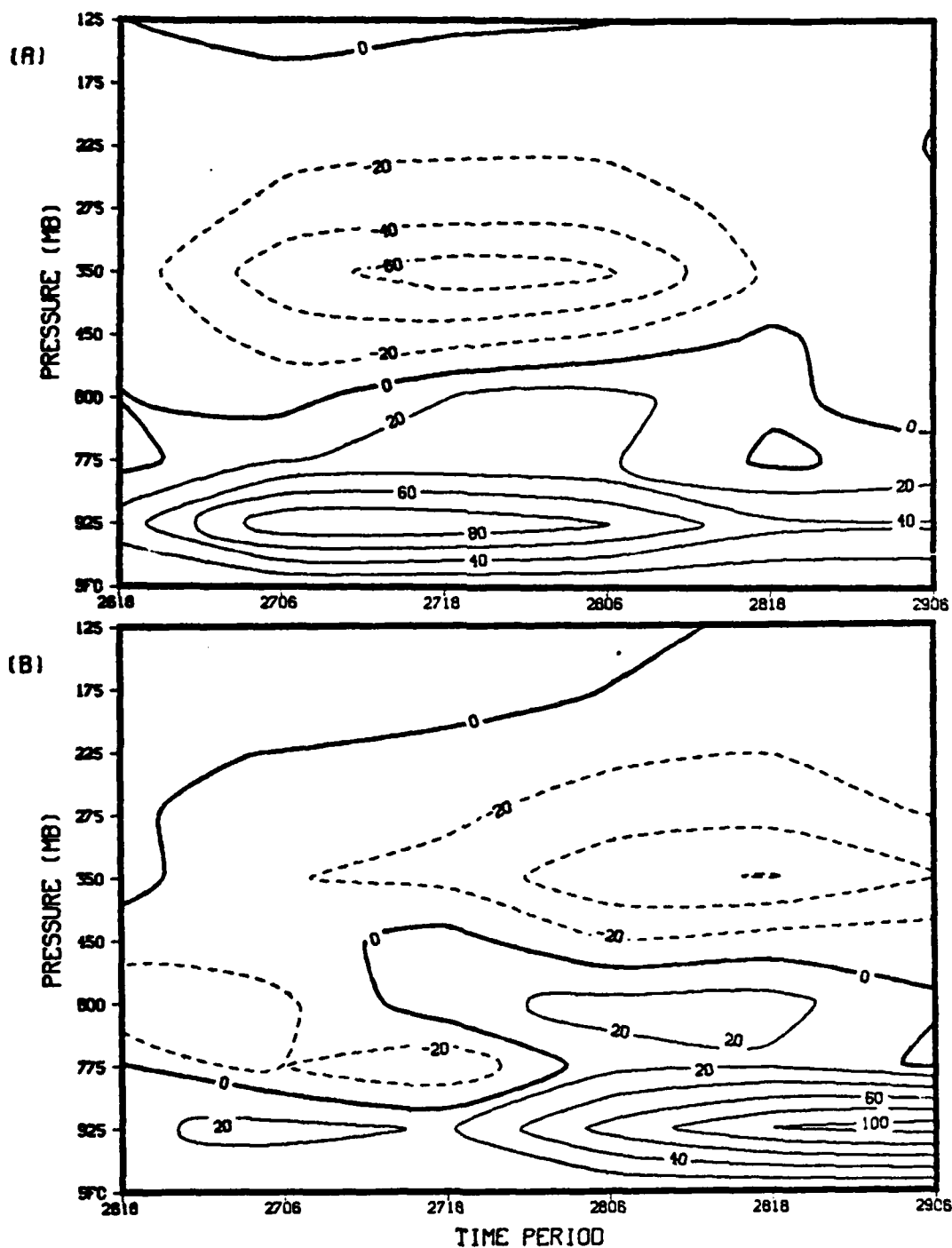


Figure 23. Horizontal Mass Flux (A) Radius 4 (B) Radius 8. Positive/Negative Values Denote Mass Flux Into/Out of the Budget Volume. Contours are 20 X 10^{19} gm/sec-100 mb.

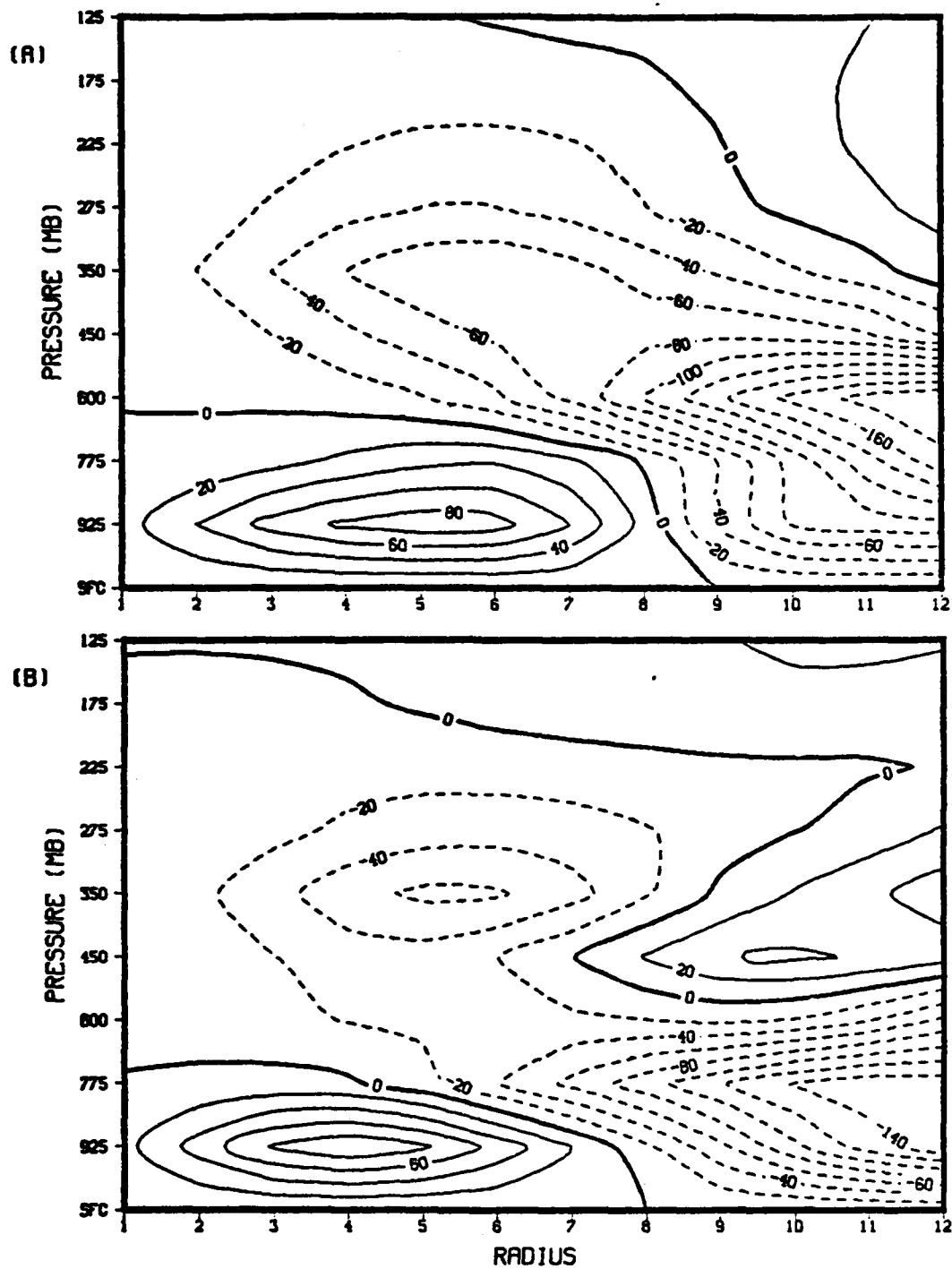


Figure 24. Radial Cross-Sections at (A) 00 GMT 27 January, (B) 12 GMT 27 January. Units same as Figure 23.

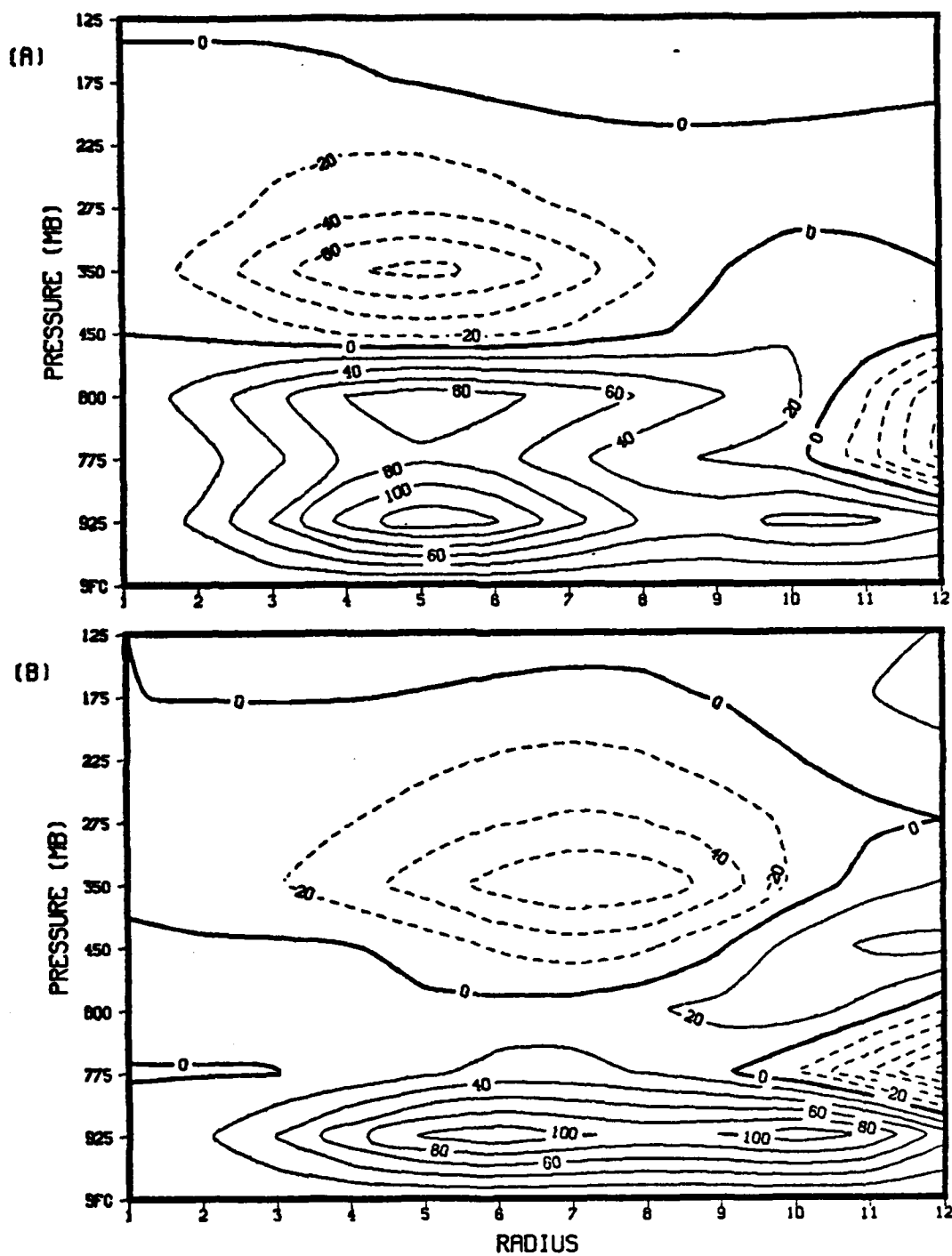


Figure 25. Radial Cross-Sections (A) 00 GMT 28 January, (B) 12 GMT 28 January.

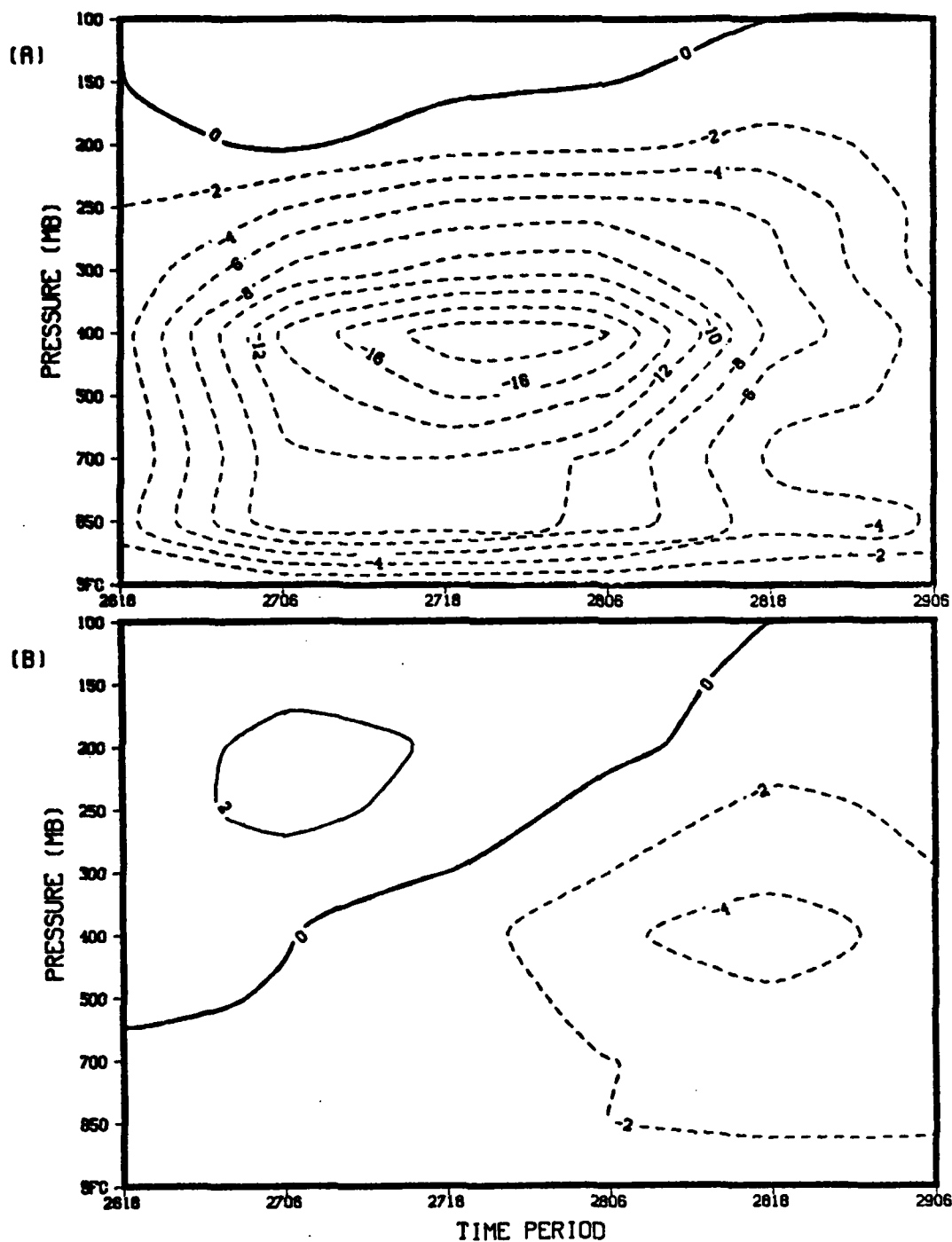


Figure 26. QLD Vertical Velocities (Omegas) at (A) Radius 4, (B) Radius 8. Units mb/1000-sec.

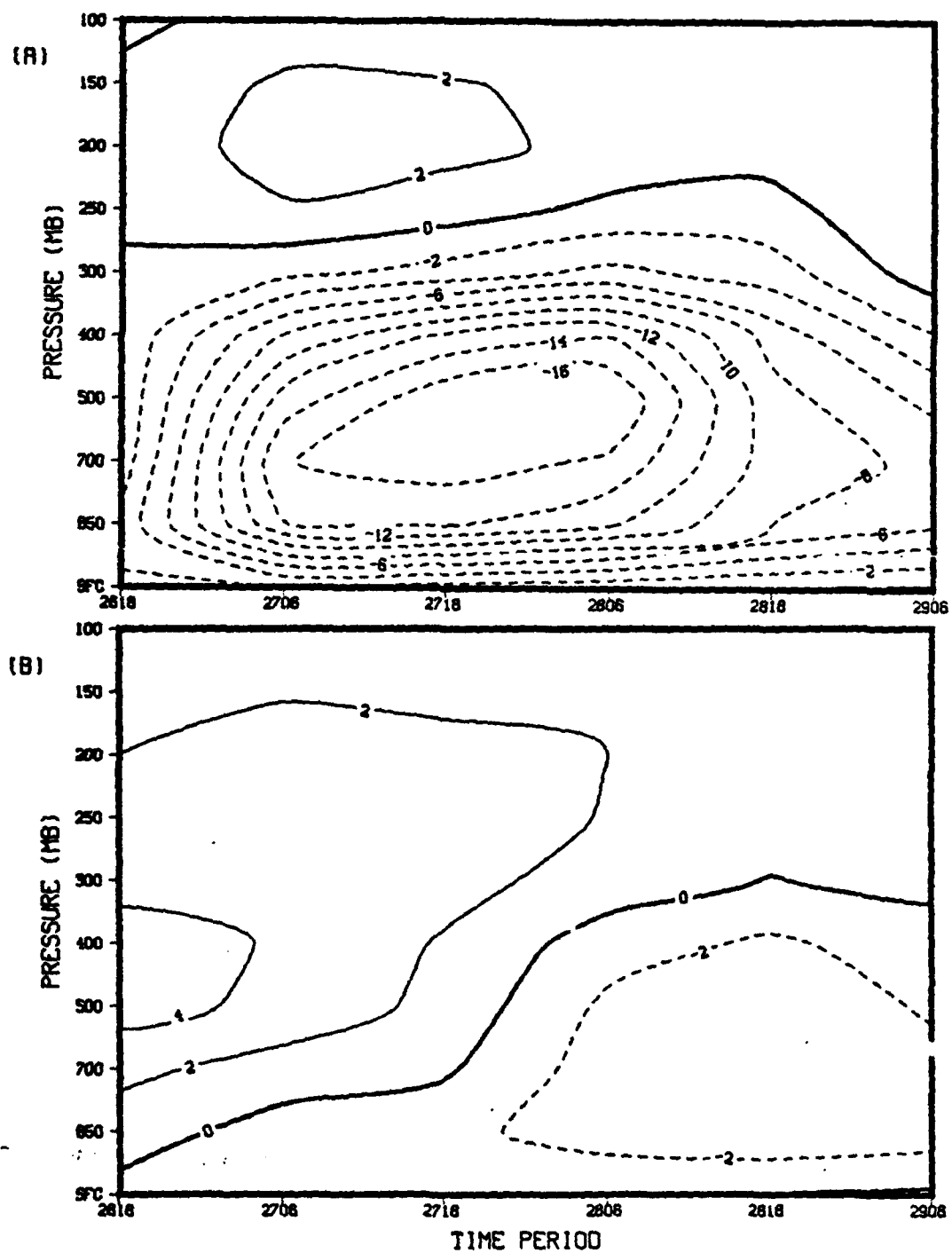


Figure 27. Similar to Figure 26 except for Kinematic Omegas

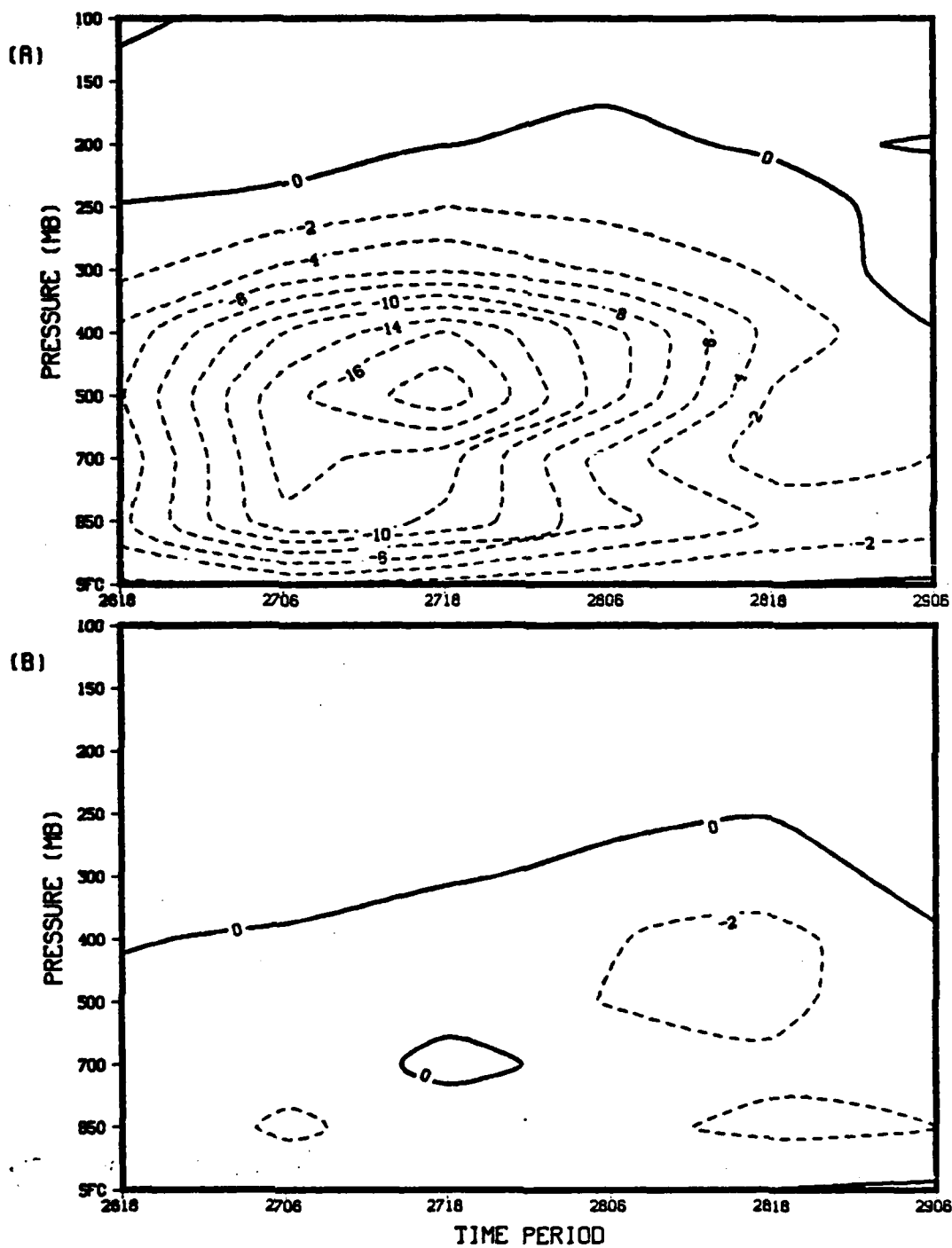


Figure 28. Similar to Figure 26 except for PGGE Omegas

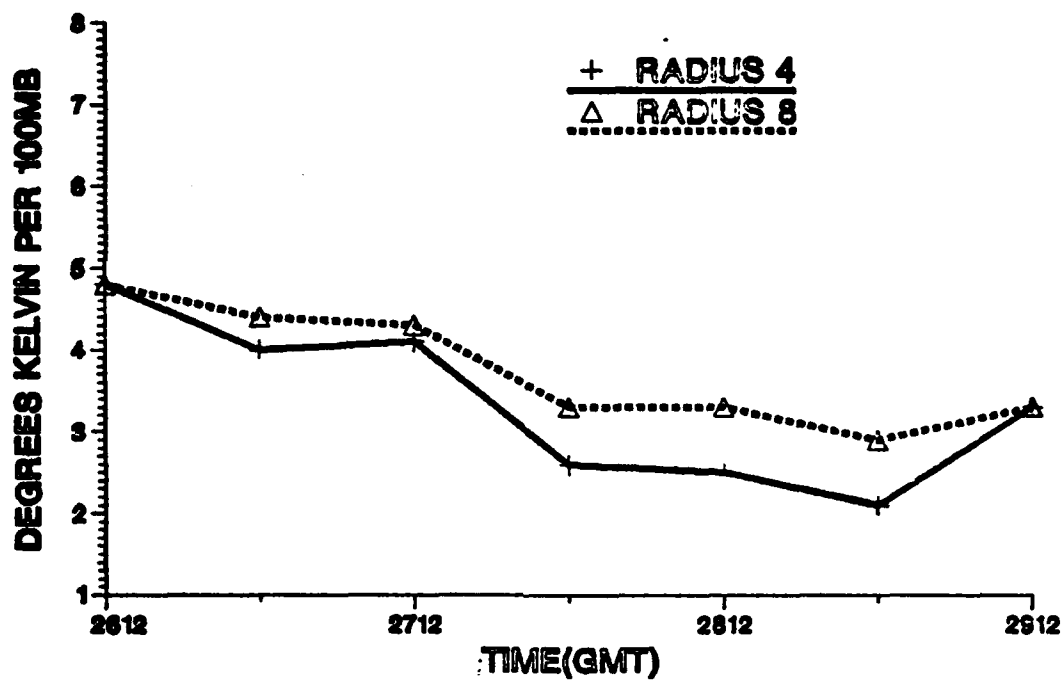


Figure 29. Static Stability Index. Values °K per 100 mb.
Time 2612 refers to 12 GMT 26 January 1979.

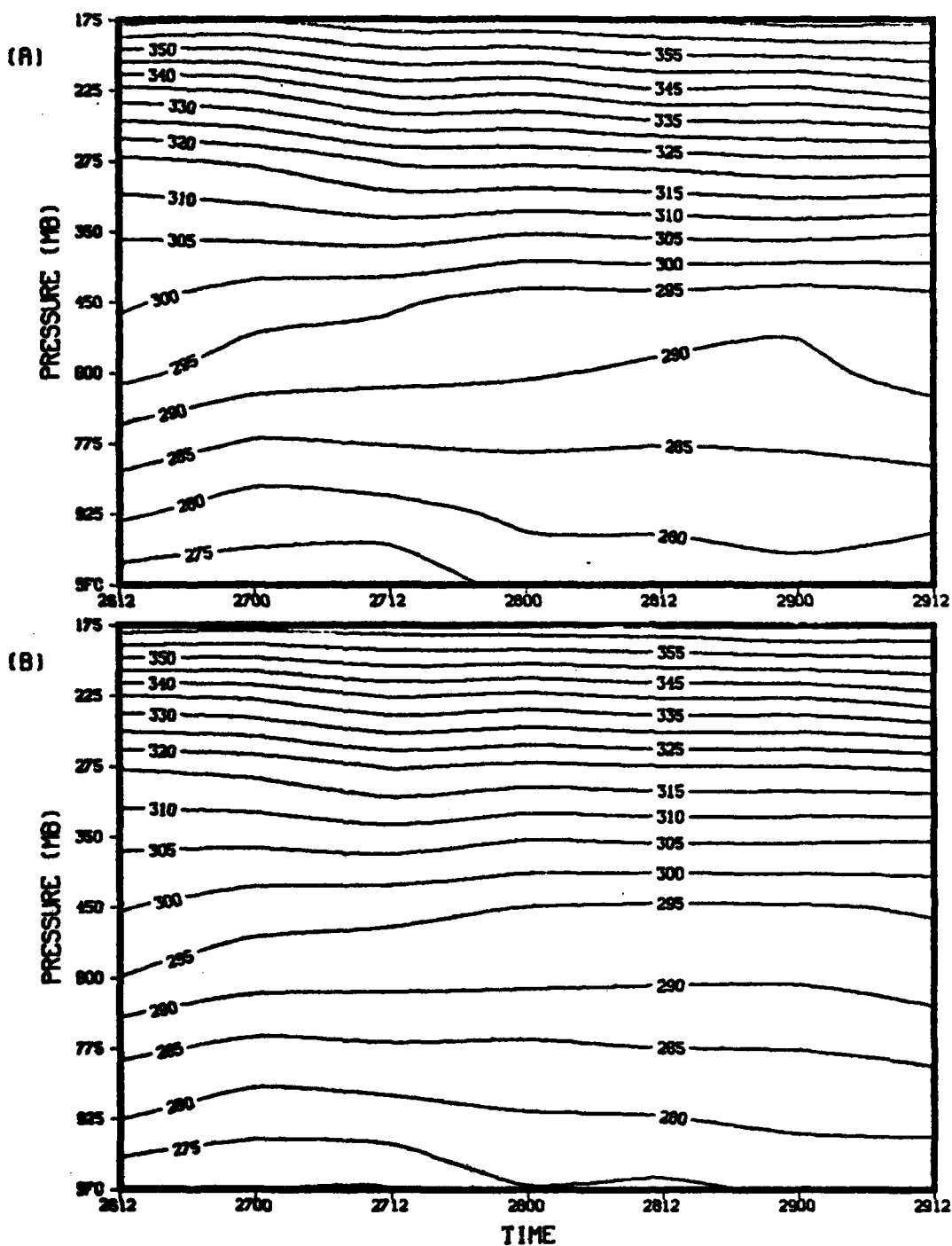


Figure 30. Area-Averaged Potential Temperatures
OK at (A) Radius 4, (B) Radius 8.

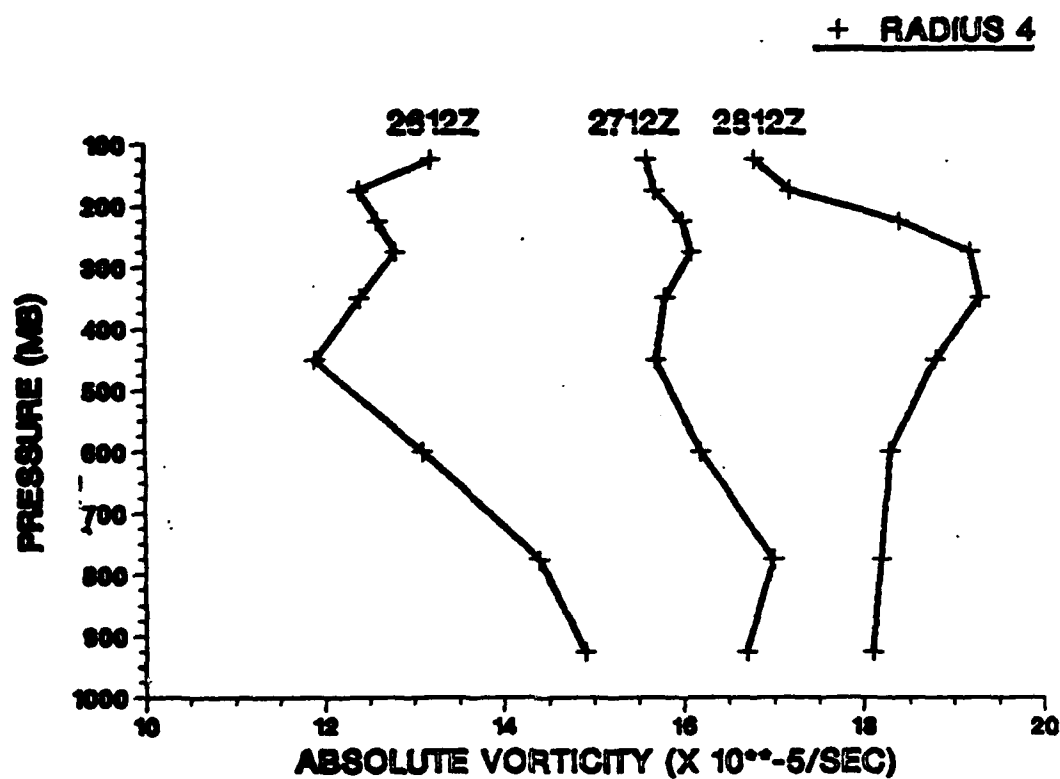


Figure 31. Absolute Vorticity Vertical Profiles for Radius 4. 2612 refers to 12 GMT 26 January.

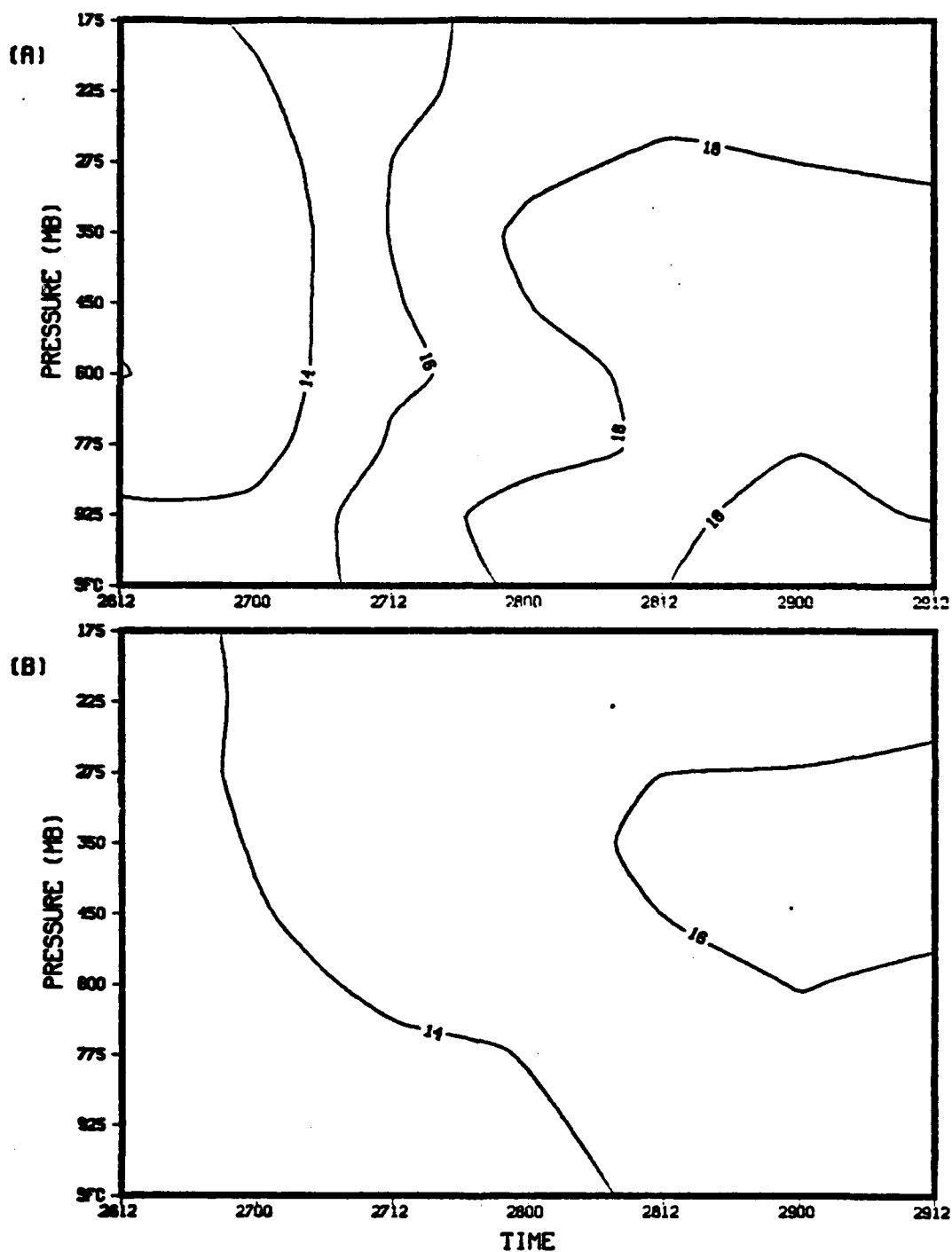


Figure 32. Absolute Vorticity Time Sections for (A) Radius 4 and (B) Radius 8. Units are $10 \times 10^{-5} s^{-1}$.

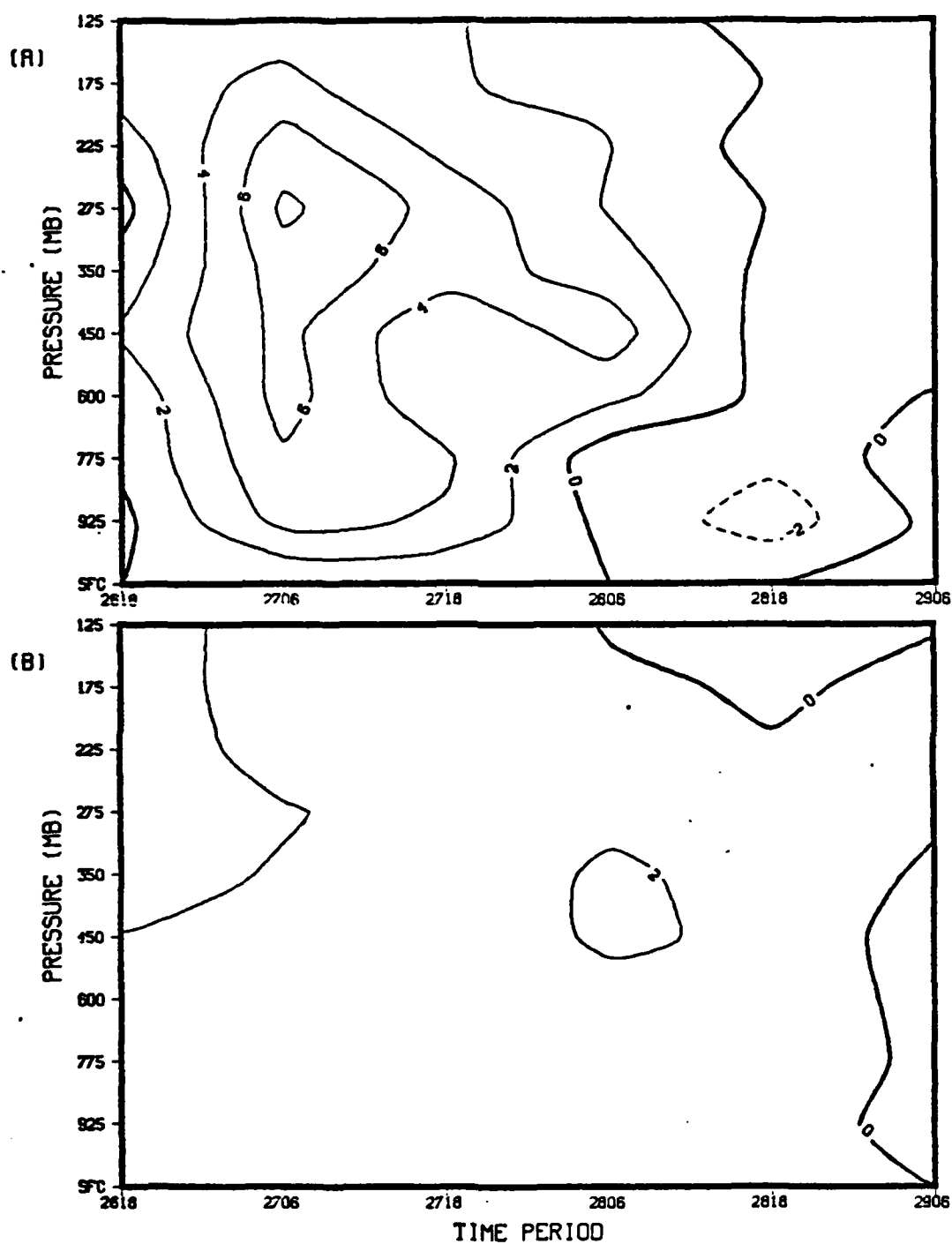


Figure 33. Absolute Vorticity Vertical Time Tendency for (A) Radius 4 and (B) Radius 8. Solid/dashed Contours Indicate Vorticity Increases/Decreases. Units are $10 \times 10^{-10} \text{ s}^{-2}$.

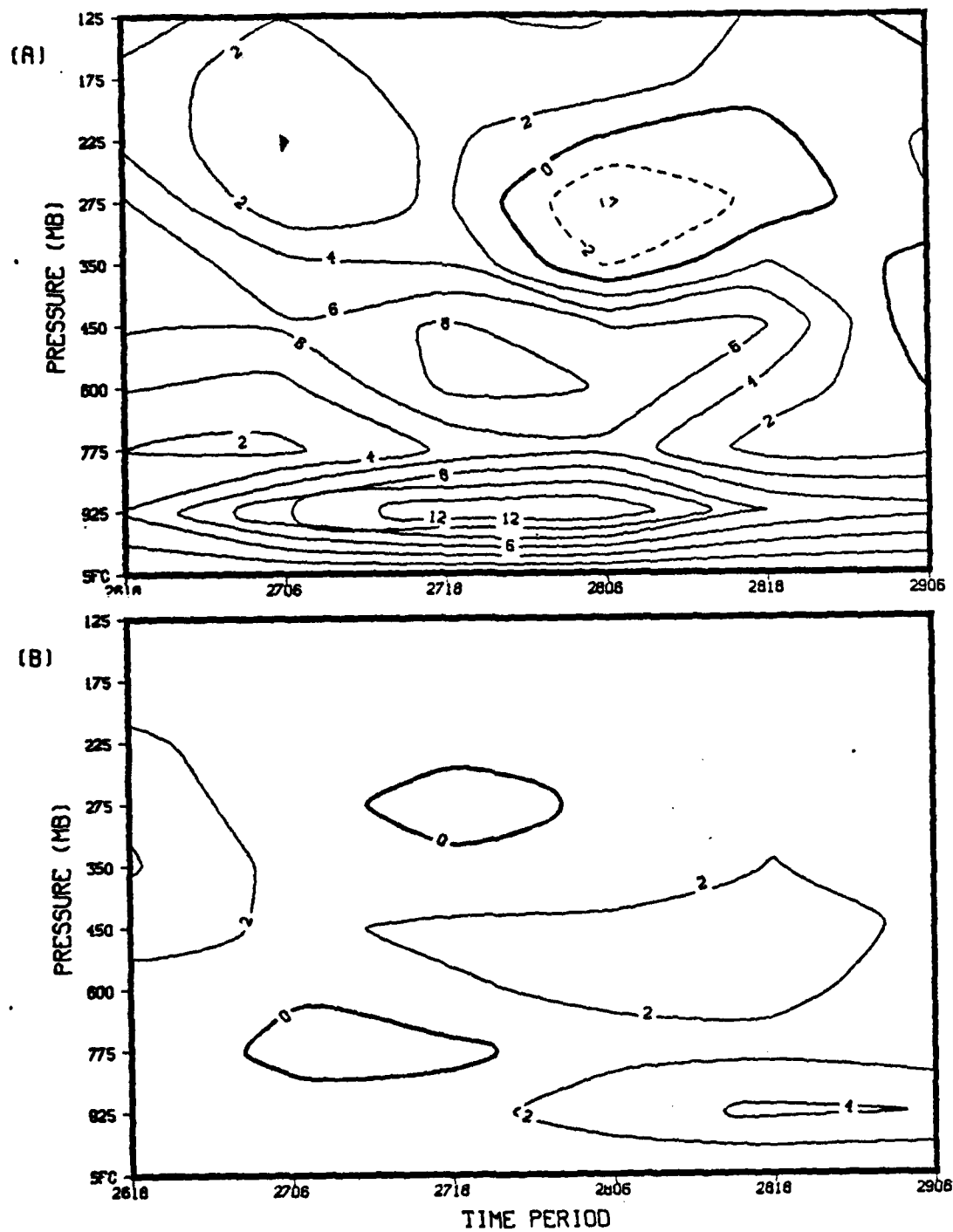


Figure 34. Similar to Figure 33 except for Lateral Vorticity Transport

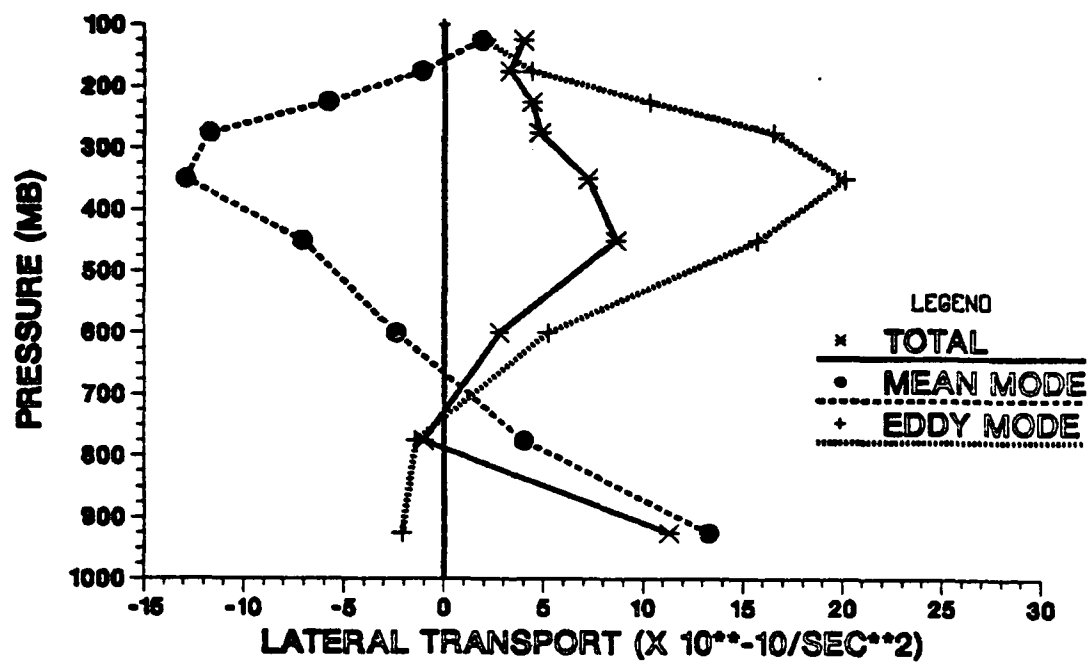


Figure 35. Total, Mean and Eddy Mode Lateral Transports During a Period of Rapid Intensification. Units same as in Figure 33.

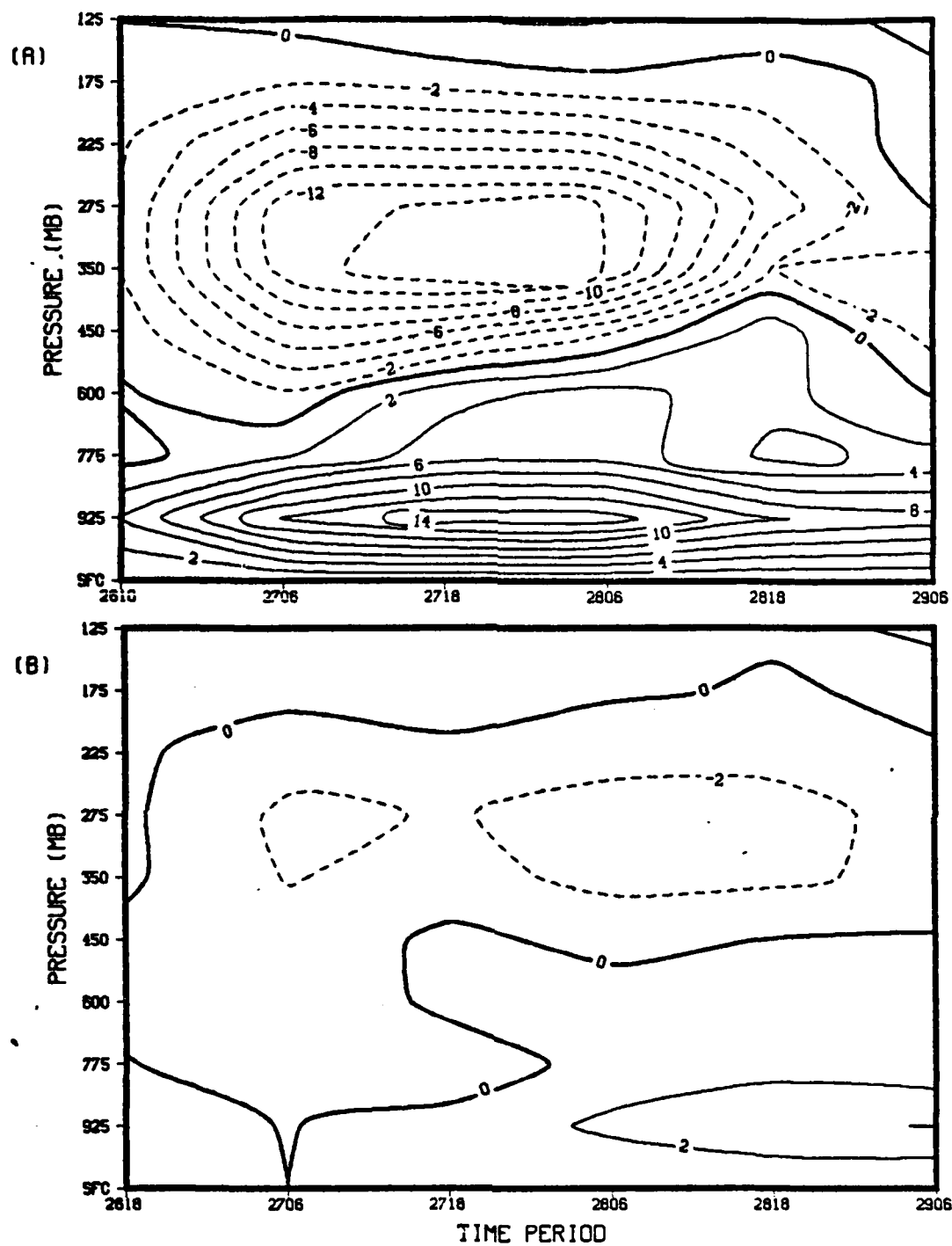


Figure 36. Similar to Figure 33 except for Mean Mode Transport

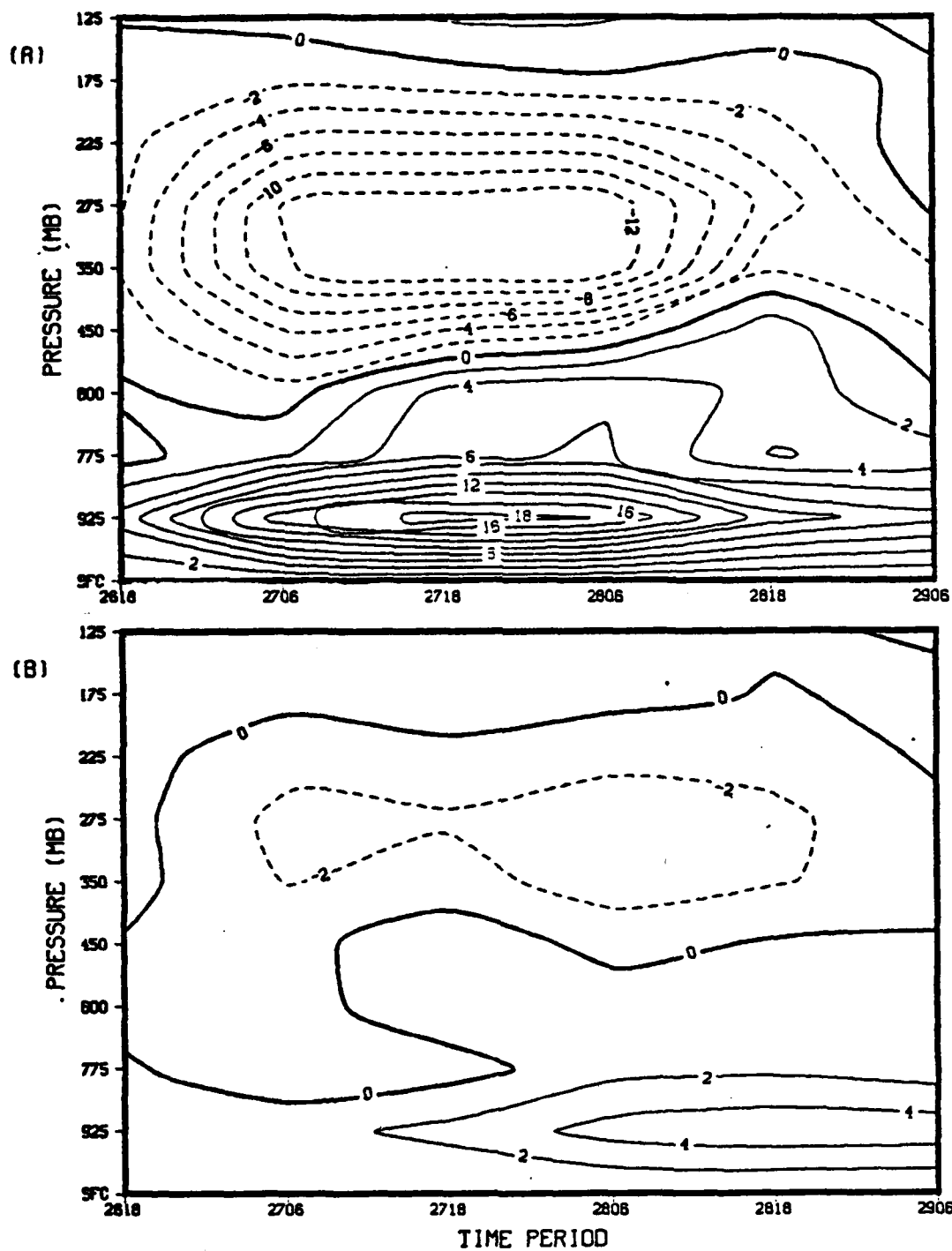


Figure 37. Similar to Figure 33 except for Lateral Divergence Component of the Lateral Vorticity Transport.

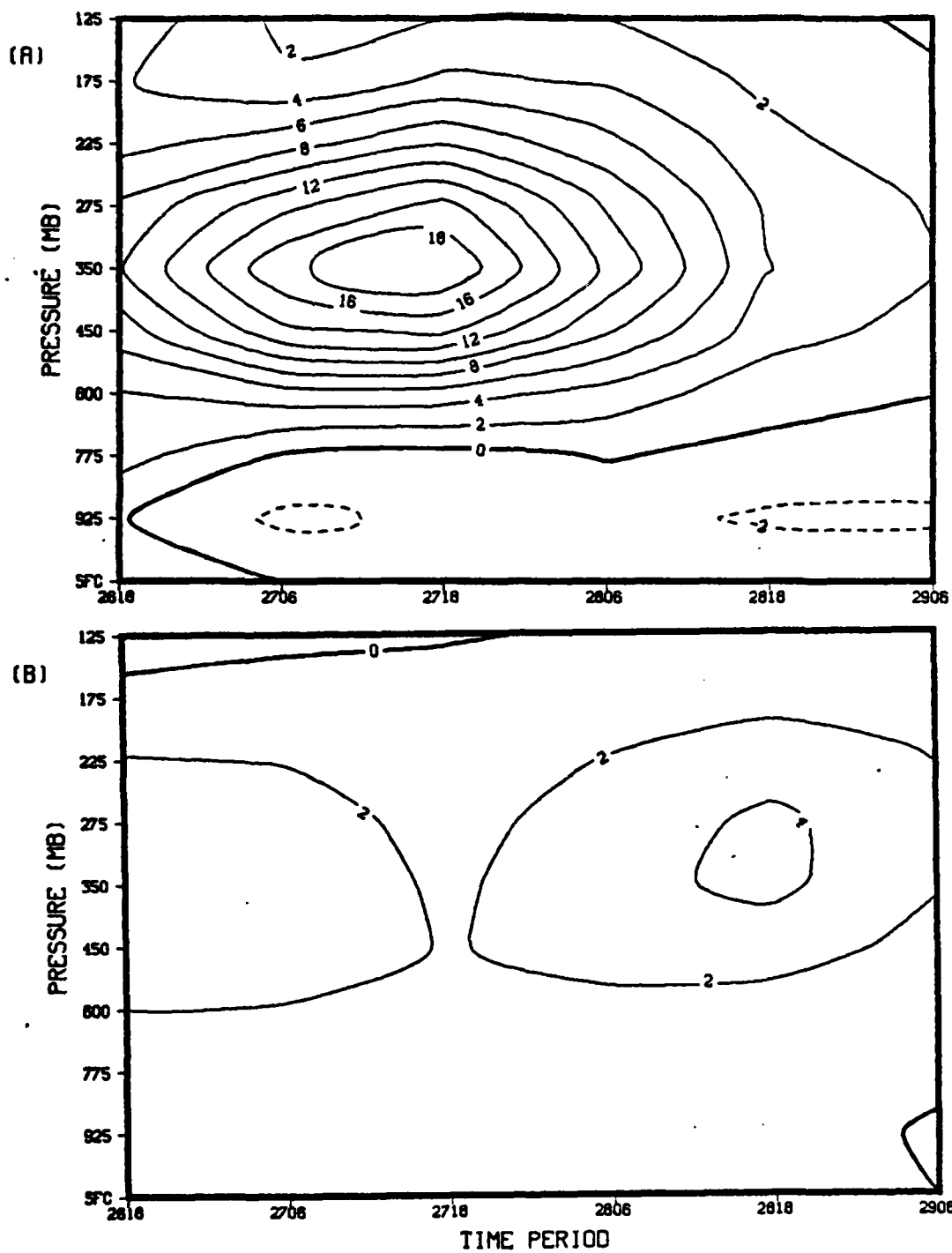


Figure 38. Similar to Figure 33 except for Eddy Mode Transport

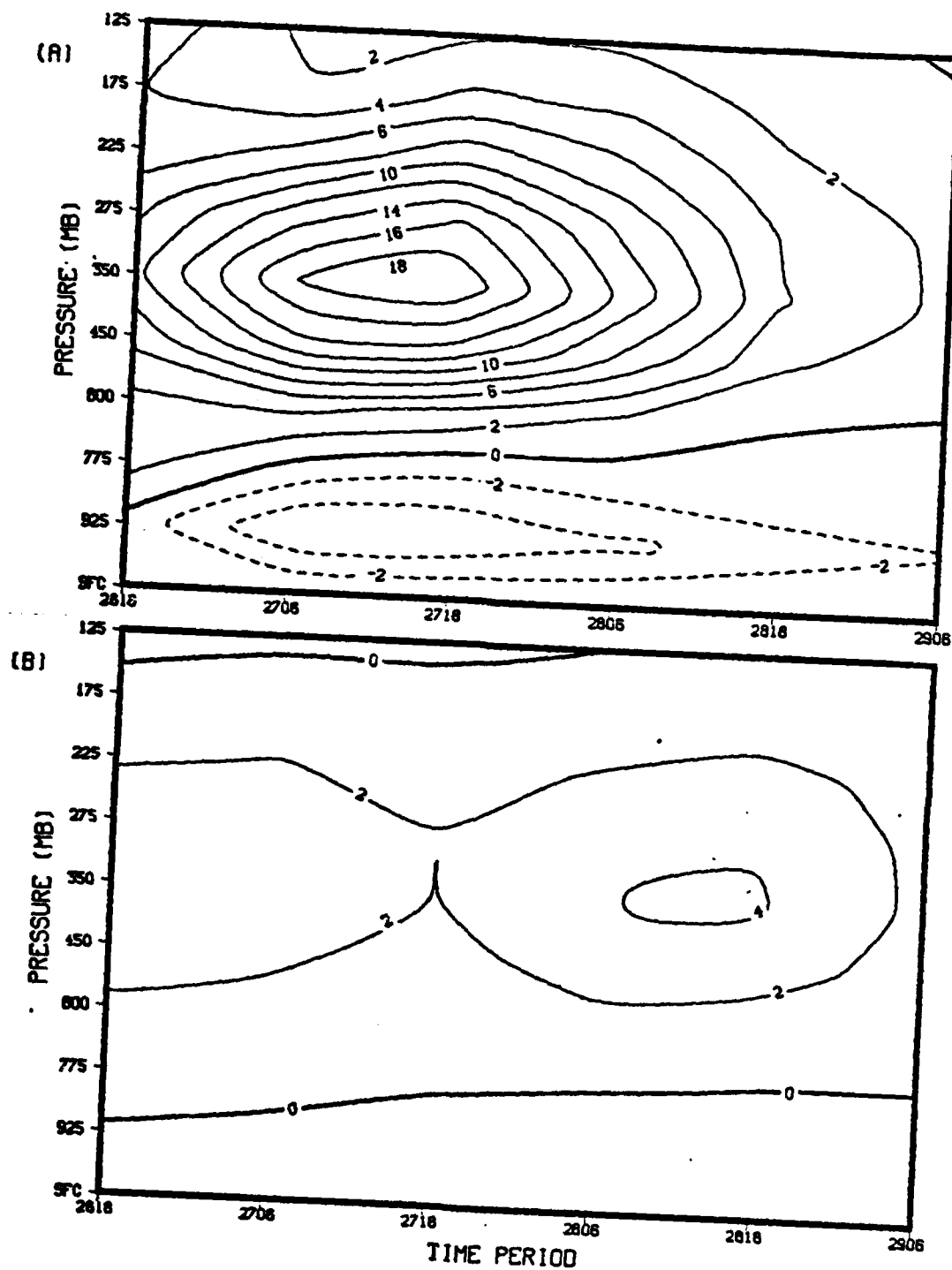


Figure 39. Similar to Figure 33 except for Lateral Advection Component of the Lateral Vorticity Transport.

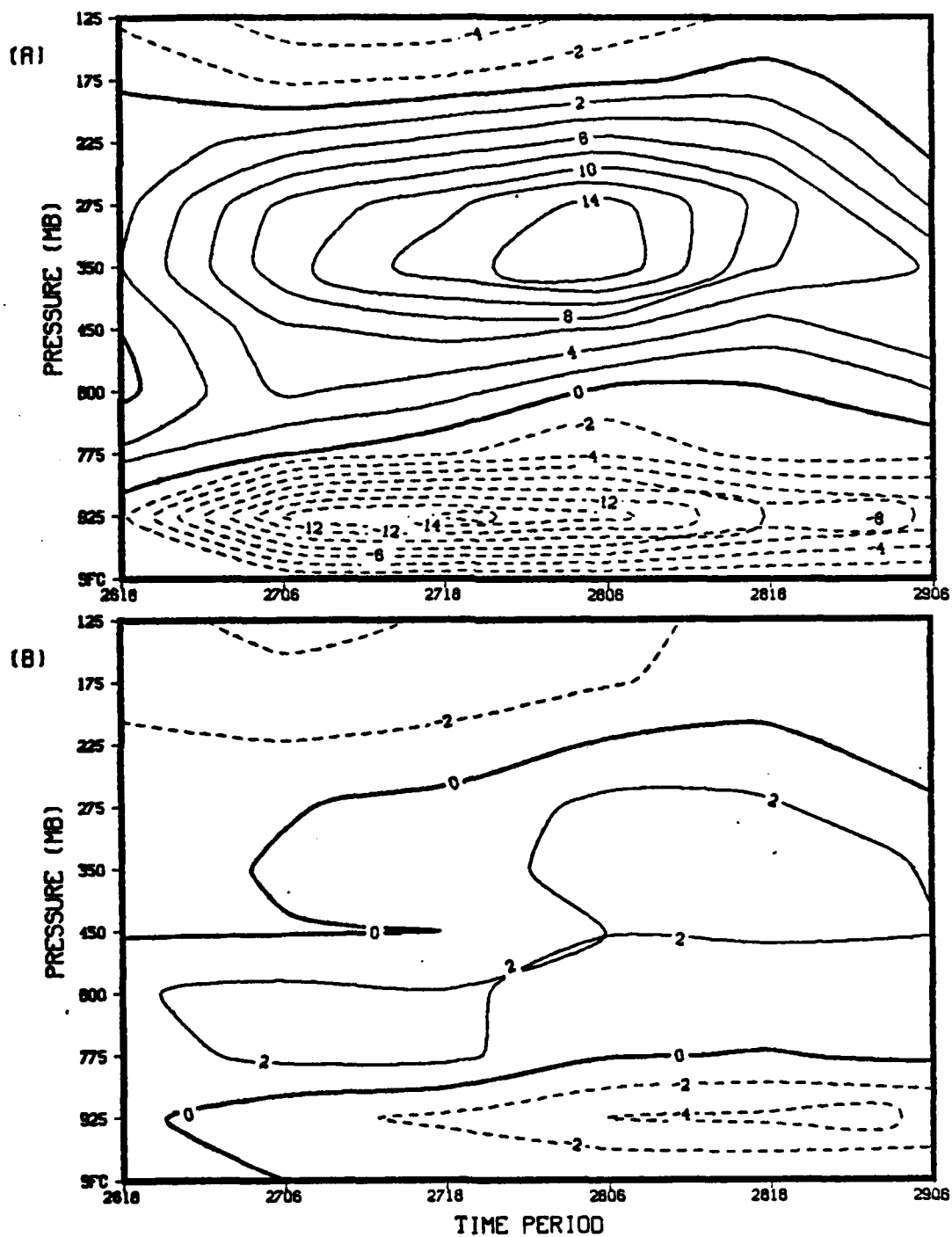


Figure 40. Similar to Figure 33 for Divergence of Vertical Transport

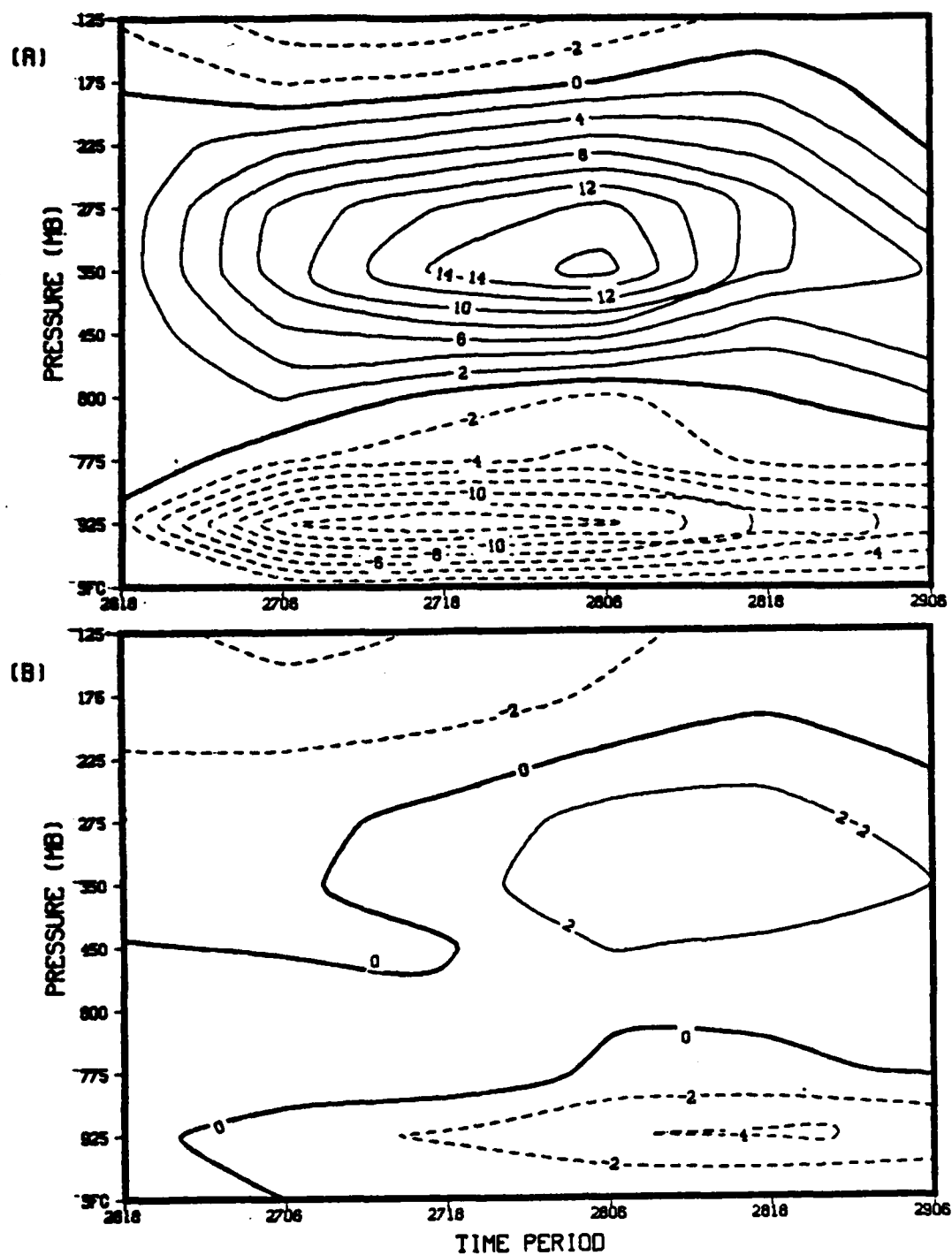


Figure 41. Similar to Figure 33 except for Vertical Divergence Component of the Divergence of the Vertical Transport.

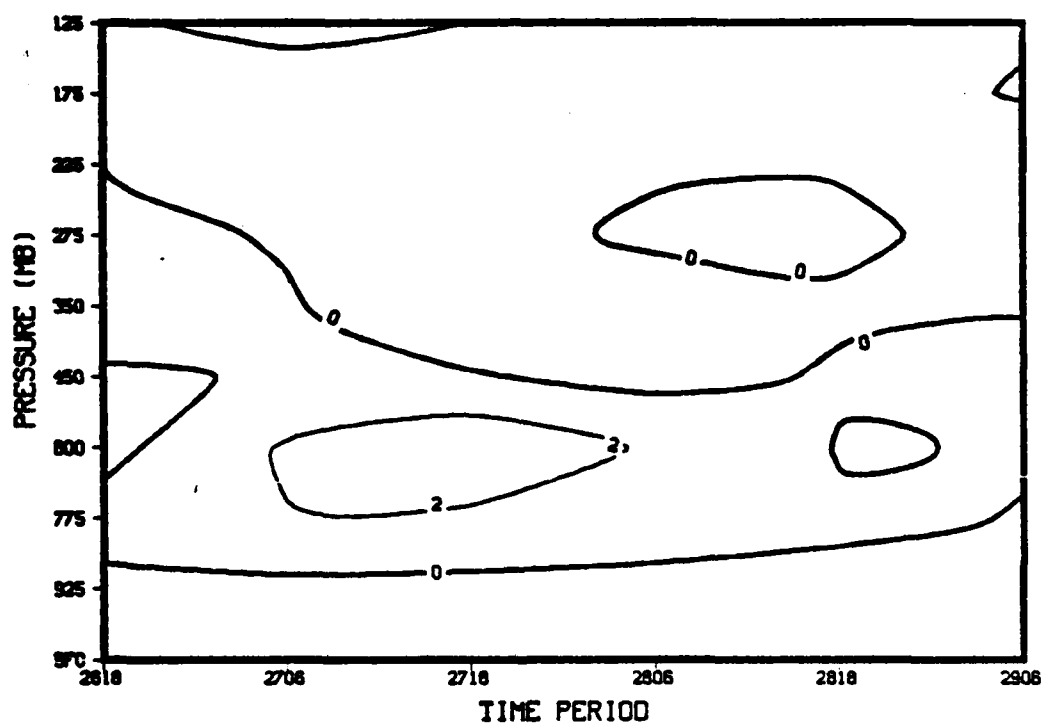


Figure 42. Similar to Figure 33 except for Vertical Advection Component of the Divergence of the Vertical Transport for Radius 4 Only.

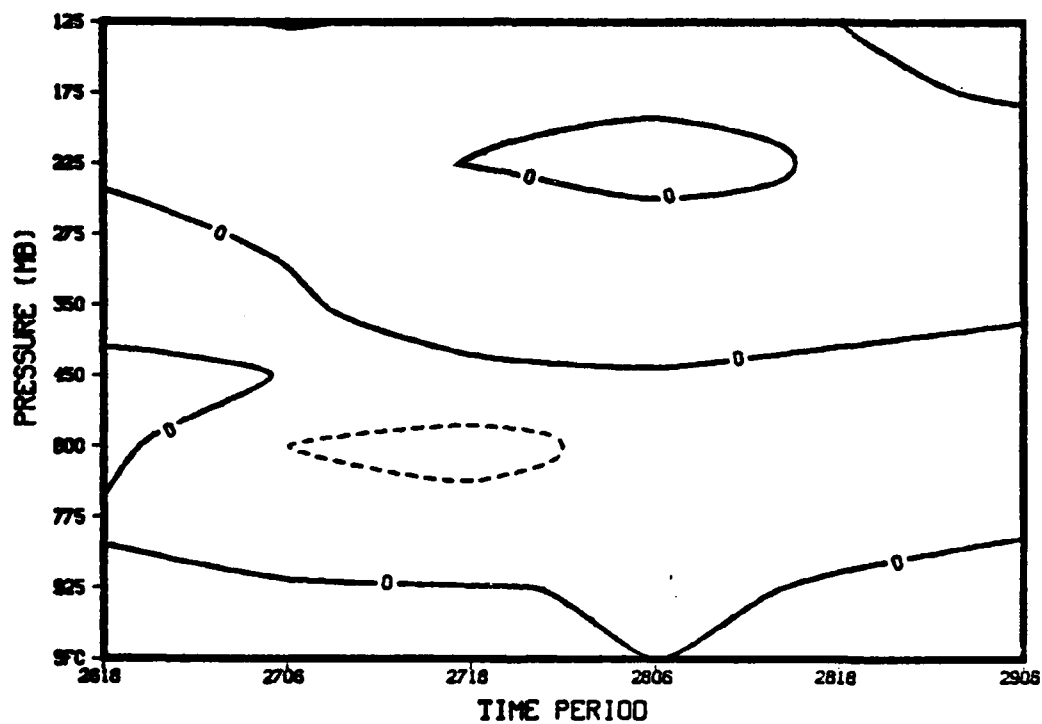


Figure 43. Similar to Figure 33 except for Tilting Term for Radius 4 Only.

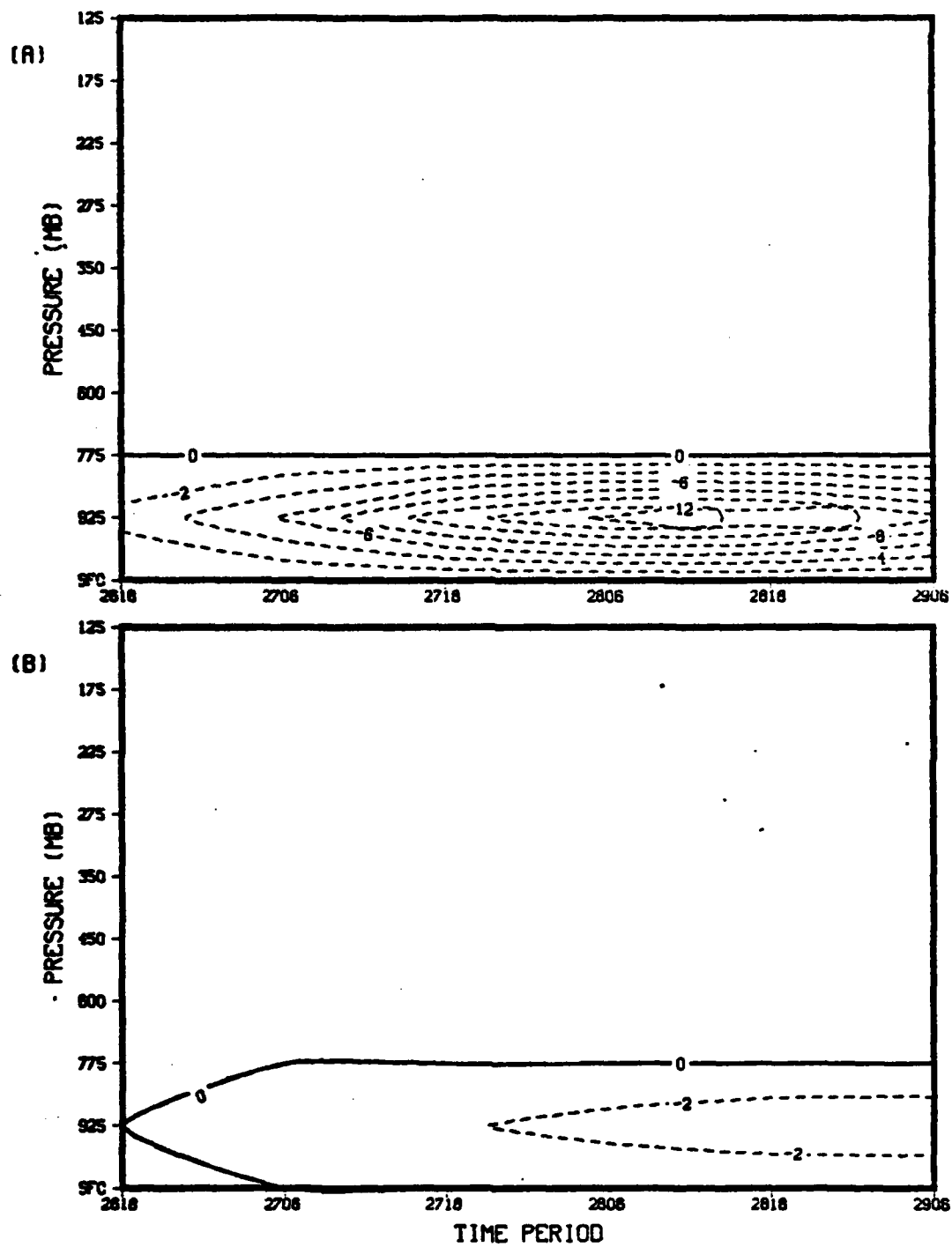


Figure 44. Similar to Figure 33 except for Frictional Dissipation

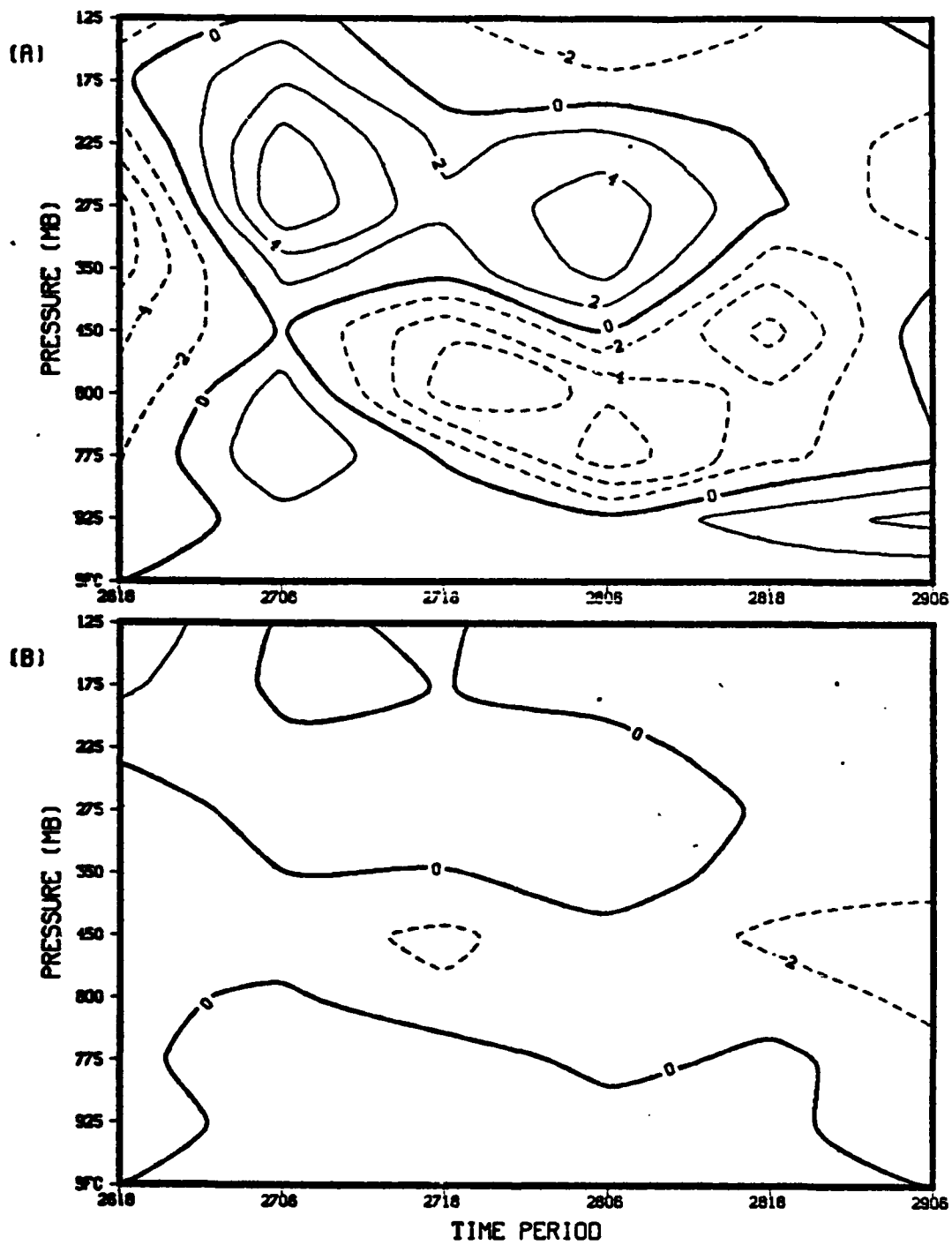


Figure 45. Similar to Figure 33 except for Residuals

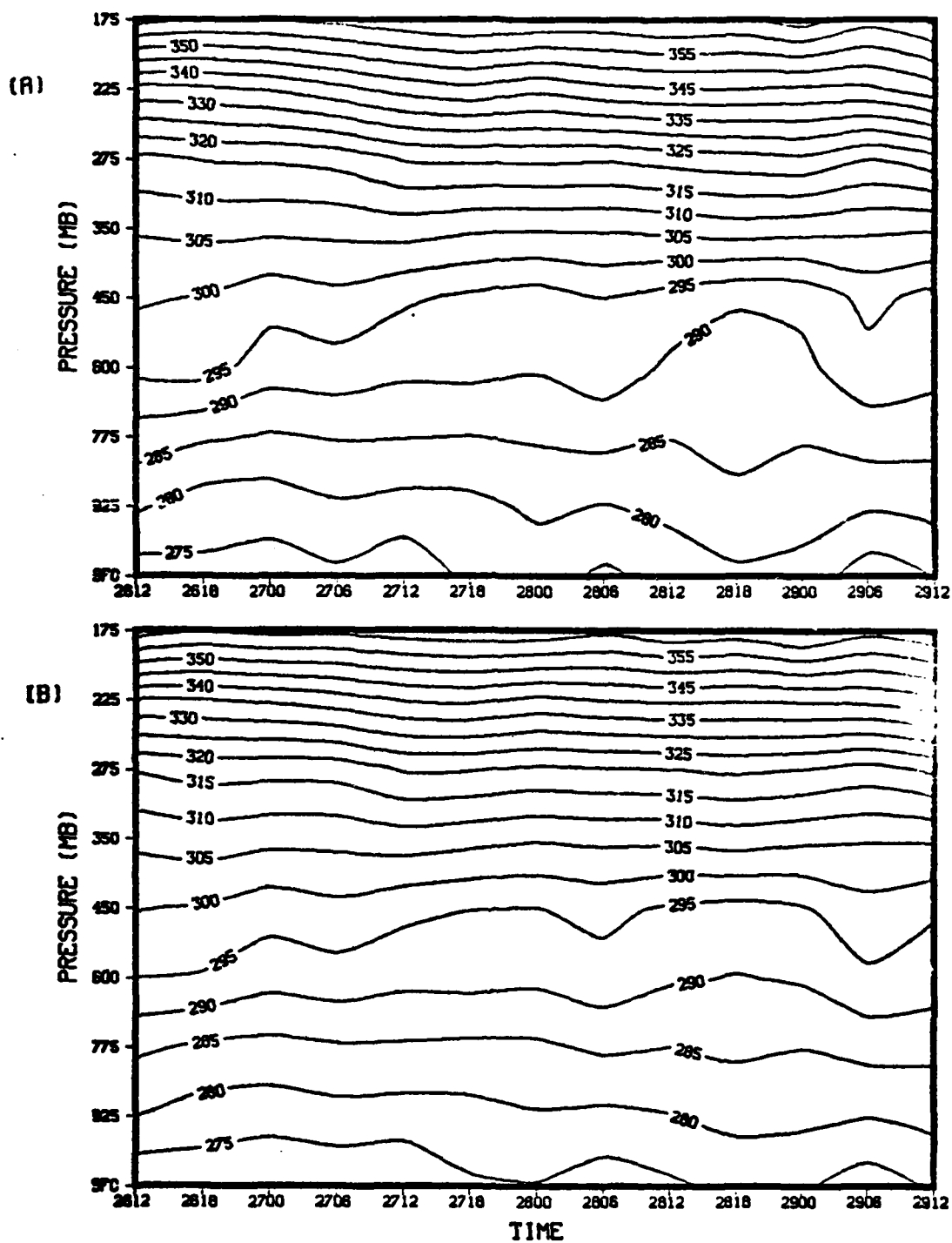


Figure 46. PGGE 6-h Area-Averaged Potential Temperatures
OK for (A) Radius 4 and (B) Radius 8.

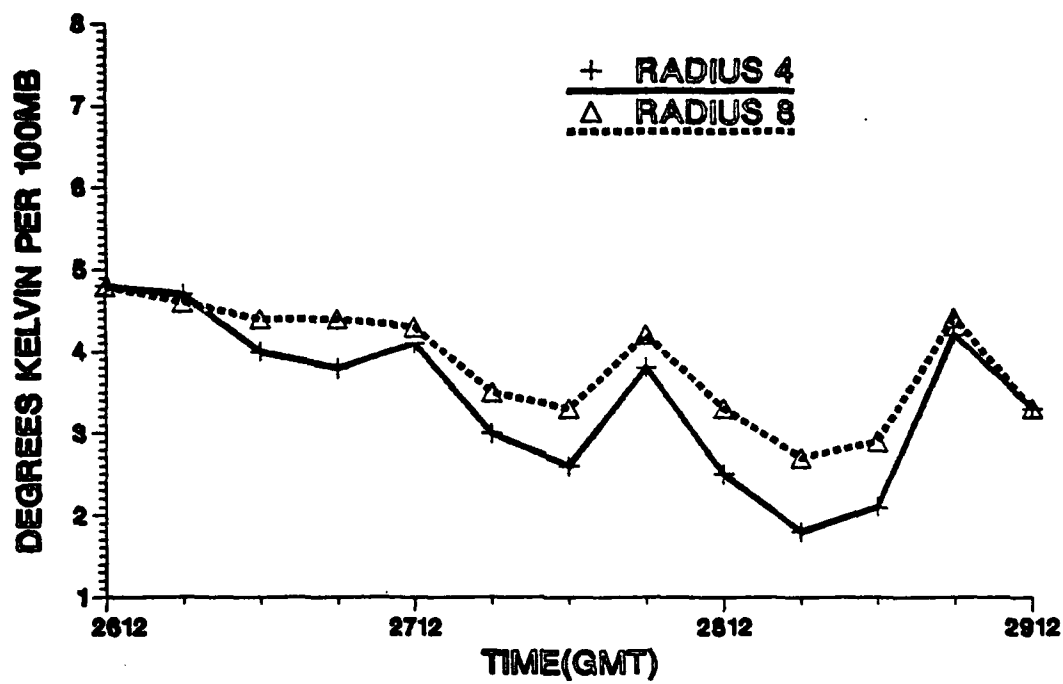


Figure 47. 6-h Static Stability Index Units same as Figure 29.

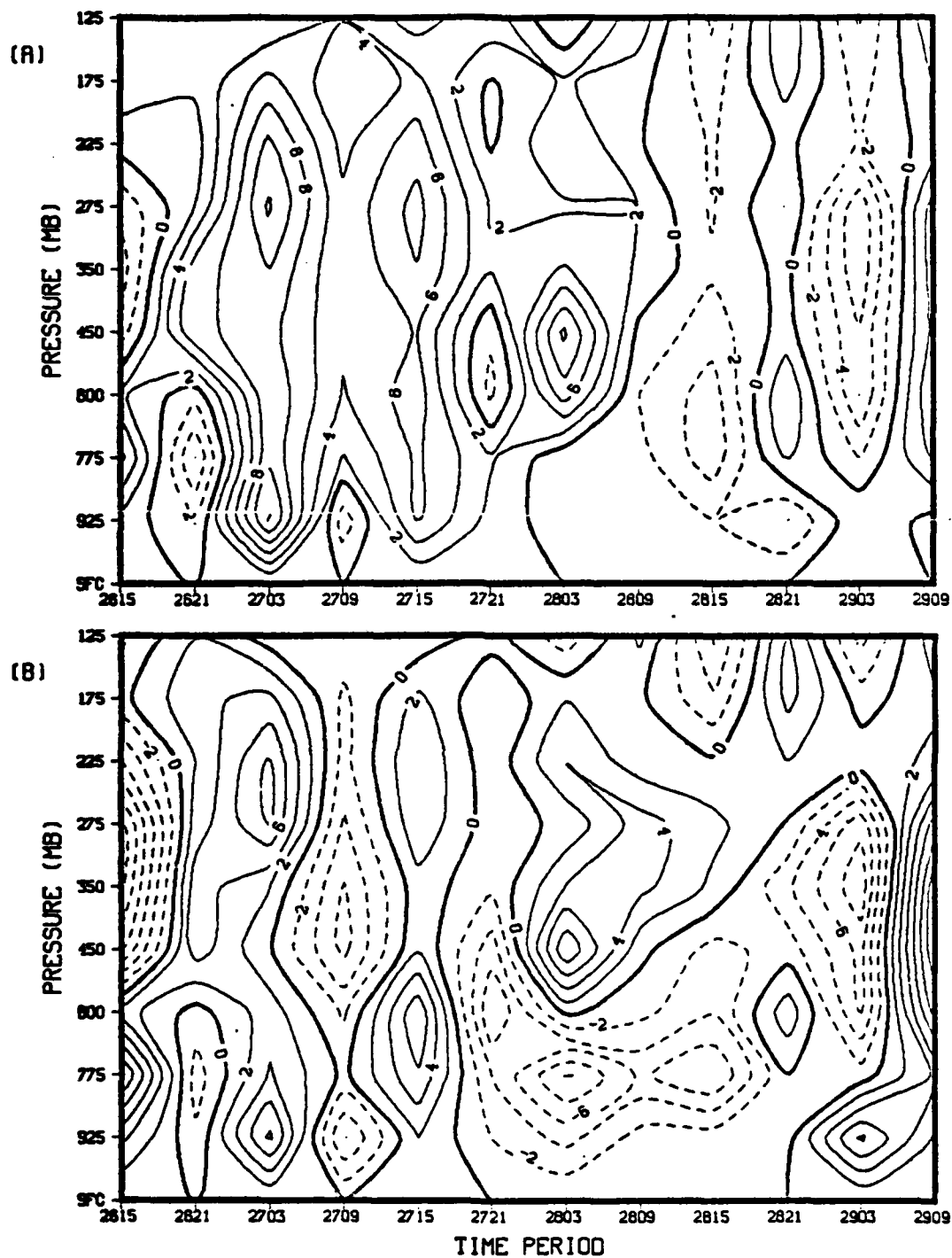


Figure 48. PGGE 6-h Radius 4 Budget Fields for (A) Time Tendencies and (B) Residuals. Units same as in Figure 33.

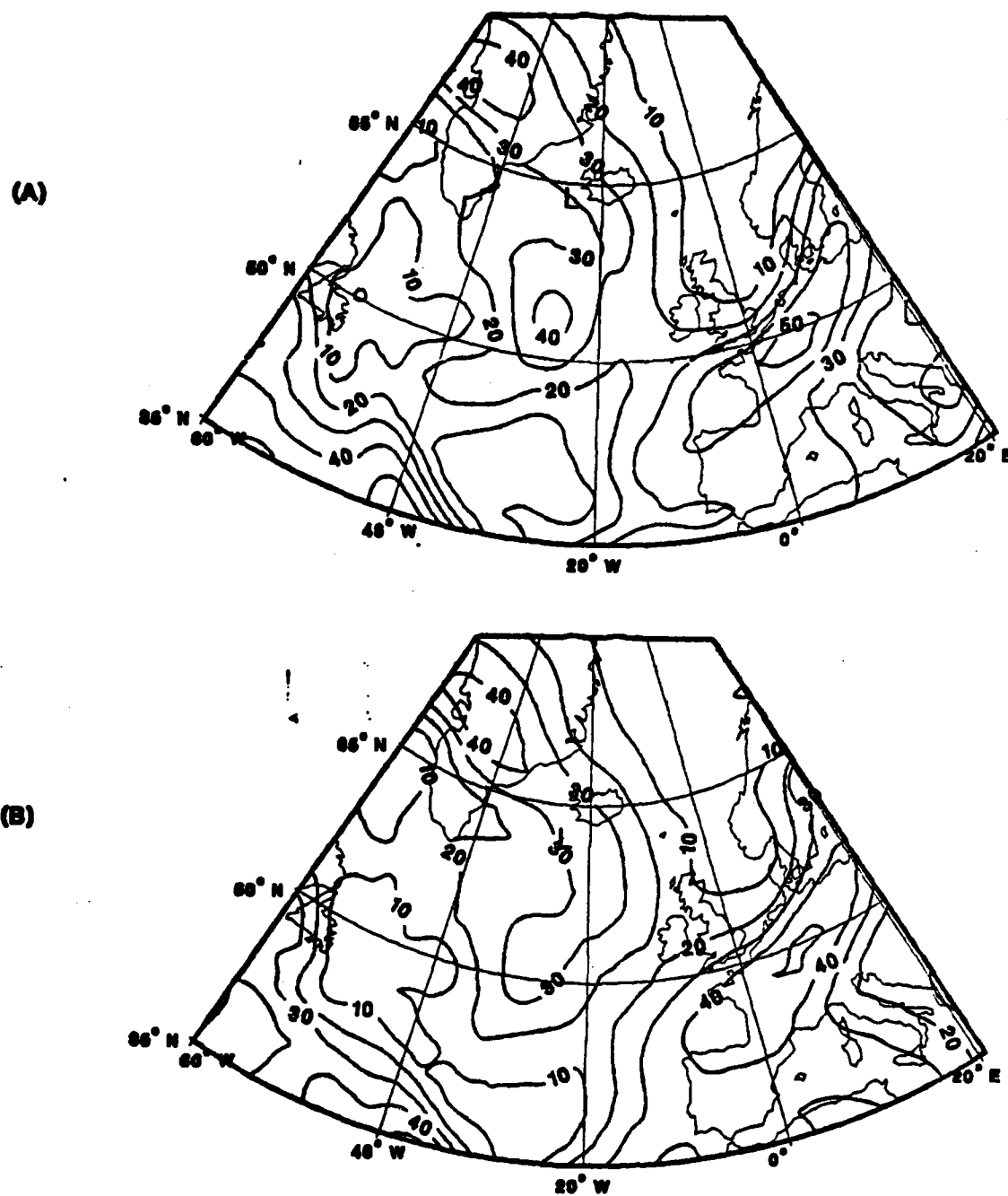
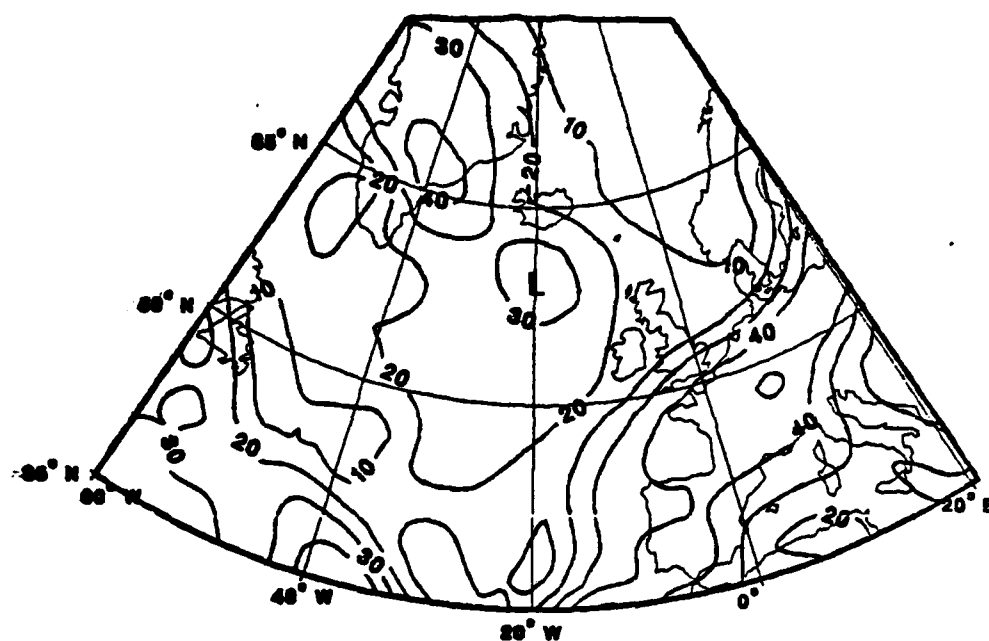


Figure 49. 300 mb Isotachs (A) 12 GMT 25 January (B) 18 GMT 26 January. Isotach Contour Intervals in 10 m/s. (L) Denotes Surface Position of Polar Lcw.

(A)



(B)

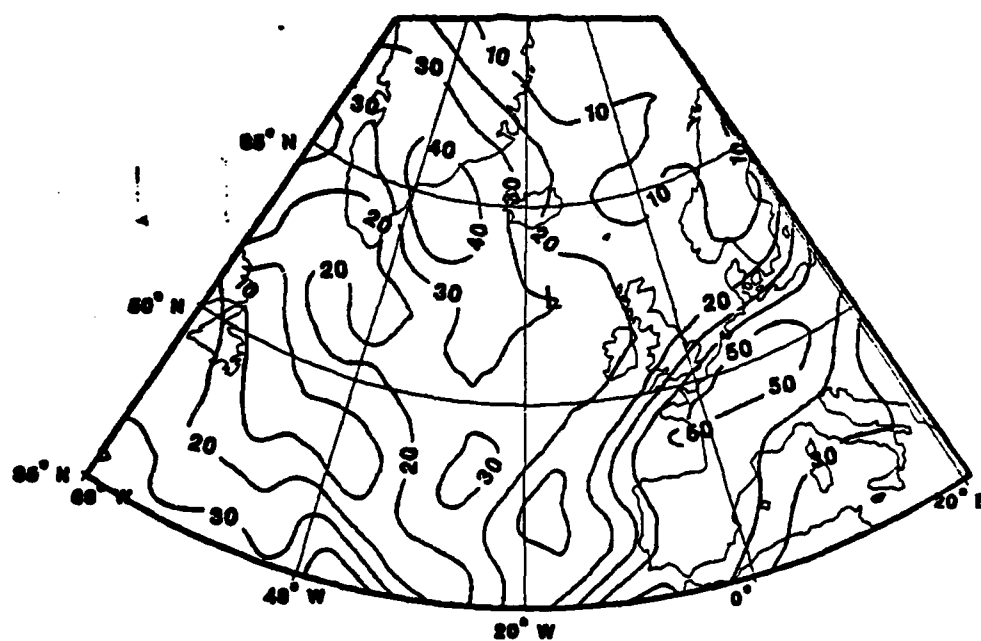
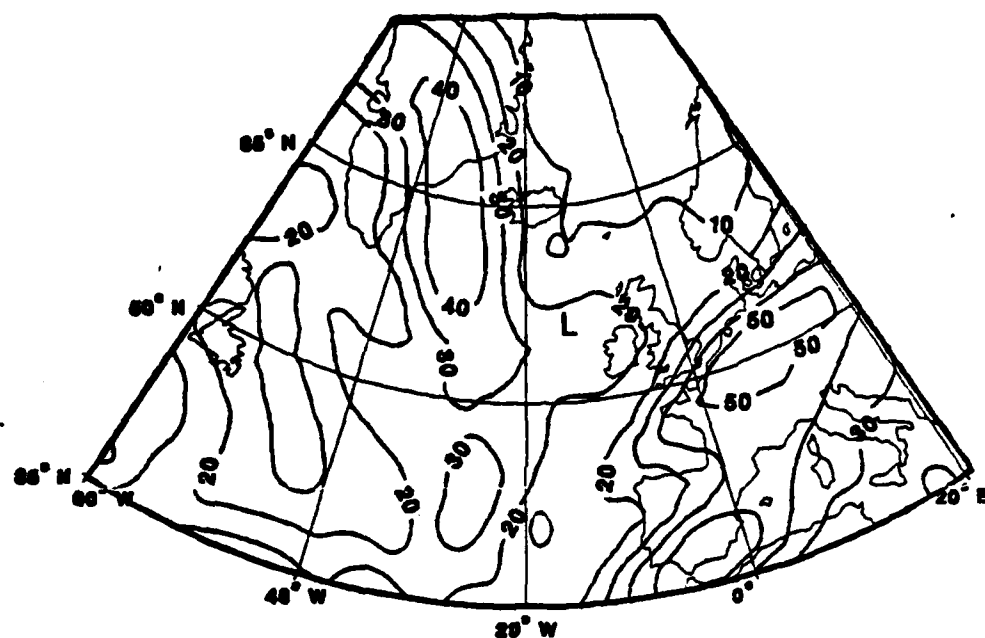


Figure 50. Similar to Figure 49 except for (A) 00 GMT 27 January (B) 06 GMT 27 January.

(A)



(B)

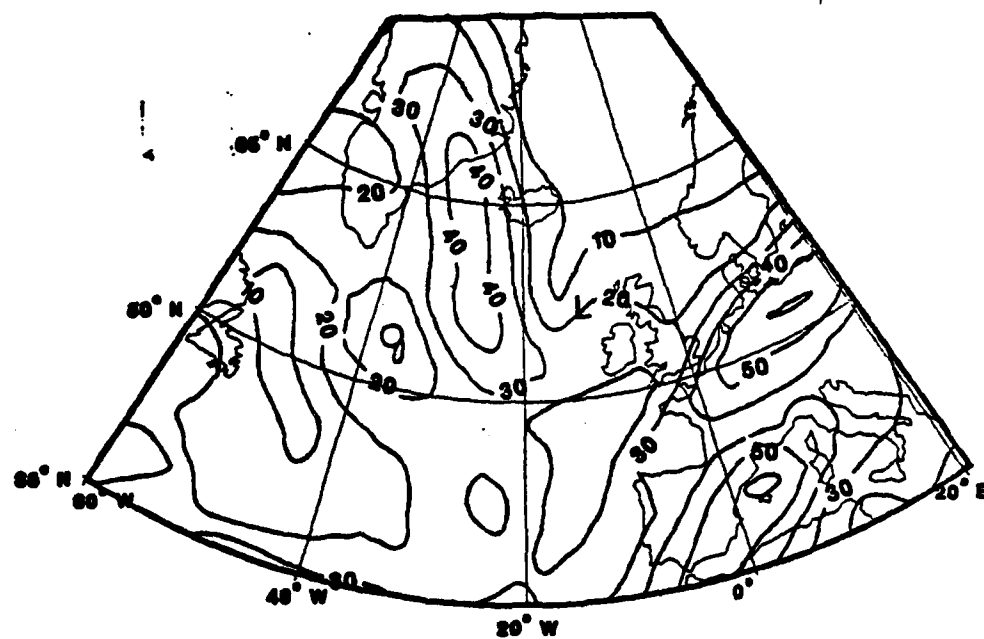


Figure 51. Similar to Figure 49 except for (A) 12 GMT 27 January (B) 18 GMT 27 January.

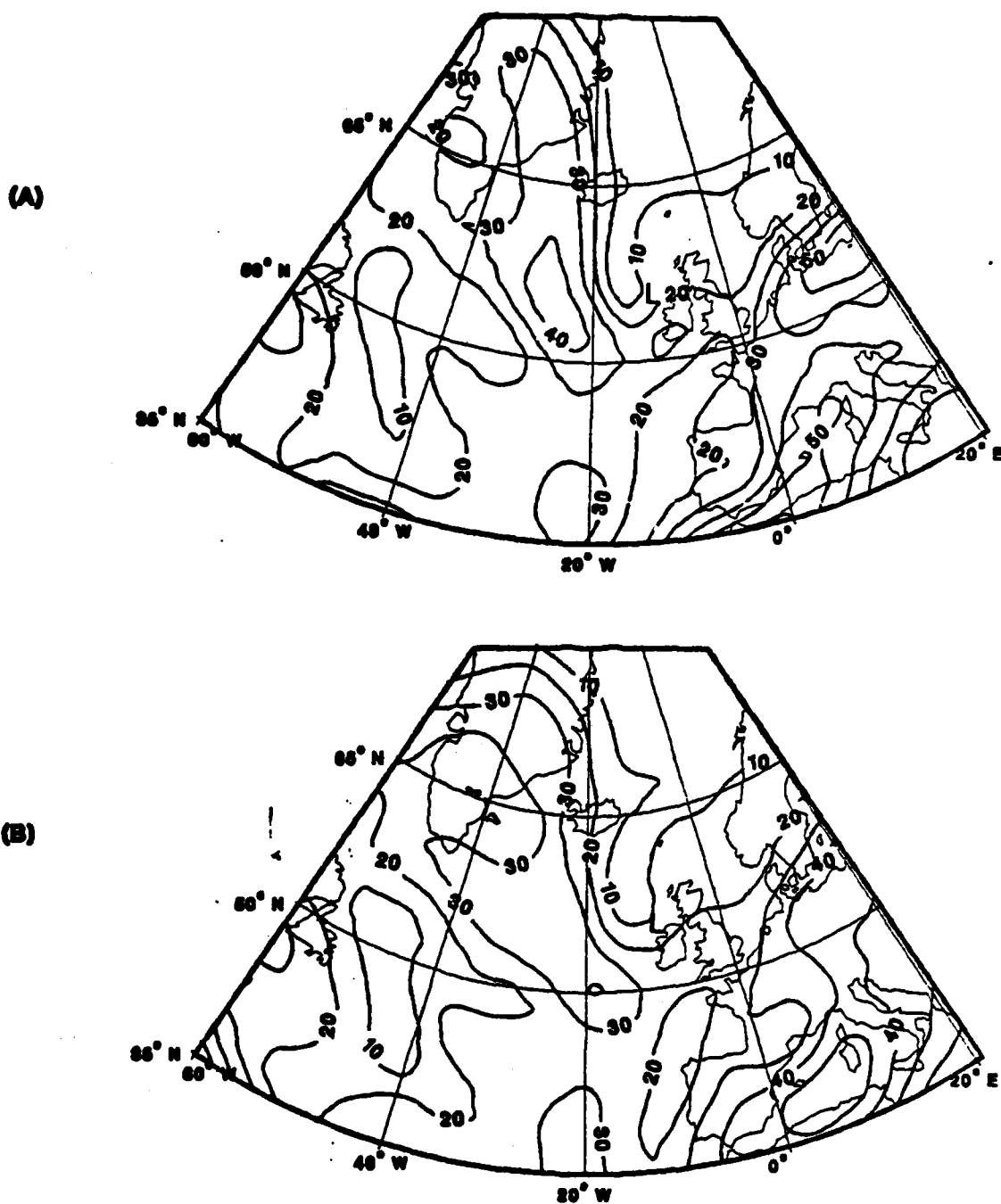


Figure 52. Similar to Figure 49 except for (A) 00 GMT 28 January (B) 06 GMT 28 January.

LIST OF REFERENCES

- Bengtsson, L., M. Kanamitsu, P. Kallberg, and S. Uppala, 1982: FGGE 4-Dimensional data assimilation at ECMWF. Bull. Am. Met. Soc., 63, 29-43.
- Calland, W. E., 1983: Quasi-Lagrangian diagnostics applied to an extratropical explosive cyclogenesis in the north Pacific. M.S. thesis, Naval Postgraduate School, 152pp.
- Conant, P.R., 1982: A study of east-coast cyclogenesis employing quasi-Lagrangian diagnostics. M.S. thesis, Naval Postgraduate School, 102pp.
- Duncan, C. N., 1977: A numerical investigation of polar lows. Quart. J. Roy. Meteor. Soc., 103, 255-268.
- Gall, R. L., 1976: A comparison of linear baroclinic instability theory with the eddy statistics of a general circulation model. J. Atmos. Sci., 33, 349-373.
- Halem, M., E. Kalnay, W. E. Baker, and R. Atlas, 1982: An assessment of the FGGE satellite observing system during SOP-1. Bull. Am. Met. Soc., 63, 407-427.
- Harley, D.G., 1960: Frontal contour analysis of a "polar" low. Meteor. Mag., 89, 146-147.
- Harrold, T. W., and K. A. Browning, 1969: The polar low as a baroclinic disturbance. Quart. J. Roy. Meteor. Soc., 95, 710-723.
- Holton, J.R., 1979: An Introduction To Dynamic Meteorology, 23, 92-100.
- James, R., 1979: Anatomy of a storm. Mar. Wea. Log., 23, 71-75.
- Johnson, D. R. and W. K. Downey, 1975a: Azimuthally averaged transport and budget equations for storms: Quasi-lagrangian diagnostics 1. Mon. Wea. Rev., 103, 967-979.
- Johnson, D. R. and W. K. Downey, 1975b: The absolute angular momentum of storms: Quasi-lagrangian diagnostics 2. Mon. Wea. Rev., 103, 1063-1076.
- Johnson, D. R. and W. K. Downey, 1976: The absolute angular momentum budget of an extratropical cyclone: Quasi-lagrangian diagnostics 3. Mon. Wea. Rev., 104, 3-14.
- Kung, E. C. and W. E. Baker, 1975: Energy transformations in middle latitude disturbances. Quart. J. Roy. Meteor. Soc., 101, 793-815.

LeMoyne, J., 1982: The Ocean Ranger's night of death. Newsweek, Mar 1, 99, 48.

Locatelli, J.D., P.V. Hobbs and J.A. Werth, 1982: Mesoscale structure of vortices in polar air streams. Mon. Wea. Rev., 110, 1417-1433.

Mansfield, D. A., 1974: Polar lows: the development of baroclinic disturbances in cold air outbreaks. Quart. J. Roy. Meteor. Soc., 100, 541-554.

Mullen, S. L., 1979: An investigation of small synoptic-scale cyclones in polar air streams. Mon. Wea. Rev., 107, 1635-1647.

Mullen, S. L., 1982: Cyclone development in polar air streams over the wintertime continent. Mon. Wea. Rev., 110, 1664-1676.

Nitta, T., and M. Yanai, 1969: A note on the barotropic instability of the tropical easterly current. J. Meteor. Soc. Japan, 47, 127-130.

Paegle, J., 1983: Some characteristics of ECMWF level III-b data sets. Global Weather Experiment Newsletter, 1, May issue.

Patterssen, S., D. L. Bradbury, and K. Pederson, 1962: The Norwegian cyclone models in relation to heat and cold sources. Geophys. Pub., 24, 243-280.

Pyke, C., 1965: On the role of air-sea interaction in the development of cyclones. Bull. Am. Meteor. Soc., 46, 4-15.

Rasmussen, E., 1979: The polar low as an extratropical CISK disturbance. Quart. J. Roy. Meteor. Soc., 105, 531-549.

Rasmussen, E., 1981: An investigation of a polar low with a spiral cloud structure. J. Atmos. Sci., 38, 1785-1792.

Reed, R. J., 1979: Cyclogenesis in polar air streams. Mon. Wea. Rev., 107, 38-52.

Roman, D., 1981: Application of quasi-Lagrangian diagnostics and FGGE data in a study of east-coast cyclogenesis. M.S. thesis, Naval Postgraduate School, 93pp.

Sanders, F. and J.R. Gyakum, 1980: Synoptic-dynamic climatology of the "bomb". Mon. Wea. Rev., 108, 1589-1606.

Sandgathe, S. A., 1981: A numerical study of the role of air-sea fluxes in extratropical cyclogenesis, Ph.D. thesis, Department of Meteorology, Naval Postgraduate School, 134pp.

Sardie, J.M. and T.T. Warner, 1983: On the mechanism for the development of polar lows. J. Atmos. Sci., 40, 869-881.

Simmons, A. J., and B. J. Hoskins, 1976: Baroclinic instability on spheres: normal modes of the primitive and quasi-geostrophic equations. J. Atmos. Sci., 33, 1454-1477.

Simmons, A. J., and B. J. Hoskins, 1978: The life cycles of some non-linear baroclinic waves. J. Atmos. Sci., 35, 414-432.

Staley, D. O., and R. L. Gall, 1977: On the wavelength of maximum baroclinic instability. J. Atmos. Sci., 34, 414-432.

Wash, C. H., 1978: Diagnostics of observed and numerically simulated extratropical cyclones, Ph.D. Thesis, Department of Meteorology, University of Wisconsin, 215pp.

Woodroffe, A., 1981: The Fastnet storm - a forecaster's viewpoint. Meteor. Mag., 110, 271-287.

INITIAL DISTRIBUTION LIST

	No. Copies
1. Defense Technical Information Center Cameron Station Alexandria, VA 22314	2
2. Library, Code 0142 Naval Postgraduate School Monterey, CA 93940	2
3. Professor Robert J. Renard, Code 63Rd Department of Meteorology Naval Postgraduate School Monterey, CA 93940	1
4. Professor Christopher N. K. Mooers, Code 68Mr Department of Oceanography Naval Postgraduate School Monterey, CA 93940	1
5. Professor Carlyle H. Wash, Code 63Wx Department of Meteorology Naval Postgraduate School Monterey, CA 93940	5
6. Professor Russel L. Elsberry, Code 63Es Department of Meteorology Naval Postgraduate School Monterey, CA 93940	1
7. Lt. William A. Cook 1254 Agate San Diego, Calif. 91208	3
8. Capt. Alan R. Shaffer, Code 63 Department of Meteorology Naval Postgraduate School Monterey, CA 93940	1
9. Director Naval Oceanography Division Naval Observatory 34th and Massachusetts Avenue NW Washington, D.C. 20390	1
10. Commander Naval Oceanography Command Central NSTL Station Bay ST. Louis, MS 39522	1

11. Commanding Officer 1
Naval Oceanographic Office
NSTL Station
Bay St. Louis, MS 39522
12. Commanding Officer 1
Fleet Numerical Oceanography Center
Monterey, CA 93940
13. Commanding Officer 1
Naval Ocean Research and Development
Activity
NSTL Station
Bay ST. Louis, MS 39522
14. Commanding Officer 1
Naval Environmental Prediction Research
Facility
Monterey, CA 93940
15. Chairman, Oceanography Department 1
U.S. Naval Academy
Annapolis, MD 21402
16. Chief of Naval Research 1
800 N. Quincy Street
Arlington, VA 22217
17. Office of Naval Research (Code 480) 1
Naval Ocean Research and Development
Activity
NSTL Station
Bay ST. Louis, MS 39522
18. Commander 1
Oceanographic Systems Pacific
Box 1390
Pearl Harbor, HI 96860
19. Commanding Officer 1
Naval Polar Oceanography Center
Navy Department
4301 Suitland Road
Washington, DC 20390
20. Commanding Officer 1
Naval Eastern Oceanography Center
McAdie Bldg (U-117)
Naval Air Station
Norfolk, VA 23511
21. Commanding Officer 1
Naval Oceanography Command Facility
P.O. Box 85
Naval Air Station
Jacksonville, FL 32212

22. Commanding Officer
Naval Oceanography Command Facility
Reflavik, Iceland
FPO New York, N.Y. 09571

1

FILME

2-84